AD-A136 305 DEVELOPMENT OF X-RAY LASER MEDIA MEASUREMENT OF GAIN AND DEVELOPMENT OF C..(U) ROCHESTER UNIV N Y LAB FOR LASER ENERGETICS J M FORSYTH FEB 83 1/2

UNCLASSIFIED AFOSR-TR-83-1136-VOL-1 AFOSR-81-0059 F/G 20/5 NL

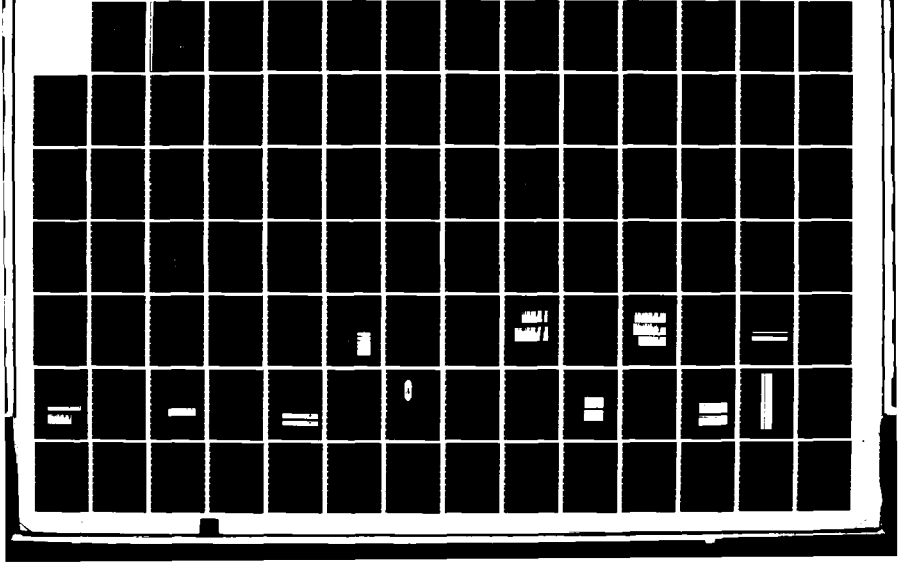

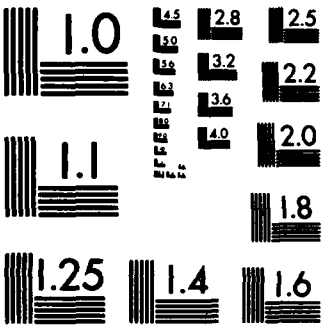

MICROCOPY RESOLUTION TEST CHART
NATIONAL BUREAU OF STANDARDS-1963-A

February 1983
Volume 1

Annual Scientific Report
1 January 1982 - 31 December 1982

Grant AFOSR-81-0059

Development of X-Ray Laser Media: Measurement of Gain and Development of Cavity Resonators for Wavelengths Near 130 Angstroms

UR
LLE

Laboratory for Laser Energetics
University of Rochester
250 East River Road
Rochester, New York 14623

Unclassified

SECURITY CLASSIFICATION OF THIS PAGE (When Data Entered)

REPORT DOCUMENTATION PAGE		READ INSTRUCTIONS BEFORE COMPLETING FORM
1. REPORT NUMBER AFOSR-TR- 83-1136	2. GOVT ACCESSION NO.	3. RECIPIENT'S CATALOG NUMBER
4. TITLE (and Subtitle) DEVELOPMENT OF X-RAY LASER MEDIA: MEASUREMENT OF GAIN AND DEVELOPMENT OF CAVITY RESONATORS FOR WAVELENGTHS NEAR 130 ANGSTROMS		5. TYPE OF REPORT & PERIOD COVERED Annual Scientific Report 1/1/82 - 12/31/82 6. PERFORMING ORG. REPORT NUMBER
7. AUTHOR(s) Dr. James Forsyth		8. CONTRACT OR GRANT NUMBER(s) AFOSR 81-0059
9. PERFORMING ORGANIZATION NAME AND ADDRESS Laboratory for Laser Energetics, College of Engineering & Applied Science, University of Rochester, 250 E. River Rd., Rochester, NY 14623		10. PROGRAM ELEMENT, PROJECT, TASK AREA & WORK UNIT NUMBERS 2301/A8
11. CONTROLLING OFFICE NAME AND ADDRESS Air Force Office of Scientific Research /NP Bolling Air Force Base Washington, D. C. 20332		12. REPORT DATE February 1983 13. NUMBER OF PAGES
14. MONITORING AGENCY NAME & ADDRESS(if different from Controlling Office)		15. SECURITY CLASS. (of this report) Unclassified 15a. DECLASSIFICATION/DOWNGRADING SCHEDULE

16. DISTRIBUTION STATEMENT (of this Report)

Approved for public release;
distribution unlimited.

17. DISTRIBUTION STATEMENT (of the abstract entered in Block 20, if different from Report)

18. SUPPLEMENTARY NOTES

19. KEY WORDS (Continue on reverse side if necessary and identify by block number)

X-Ray, Reflectors, Laser, Plasma

20. ABSTRACT (Continue on reverse side if necessary and identify by block number)

A two part study of soft x-ray laser media is presented. Experimental observation of significant population inversion on the Balmer alpha transition in hydrogen-like flourine at 81 Å in a line-focus laser plasma is reported. An analysis of the expected performance of soft x-ray multilayer reflects is presented. This volume discusses the development of an XUV (extreme ultraviolet) optics

DD FORM 1 JAN 73 1473 EDITION OF 1 NOV 68 IS OBSOLETE
S/N 0102-LF-014-6601

Unclassified
SECURITY CLASSIFICATION OF THIS PAGE (When Data Entered)

TABLE OF CONTENTS

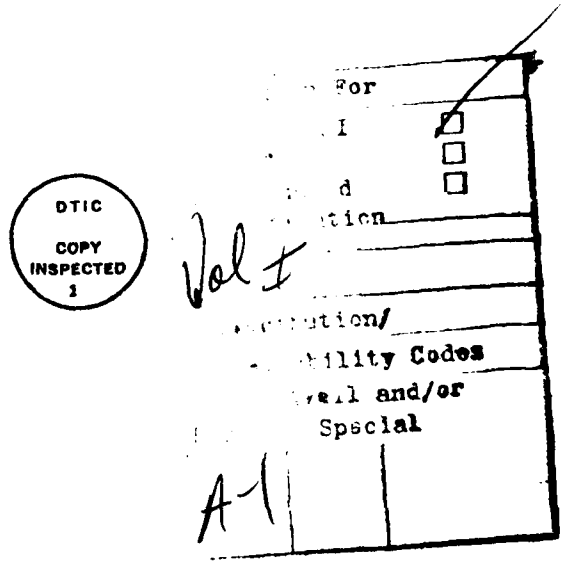

1.0 SUMMARY OF RESEARCH OBJECTIVES

During the period from January 1 through December 31, 1983 we continued our research in the following two areas:

1. Continued experimental studies of soft x-ray population inversions in recombining, laser produced plasmas with an emphasis on the development of a practical soft x-ray amplifier.
2. Analysis of the performance which could realistically be expected to be obtained from multilayer structures suitable for use as normal incidence, soft x-ray cavity mirrors.

Our activies during this period have led to several significant achievements:

1. Operation of our frequency tripled laser system in line-focus, step target geometry.
2. Observation of significant population inversion in line focus experiments on the Balmer α transition in hydrogenic flourine.
3. Successful numerical modelling of both point- and line-focus experiments.
4. Completion of the analysis of possible soft x-ray multilayer mirror performance.

Two theses were successfully completed during this period and a summary presentation of the line-focus experimental results was given at the conference on Laser Techniques for Extreme Ultraviolet Spectroscopy. Since a complete description of the work is contained in the theses, they are attached and constitute the main body of this report.

2.0 Development of an XUV Amplifier

Development of an XUV Amplifier

by

Yves G. Conturie

Submitted in Partial Fulfillment

of the

Requirements for the Degree

Doctor of Philosophy

Supervised by Dr. James M. Forsyth

Institute of Optics

College of Engineering and Applied Science

University of Rochester

Rochester, New York

1982

ABSTRACT

The feasability of an XUV amplifier based on the recombination of a laser-produced plasma was investigated. Experiments were carried out with a Nd^{+3}-glass laser generating sub-nanosecond pulses of either IR light (1.054 μm, up to 100 J) or frequency-tripled UV light (0.351 μm, up to 60 J). The plasma formed at the surface of a flat target was cooled at an early stage of its expansion by inserting a metallic foil near the target. The cooling of a dense plasma is known to result in a recombination cascade dominated by collisions, which tend to populate high-lying quantum states of the recombining ion.

With point-focus illumination (diam. $\lesssim$100 μm), population inversions were observed in the helium-like ions Al^{+11} and Mg^{+10}, showing possibility of gain on the transition 3^3D-4^3F at 129.7 Å and 154.4 Å respectively. We established that the inversions were caused neither by resonance mechanisms such as photopumping or charge transfer, nor by channelling of the plasma flow. We defined, after a parametric study, the optimum target design (slit-foil of an arbitrary material, 200 μm wide and 200 μm from the original plasma formation), and illumination conditions (UV laser of intensity $\simeq 5\times10^{14}$ W/cm^2). The short wavelength laser was shown to couple its energy to the target more efficiently.

With line-focus illumination (100 μmx2 mm, using specially manufactured cylindrical optics), inversion was observed in the hydrogenic ion F^{+8} between levels n=2 and n=3. The corresponding transition, Balmer α at 80.9 Å, was spatially resolved over $\sim$1 mm in the

direction of expansion, with single-shot recording.

Numerical simulations, using existing laser-fusion code and rate equations, were in good agreement with the data when we included enhanced recombination (via cooling) and plasma opacity. The gain region travelled with the velocity of the expanding plasma (0.3-1 10^8 cm/sec). The gain could be high locally in time and space, 10^2 cm^{-1} over $\lesssim$ 100 psec in Al^{+11} (129.7 Å) and 5 cm^{-1} over $\sim$200 psec in F^{+8} (80.9 Å). However, the plasma length (200 μm and 2.5 mm respectively, in the region of highest gain) did not permit direct gain measurement from time-integrated recordings of the amplified spontaneous emission. We discuss how that goal could be reached in the future with upgraded UV pump laser (factor 5) and time-resolved diagnostic capability ($\lesssim$100 psec).

TABLE OF CONTENTS

LIST OF TABLES

LIST OF FIGURES

CHAPTER 5

Chapter 1

Introduction

The interest in building an X-ray laser comes from the potential applications of a coherent source of X-rays in fields like chemistry, biology and crystallography (LLL 1974-75). Sources of high brightness, emitting subnanosecond pulses of energetic photons would make possible studies combining the spatial resolution of X-rays with a temporal resolution similar to what is now available in the visible and near UV. Some applications, like diffraction experiments in biology, require only a point source. But spatial coherence would provide directionality to the emission, an important factor in a spectral region where imaging is limited to small solid angle, grazing incidence optics.

Both components of such a laser, the amplifying medium and the resonator, present us with technological problems yet to be solved. Among the ideas for producing the amplifying medium, a promising one is the rapid generation of a highly ionized plasma by focusing on a solid target the intense pulse from a subsidiary laser. Such an approach, which benefits directly from the advances in laser development for inertial confinement fusion (ICF) research, has been pursued at the Laboratory for Laser Energetics (LLE) for several years (Forsyth et al 1976, Bhagavatula & Yaakobi 1978). The present thesis describes the progress made in that direction, including experimental results and numerical simulations. A separate study of the resonator is also under way at LLE (Rosenbluth 1982). Available pump laser energies limit current research to the XUV region ($\sim$100 Å), not much farther than the

region already accesible by frequency multiplication (Reintjes, et al, 1981) or mixing (Egger, et al, 1982) of existing lasers. A direct approach is attractive, however, because it is often scalable to shorter wavelengths.

1-1. Inversion methods.

There are two basic difficulties in producing an amplifying medium operating in the X-ray region (LLL 1974-75). The first is the photoelectric effect which results in the absorption of X-rays except in hot, highly ionized plasmas. The second is the very short lifetime, τ, of allowed X-ray transitions, which places severe requirements on the pumping mechanism sustaining the population inversion:

$$\tau(\text{sec}) = (8\pi^2 r_o c)^{-1} (g_u/g_l) \lambda^2 / f_{lu} \simeq 1.5 \times 10^{-16} (g_u/g_l) [\lambda(\text{Å})]^2 / f_{lu} \qquad (1\text{-}1)$$

where r_o is the radius of the electron ($2.82\ 10^{-5}$ Å), c is the velocity of light ($3\ 10^{18}$ Å/sec), λ is the wavelength of the transition, g_u and g_l are the statistical weights of the upper and lower levels respectively, and f_{lu} is the absorption oscillator strength (Griem 1964, p.45). f_{lu} is nearly constant along isoelectronic sequences, and approaches unity for intense lines (Wiese, et al, 1966-69).

Some authors (Lacour et al 1976, Duguay 1976) have proposed pumping schemes fast enough to be effective in a time shorter than τ for the production of ultra-short bursts of coherent X-rays. In such devices, an unambiguous diagnostic would be difficult due to the low photon yield. Recent progress in conventional laser technology has made possible a steady-state type of pumping, while providing conditions such

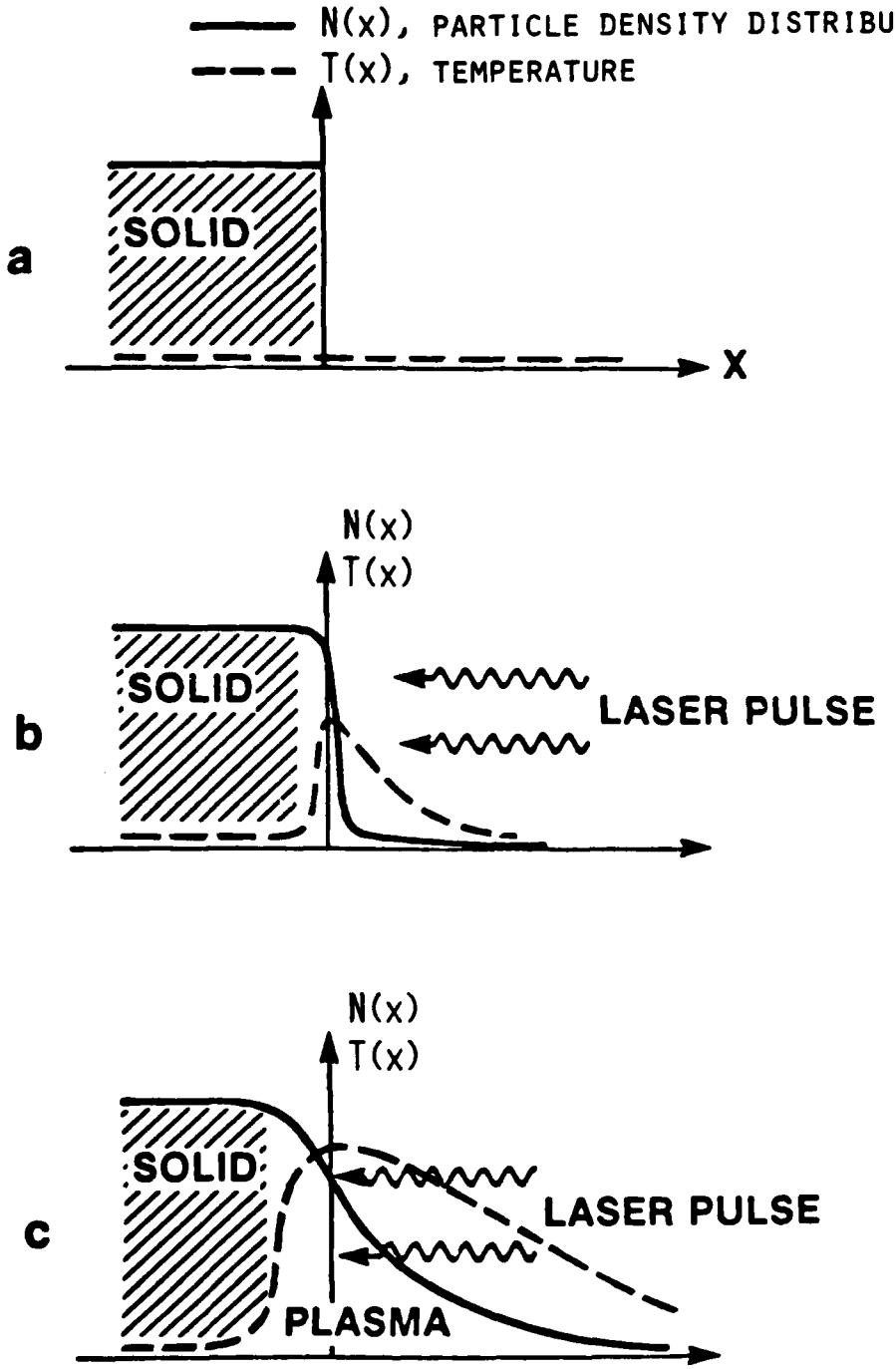

FIGURE 1-1 : LASER-PRODUCED PLASMA.

1. Recombination to Hydrogenic Plasma (i.e. one bound electron).

A. Collisional Processes:

three-body recombination and its inverse	$(N^{z+}+e^-) + e^- \rightleftharpoons N_{(p)}^{(z-1)+} + e^-(\text{accelerated})$
collisional excitation and de-excitation	$N_{(p)}^{(z-1)+} + e^- \underset{\text{inelastic}}{\overset{\text{superelastic}}{\rightleftharpoons}} N_{(q)}^{(z-1)+} + e^- \quad (q<p)$
ion-ion collisions	

B. Radiative Processes:

radiative recombination and photoionization	$N^{z+} + e^- \rightleftharpoons N_{(p)}^{(z-1)+} + h\nu$
spontaneous emission	$N_{(p)}^{(z-1)+} \longrightarrow N_{(q)}^{(z-1)+} + h\nu$
absorption (optically thick plasma)	$N_{(q)}^{(z-1)+} + h\nu \longrightarrow N_{(p)}^{(z-1)+} \quad (p>q)$

2. Recombination to lower stages of ionization.

It involves processes analogous to those listed above, and also

dielectronic recombination and its inverse (Auger)	$N_{(p)}^{(z-1)+} + e^- \rightleftharpoons N_{(p_1,p_2)}^{(z-2)+} \quad (p_1,p_2>p)$
charge exchange (here one example among many)	$2\,N_{(p)}^{(z-1)+} \rightleftharpoons N_{(p_1,p_2)}^{(z-2)+} + N^{z+}$

3. Free electrons.

bremsstrahlung and its inverse	$e^- \rightleftharpoons e^-(\text{slowed}) + h\nu$

TABLE 1-1 : PLASMA RECOMBINATION MECHANISMS.

as to prevent severe absorption effects. When a high-power laser is focused on a target, it creates a plasma at the surface (Figure 1-1). The plasma remains in a state of non-equilibrium for a time of the order of the laser pulse duration, τ_L, which can be much longer than τ. During that time, τ_L, recombinations in the plasma take place through mechanisms, both collisional and radiative, which populate the various levels of the lower stages of ionization at different rates (Table 1-1). In collisional processes an ion can interact with another ion (with possibilities of charge exchange), one electron (inelastic collision, dielectronic recombination) or two electrons (three-body recombination). Radiative processes can involve one ion (spontaneous emission, stimulated emission and absorption), one ion and one electron (radiative recombination) or one electron (bremsstrahlung). Some of the ideas suggested to make this plasma behave as an X-ray amplifier have led to experimental works: charge exchange (Scully, et al, 1973), resonant photoexcitation (Norton & Peacock 1975), dielectronic recombination (Jaegle, et al, 1981), and recombination with cooling (Gudzenko & Shelepin 1965), the latter being the basis of our own research.

(i) Charge exchange. The idea is to utilize electron pick-up in an excited state of the ionized species. Dixon et al (1977-78) have taken advantage of the large cross-section for the transfer of an electron from atomic Carbon to $C^{+5,+6}$ resulting in the selective production of excited ions $(C^{+4,+5})^*$. They focus a Nd^{+3}-glass laser (5 J, 16 nsec) on a carbon slab. A background gas (Helium, 1 torr) is used to allow the formation of neutral atoms and to slow down the reacting ions, a low relative velocity being required. Population inversion occurs between

the levels n=5,4,3 in both C^{+4} and C^{+5} about 2 cm from the slab but the low ion density ($\sim 10^{14}$ cm^{-3}) results in such a weak emission, and weak gain, that many shots are necessary for measurement and no diagnostic is possible on the potential amplification (350-760 Å region). In order to achieve higher densities, Seely & McKnight (1977) have proposed to use Argon instead of Helium, the charge transfer taking place directly between the ions C^{+6} and Ar^{+2} within 1 mm of the target. Amplification is expected at 182 Å on C^{+5}(3-2). No experimental follow-up on this scheme has, so far, been reported.

(ii) Resonant photoexcitation. In a dual plasma the radiation emitted by one species ("source ion") pumps the other species ("lasing ion") to an excited level $n \geq 2$ (n, principal quantum number), resulting in an inversion between the levels n and n-1. The process is effective if there is resonant absorption of the pump radiation, as can be done by an appropriate choice of species. Hagelstein (1981) has proposed to pump Ne^{+1} "by preferential photoionization of 2s electrons from [atomic neon], resulting in a 2s-2p inversion at 27 eV [460 Å] in Ne^{+1}. The target design implementing the scheme is based on thin film flashlamp and filter systems which emit strong X-ray radiation near 500 eV [25 Å] when irradiated with short pulse (90 psec) 1.06 μm radiation at 10^{14} W/cm^2. (...) Gains in excess of 50 cm^{-1} are calculated" (ibid.). Experiments, to be carried out at LLE with the OMEGA laser system (Bunkenberg, et al, 1981), are in the planning stage.

(iii) Dielectronic recombination. Ions whose configuration includes more than one excited electron often correspond to energy levels above the ionization limit, that are called "autoionizing" because they can

decay spontaneously by ejecting an electron instead of by emitting a photon. The populations of these levels are in equilibrium with the thermal continuum of free electrons even when the ionic distribution itself departs from equilibrium. Thus the reverse process of electron capture (dielectronic recombination) followed by collisional transfer to levels below the ionization limit may enhance strongly the populations of some levels of specific ions, and be a source of population inversion. This is the interpretation given by Jaegle et al (1981) for their own early observation of gain at 117.41 Å on the transition $2p^5 4d(^3P_1)-2p^6(^1S_o)$ in Al IV (1971, 1974). A gain coefficient of 10 cm^{-1} is reported in a plasma of electron density $10^{20}-10^{21}$ cm^{-3} formed by a Nd^{+3}-glass laser (20 J, 40 nsec).

(iv) Recombination with cooling. Collisional and radiative processes tend to favor high- and low-lying quantum levels respectively. In a dense plasma, collisions become important and an inversion can be achieved during the cascade through the excited levels of the recombining ions. Rapid cooling is required in order to "freeze" the plasma in a much higher ionization state than predicted by the equilibrium relations. "Cold" electrons recombine mainly into the higher levels, while the lower levels are still relatively empty (Gudzenko & Shelepin 1965). Population inversions have been observed in particular in Carbon VI during the adiabatic expansion of a cylindrical fiber (Jacoby et al 1981), and in Aluminum XII through external heat loss (Bhagavatula & Yaakobi 1978). In the former, a direct measurement of gain x length product up to 5 is reported on the 3-2 (Balmer α) transition at 182 Å. In the latter, the cooling is so effective that

line-intensity inversions are observed and a gain of 10 cm^{-1} is predicted on the manifold 4^3F-3^3D at 129.7 Å.

1-2. Thesis outline.

The plasma recombination concept is the most promising of those listed above: (i) it has already been demonstrated in the visible (Silfvast et al 1979-b, 1980), (ii) several independent experiments at various laboratories have led to population inversion in the XUV region, (iii) there is potential for significant gain because inversion can occur at high density. Our thesis being based on that concept, in Chapter 2 we outline the theoretical treatment of recombining plasmas developed by Bates (1962-a and -b), McWhirter (1963) et al. We also review several diagnostic methods relevant to this thesis.

Chapter 3 gives some details about the instrumentation necessary for an experimental study: high-power laser, focusing optics, diagnostic instruments. For the most part, we used existing hardware, with some modifications to fit our requirements.

Our study, described in Chapter 4, tried to address three issues: the choice of an XUV transition, the target design to achieve a population inversion, and the design of an amplifier for direct gain measurement. It is desirable to choose a transition from a highly stripped ion, to limit the number of recombination channels. Also, the higher the atomic number, the shorter the wavelength of the transition is, but an upper limit is set by the available pump laser. Experiments were carried out with a Nd^{+3}-glass laser generating sub-nanosecond pulses of either IR light (1.054 μm, up to 100 J) or frequency-tripled

UV light (0.351 μm, up to 60 J).

With point-focus illumination (diam. ≤100 μm), population inversions were observed in the helium-like ions Al^{+11} and Mg^{+10}, showing possibility of gain on the transition 3^3D-4^3F at 129.7 Å and 154.4 Å respectively. We established that the inversions were caused neither by resonance mechanisms such as photopumping or charge transfer, nor by channelling of the plasma flow. We defined, after a parametric study, the optimum target design (slit-foil of an arbitrary material, 200 μm wide and 200 μm from the original plasma formation), and illumination conditions (UV laser of intensity $\simeq 5 \times 10^{14}$ W/cm^2). The short wavelength laser was shown to couple its energy to the target more efficiently.

Experiments were also done with line-focus illumination (100 μmx2 mm, using specially manufactured cylindrical optics), to study the design of an actual XUV amplifier. Inversion was observed in the hydrogenic ion F^{+8} between levels n=2 and n=3. The corresponding transition, Balmer α at 80.9 Å, was spatially resolved over ∿1 mm in the direction of expansion, with single-shot recording.

We made numerical simulations of our results with a 1-dimensional laser fusion code, LILAC (Goldman 1973, Delettrez 1978-82). Chapter 5 shows how the hydrodynamic motion of the plasma (LILAC), the ionic rate equations (McWhirter & Hearn 1963), and our own radiation transport and target modeling were combined. Experimental data could be reproduced when we included enhanced recombination (via cooling) and plasma opacity. The gain region travelled with the velocity of the expanding plasma (0.3-1.0 10^8 cm/sec). The gain could be high locally in time and

space, 10^2 cm^{-1} over $\lesssim$100 psec in Al^{+11} (129.7 Å) and 5 cm^{-1} over $\sim$200 psec in F^{+8} (80.9 Å). However, the plasma length (200 μm and 2.5 mm respectively, in the region of highest gain) did not permit direct gain measurement from time-integrated recordings of the amplified spontaneous emission. That goal could be reached in the future with upgraded UV pump laser (factor 5) and time-resolved diagnostic capability ($\lesssim$100 psec).

More details about the instrumentation and data reduction procedures can be found in three appendices. They cover our photometry & film calibration (Appendix A), the experimental wavelength determination of lines recorded with crystal and grating spectrographs (B), and the design & fabrication of the cylindrical optics to form a line-shaped plasma for an XUV amplifier (C). The work described in the appendices, while an important part of our experimental study, can also be useful to spectroscopists in other applications. Several users' codes have been written to make that work easily available.

Chapter 2

Recombination of a Highly-Ionized Plasma

There are a number of proposals to form an X-ray amplifying medium in a recombining plasma (see Chap.1). For a more quantitative evaluation of their feasability, a comprehensive calculation of the population densities in the plasma is required. The standard model is that of McWhirter & Hearn (1963). Modifications and refinements have been suggested for some coefficients (Whitney et al 1974-1980, Weisheit 1975, Landshoff & Perez 1976, Salzmann & Wendin 1978), but the overall procedure is widely accepted. In this chapter we outline their model, which is the basis of the atomic rate equations routine included in our numerical simulation (Chapter 5). We also review some spectroscopic techniques to measure the temperature and density in a highly-ionized plasma.

2-1. Rate Equations.

McWhirter & Hearn have calculated the instantaneous population densities, P(n), of the excited levels (n, principal quantum number) of hydrogenic ions in a plasma. The steps in their procedure are (a) to get an expression for the rate coefficient of each collisional or radiative process, (b) to write the rate equations for the P(n), (c) to make reasonable assumptions in order to simplify the equations and solve them, for the electron temperature (T_e) and density (N_e) prevailing in the plasma. The collisional and radiative processes listed in Table 1-1 are all included except those involving the absorption of photons:

opacity is not considered, at least not at this stage. One looks for a local, "quasi-static" solution for a given set of conditions (T_e,N_e). The assumptions that are made are the following:

(i) The free electrons have a Maxwellian distribution.

(ii) Steady-state approximation. "The time in which the population densities of the excited levels come into equilibrium with a particular population density of the ground level, free electrons and bare nuclei is so short that it is sufficient to express these equilibrium population densities as functions of the ground level population density" (ibid.). Setting the time derivatives $dP(n)/dt=0$ $(n>1)$ leads to a set of simultaneous equations,

$$P(n) = C_o + C_1 P(1) \qquad (n > 1) \qquad (2\text{-}1)$$

where C_o and C_1 are time-independent parameters which are functions of n, N_e, T_e and the atomic number Z.

(iii) The number of simultaneous equations (2-1) can be kept finite because the field from the surrounding plasma produces a lowering of the ionization limit: beyond a certain value of n, the bound levels lose their discrete nature and merge into the continuum of free electrons. Also, for levels of high n, collisions dominate and the levels are in Saha-Boltzmann equilibrium (which is simply the result of Boltzmann statistics applied to the system [ion + electron], see for example Griem 1964). That approximation is made for n>20 "because this is the limit of the tables of oscillator strength. (...) For many conditions this is much higher than necessary" (McWhirter & Hearn 1963). Eq.2-1 can be written in terms of the Saha-Boltzmann population densities $P_E(n)$

defined for the local value of (T_e, N_e):

$$P(n)/P_E(n) = r_o(n) + r_1(n)[P(1)/P_E(1)] \qquad (2\text{-}2)$$

One still has to solve the rate equation for the ground-state. It can be written as follows:

$$dP(1)/dt = N_e[\alpha P(N^{+z}) - S P(1)] \qquad (2\text{-}3)$$

where $P(N^{+z})$ is the population density of bare nuclei. In that "collisional-radiative" model, the recombination coefficient α includes three-body and radiative recombination, collisional deactivation and cascading, while the ionization coefficient S includes collisional excitation, and ionization and photoionization. α and S are functions of T_e, N_e and Z.

A further generalization is possible if one defines "reduced" temperature $\theta_e = T_e/Z^2$ and density $\eta_e = N_e/Z^7$. The quantities α/Z and Z^3S are functions of θ_e and η_e only. Hence the important parameters to consider when studying a highly ionized plasma are (θ_e, η_e), not (T_e, N_e). McWhirter & Hearn have generated on a computer, in the range 0.35 eV$< \theta_e <$ 22 eV and $10^8 cm^{-3} < \eta_e < 10^{18} cm^{-3}$, the coefficients $r_o(n)$ and $r_1(n)$ (see Eq.2-2), and the ratio $P_s(1)/P_E(1)$ where $P_s(1)$ corresponds to a true steady-state (ground level in equilibrium).

In the extreme cases of high and low density η_e, the recombination is controlled by collisional and radiative processes respectively. Collisions help fill the upper excited states of the hydrogenic ion, while radiative decay rapidly populates the ground-state and lower excited states. The filling of the upper levels through collisions is

also influenced by temperature. Let us consider the three-body recombination and its reverse process (Table 1-1). In a collision between a free electron and an hydrogenic ion, ionization is more likely to occur if the bound electron is already in an upper level. This is especially true when the incident electron has a low kinetic energy, i.e. low temperature θ_e. Seen from the opposite perspective, the probability of a collision between one ion and two free electrons is higher at lower velocity. Most interactions will be at a distance, producing weak energy perturbations, and recombination will occur in one of the bound levels near the ionization limit.

For a given set of conditions (θ_e, η_e), one can define the level for which upward collisional excitation equals downward radiative loss. It is called the collision limit n_L (Griem 1964, Pert & Ramsden 1974):

$$n_L^{17} = 5\ 10^{35}\ \eta_e^{-2} (\theta_e / E_H)\ \exp(4\, E_H / n_L^3\, \theta_e) \qquad (2\text{-}4)$$

where E_H is the Rydberg energy. In the relevant interval of temperature and density, n_L is a strongly decreasing function of η_e and weakly increasing function of θ_e (Figure 2-1). High density is required to keep n_L low, say <4. Low temperature fills the level above n_L, which is in thermal equilibrium with the upper levels, while the level just below is emptied by radiation to the ground-state. That idea for producing a population inversion has triggered several experimental programs (see Sec.1-1), including our own as described later in this thesis.

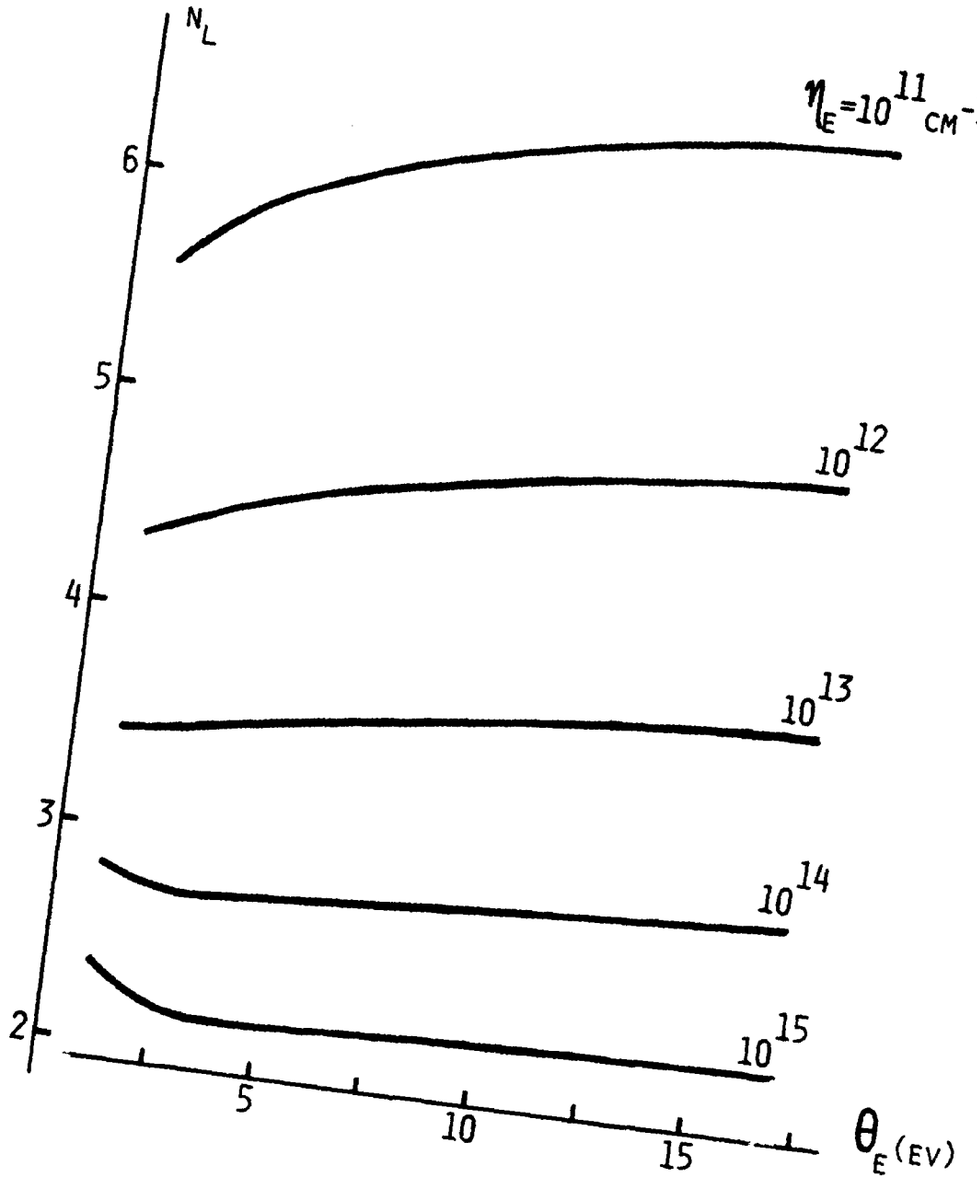

FIGURE 2-1 : COLLISION LIMIT, $N_L = F(\theta_E, \eta_E)$.

2-2. Plasma Spectroscopy.

Plasma temperature and density may be inferred from the spectroscopic recording of transitions in 1- and 2-electron ions (Griem 1964, 1974). Among the lines that are useful for such diagnostic, and/or are present in many of our experimental results (Chap.4), we will mention the following:

(i) Resonance lines. They are allowed transitions to the ground state, 1s-np and $1s^2(^1S)$-$1snp(^1P)$ ($n\geq 2$), in the hydrogenic and helium-like ions, respectively. The series 1s-np is also called Lyman series (Lyman α for n=2, $\beta,\gamma,\delta,\varepsilon$,etc... for n=3,4,5,6,etc...). When the term "resonance line" is used alone, it refers to the first line of the series, i.e. 1s-2p or $1s^2$-1s2p, often the latter when there is no ambiguity.

(ii) Intercombination lines. They are forbidden transitions to the ground state, such as the triplet-singlet lines $1s^2(^1S)$-$1snp(^3P)$ and $1s^2(^1S)$-$1sns(^3S)$ in the helium-like ion. In our case the label will always refer to n=2.

(iii) Satellite lines. They are transitions corresponding to a doubly-excited level, as can be produced by dielectronic recombination. For example, lines of the Lyman series (1s-np) have helium-like satellites 1sms-npms and 1smp-npmp ($m\geq 2$). Similarly, lines of the helium-like resonance series ($1s^2$-1snp) have lithium-like satellites $1s^2$ms-1snpms and $1s^2$mp-1snpmp. The most intense satellites, and those resulting in a spectral shift large enough to be resolved, correspond to m=2, especially 1s2p-$2p^2$ (labeled s) and $1s^2$2p-1snp2p (labeled s_n unless specified otherwise). There are also higher order satellites, where the

same basic transition takes place in an ion whose electronic shells are partially filled. The last satellite of the resonance line $1s^2$-1s2p is the so-called K_α line, when the atom is neutral except for one vacancy created in its K-shell.

2-2-a. Temperature Measurement.

One may distinguish between methods which require some knowledge of the electron density N_e and those which do not (Woodall, et al, 1976). One finds in the first category (i) the ratio of two resonance lines (1s-np)/($1s^2$-1snp), especially with n=2, (ii) the ratio of two lines belonging to the same resonance series. The second category includes (i) the ratio of a resonance line and its nearby satellites, which is proportional to T_e, (ii) the slope of the free-bound continuum beyond the series limit, which is proportional to $\exp(-h\nu/kT_e)$. A serious problem in dense plasmas is that of self-absorption. Methods involving lines with high oscillator strength, hence high opacity (such as 1s-2p and $1s^2$-1s2p), become very inaccurate. Examples will be given later (Figs.5-4 & 5-5).

2-2-b. Density Measurement.

Available methods include (i) the ratio of the helium-like resonance to intercombination lines, (ii) Stark broadening. The first method relies on the fact that, in a certain range of densities, the lifetimes of the resonance (^1P) and metastable (^3P) states are respectively shorter and longer than the time constant for collisions between the two states. That time constant , hence the line ratio, is

density dependent (Griem 1975). In the second method, the spectral broadening induced by fields from surrounding ions makes the discrete spectrum merge with the free-bound continuum. The number of the last discernible spectral line in the resonance series depends on the broadening, which is density dependent (Inglis & Teller 1939).

Chapter 3

Instrumentation

Experiments were carried out with several laser configurations, in terms of wavelength, beam diameter, output energy and power. Optics to form a point focus or a line focus were used, sometimes with the addition of a blast-shield. Diagnostic instruments included a variety of crystal spectrographs, grating spectrographs and pin-hole cameras. This chapter describes that instrumentation and the context in which it was used.

3-1. Laser.

Figure 3-1-a shows the Glass Development Laser , GDL (Seka et al 1980), a one-beam prototype of the 24-beam OMEGA laser built for Inertial Confinement Fusion (ICF) research: "[its] basic design characteristics include Nd-doped phosphate glass, rod amplifiers up to 90 mm diameter, the propagation of a circularly polarized beam [to reduce the effective non-linear index of refraction of the glass], extensive spatial filtering and imaging, and the use of large aperture Pockels cells" (ibid.). Depending on the type of oscillator used, the output at λ=1.054 μm can be a "short", high-power pulse (50 psec FWHM, up to 500 GW) or a "long", energetic pulse (500 psec, up to 100 Joules; 1 nsec, up to 120 Joules). These numbers correspond not to peak performance but to what the system can deliver on a regular basis. Also available to us for some experiments was an up-graded version of GDL where a series of prototype high-power amplifier modules called "active

GDL (IR) (3-1-A)

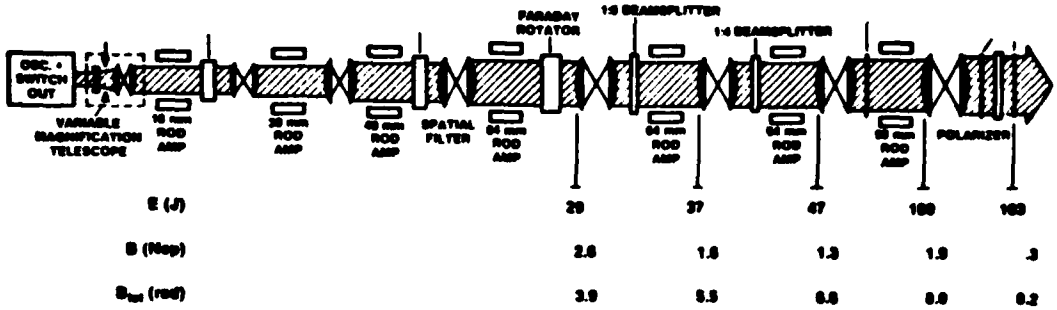

GDL (UV) (3-1-B)

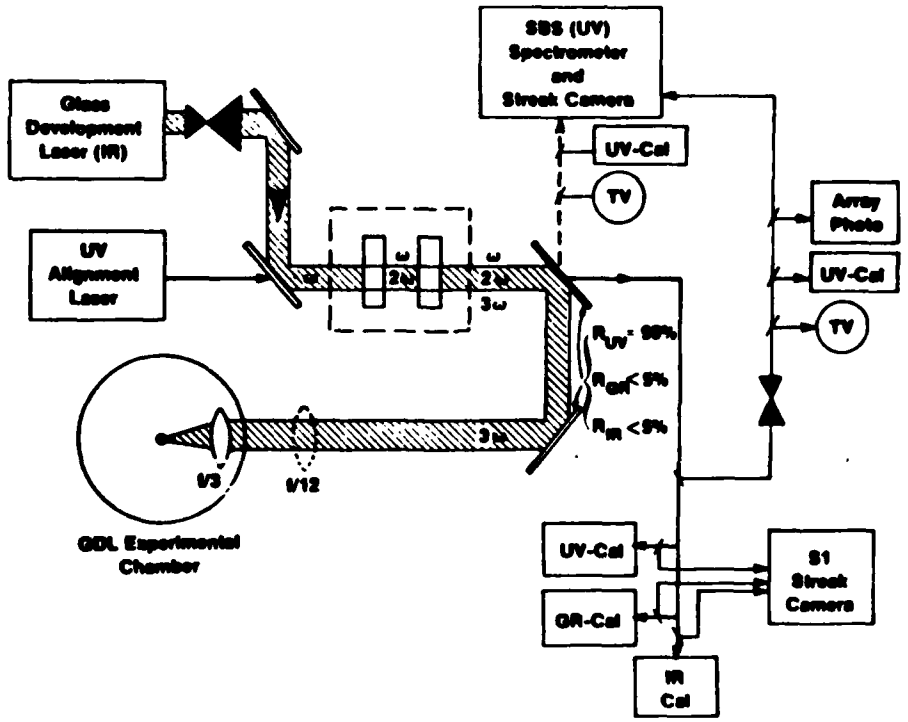

FIGURE 3-1 : GLASS DEVELOPMENT LASER IN ITS IR (1.054 μM) AND UV (0.351 μM) CONFIGURATIONS.

mirrors" (Brown et al 1981) were added at the end of the beamline. They boosted the output of the laser above 200 Joules (700 psec FWHM), with a beam diameter of 150 mm.

In the past two years GDL has been converted to short wavelength (0.351 μm) by frequency doubling and tripling the 1.054 μm beam in a pair of type II KDP crystals (Seka et al 1981). The 90 mm GDL output beam is expanded to 130 mm to nearly fill the crystals. The overall conversion efficiency to third harmonic is close to 60% in long pulse operation (500 psec). The layout is shown in Figure 3-1-b. A number of diagnostics, mainly calorimeters and streak cameras, provide a complete characterization of the laser pulse.

3-2. Optics.

The GDL output beam, at 1.054 μm or at 0.351 μm, is linearly polarized. A series of coated mirrors, optimized for maximum reflection, transport the beam toward the focusing optics and the experimental vacuum chamber. When the direct IR output is used, a quarter-wave plate (mica) is added at the end of the beamline so that light reflected by the target cannot propagate back and damage the rod amplifiers. That risk does not exist in the UV configuration because the frequency conversion is not reversible.

The optics used to focus the beam on target and the flat window serving as interface with the vacuum are made of BK-7 glass (1.054 μm light) or fused silica (0.351 μm light), with anti-reflection coatings on each face. In all point-focus studies a single-element aspheric lens was used. In early IR experiments the lens had a focal length of 30 cm, a working f-number 3.5 and was located inside the vacuum tank. In order

to go through its clear aperture, the 90 mm output beam from GDL was slightly demagnified, to 85 mm, with an inverse telescope. In later IR experiments the lens had a focal length of 60 cm and, depending on whether or not the active mirror booster amplifier was used, a working f-number 4 or 6. That lens, located outside the tank, and the vacuum-interface window were similar to the focusing optics used in the OMEGA laser. Designed as a unit, they are corrected for spherical aberration and coma. In UV experiments the lens, located outside the tank, had a focal length of 167 cm and a working f-number 12.7.

Line-focus studies were also carried out, using cylindrical optics. In IR experiments a single-element double-aspheric lens produced a 1 mm line in the first astigmatic image plane (focal length f=30 cm, $f_y - f_x = 0.35$ cm, working f-number 3.5). In UV experiments two weakly diverging cylindrical correctors were added before the main focusing lens used in point-focus studies. Appendix C gives details about the design of the cylindrical optics and describes how the insertion of a blast window in the beam converging on target affects the distribution of intensity in the focal plane. The blast window is intended to protect from target blow-off the focusing optics or the vacuum interface window, whichever is directly exposed.

3-3. Diagnostics.

We relied mainly on soft X-ray spectroscopy to study the plasma created by the laser beam at the surface of the target. Two types of transitions were of interest to us. The transitions which end in the ground state of the Hydrogen-like or Helium-like ion give a means to

measure the populations of the excited states of these ions and, combined with some physical assumptions, the electron temperature and density of the plasma. For the materials we studied, these transitions range from $\sim$ 1.5 Å (Nickel, atomic number Z=28) to above 20 Å (Oxygen, Z=8). They were recorded with crystal spectrographs. We were also interested in the transitions ending in excited states of these same ions. They correspond to the lines which are candidates for amplification by stimulated emission. In suitable materials (from Aluminum, Z=13, to Fluorine, Z=9) their wavelengths are in the 100 Å range. They were recorded with a grating spectrograph. In some experiments a pin-hole camera was added to monitor the size and aspect ratio of the plasma. This was especially relevant when a line-focus was used. The experimental set-up, shown in Figure 3-2, took place in a large (17"high x25"diam) vacuum chamber at $\sim 10^{-5}$ torr.

3-3-a. Crystal spectrograph.

X-rays emitted by the plasma are diffracted according to Bragg's law $\lambda = 2D.\sin\theta$, where θ is the angle of incidence on the diffracting planes of the crystal and D is the interplanar spacing. The spectrum is recorded on film. Appendices A and B give details about the photometry of the spectrograph and its dispersion characteristics, respectively. As shown in Figure 3-2, it is usually equipped with a set of filters and a slit parallel to the direction of dispersion of the crystal. The filters are thin foils which, in addition to providing a spectral selection, serve as an entrance window, preventing light leaks inside the instrument. Figure 3-3 gives the transmission curves of the

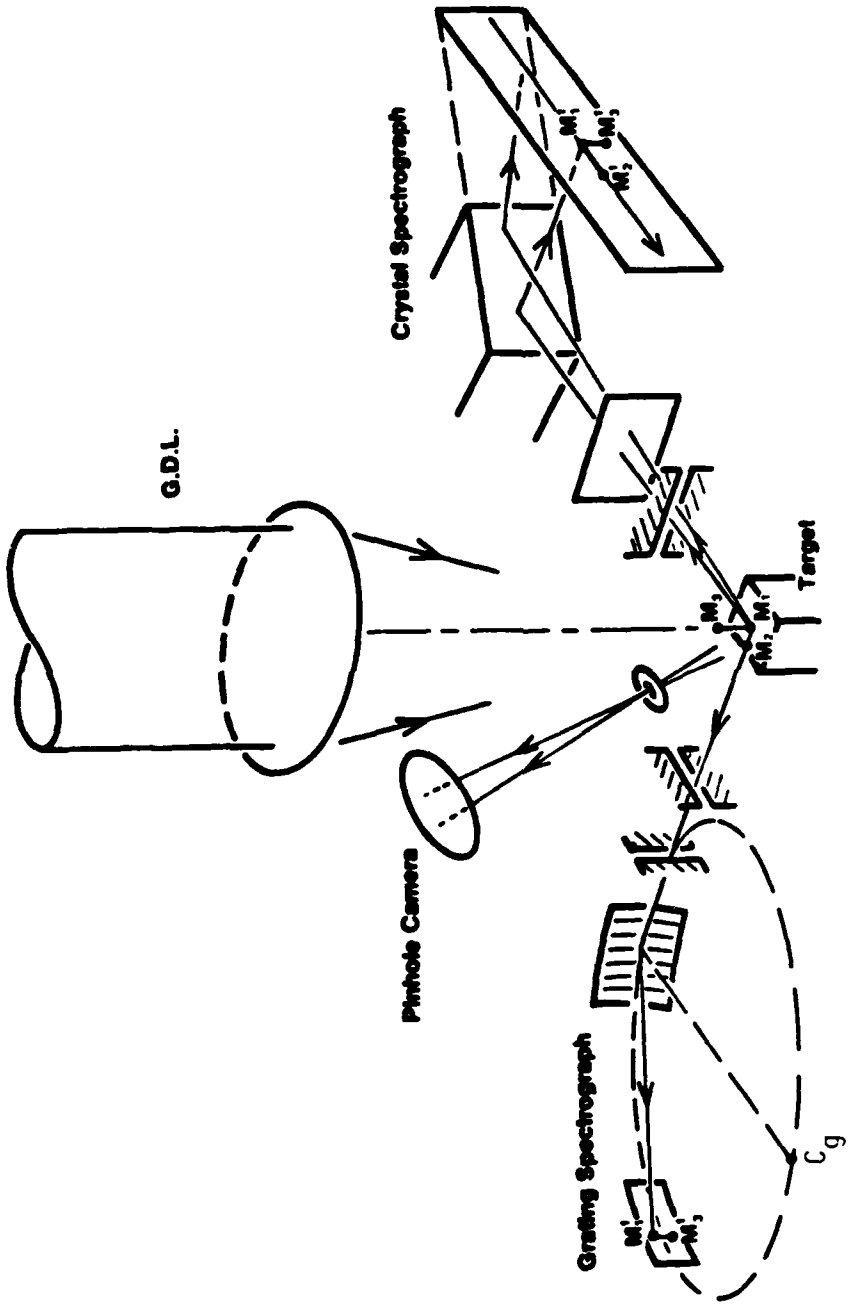

FIGURE 3-2 : EXPERIMENTAL SET-UP FOR XUV INVERSION STUDIES.

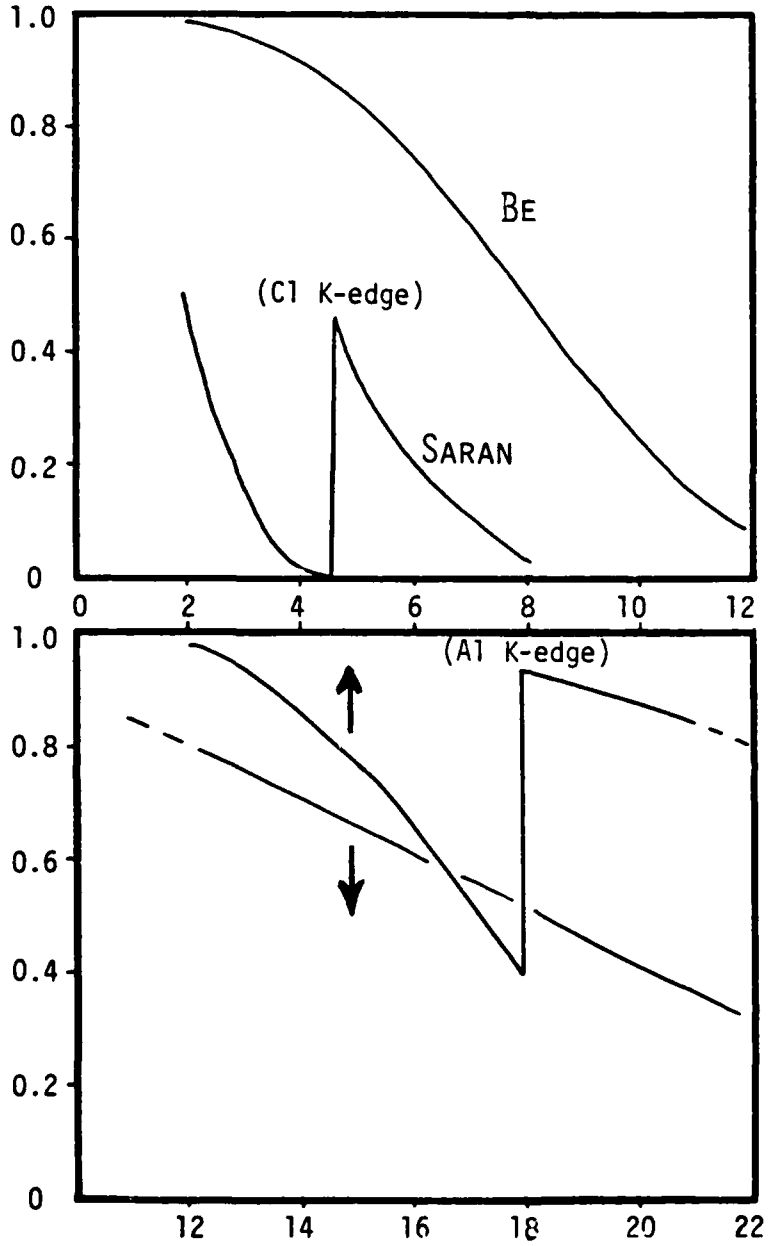

(3-3-A)
Be, Saran :
25 microns (1 mil)

(3-3-B)
Al : 0.75 micron

Figure 3-3 : Transmission of X-Ray Filters
(after Henke et al 1967).

filters we used most frequently: Beryllium, Aluminum, and Saran $(C_2H_2Cl_2)_x$. Spatial resolution is provided (i) along the normal to the target by the slit (typical width ∿50 μm), (ii) in the transverse direction by the crystal itself due to its small acceptance angle at any specific wavelength. The slit can be either a pair of semi-infinite razor-blades or two stripes (or rods). The latter case is outlined in Figure 3-4, where the laser is focussed on a flat target through an opening formed by two foils (see Chap.4). The hydrogenic and helium-like resonance series of the target material are recorded on the film. Five regions can be identified, from left to right: (I) integrated spectrum of the whole plasma, (II) shadowgram, (III) spatially resolved spectrum produced by the slit, (IV) inverse shadowgram, (V) integrated spectrum of part of the plasma. Radiation from the dense region of the plasma *near* the surface of the target does not reach the film on the right side of the slit because it is blocked by the edge of the target. Weaker emission from the under-dense region is not swamped and its features can be observed in (IV). Also the spectrum on the right side (V) corresponds to a spatial integration limited to the expanding plasma. Table 3-1 summarizes the main features of the spectrograph for each of the materials studied. Crystals with long 2D-spacings, TAP being one example, have a rather large acceptance angle roughly proportional to the wavelength. The spatial resolution provided by the crystal thus decreases when spectra from low-Z materials are recorded. For a typical distance of 8 cm between the source and the crystal, the spatial resolving element exceeds 100 μm in an oxygen plasma.

Target material (Z-number)	Wavelength range (Å)	Crystal (2D spacing)	Average angle of incidence	Acceptance angle (10^{-5} rad)	Entrance window	Film (E-K Type)
O (8)	14.5 - 22.0	TAP 001 (25.9 Å)	45°	140	Al (0.75 µm)	RAR-2491
F (9)	11.5 - 17.0		34°	90		
Mg (12)	6.5 - 9.5		18°	36	Be (12.5 µm)	RAR-2491 or NO-SCREEN
Al (13)	5.5 - 8.0		15°	28		
Si (14)	4.5 - 7.0		13°	20		
			(PET) / (Ge)	(PET) / (Ge)		
Cl (17)	3.0 - 4.5	PET 002 (8.73 Å) or GE 111 (6.50 Å)	26° / 36°	8.0	Be (25.0 µm)	NO-SCREEN
Ca (20)	2.3 - 3.3		18° / 25°	5.5		
Ti (22)	1.9 - 2.7		15° / 20°	4.5		
Fe (26)	1.3 - 1.8		11° / 15°	3.2		
Ni (28)	1.2 - 1.7		9° / 13°	2.6		

TABLE 3-1 : CRYSTAL-SPECTROGRAPH CHARACTERISTICS.

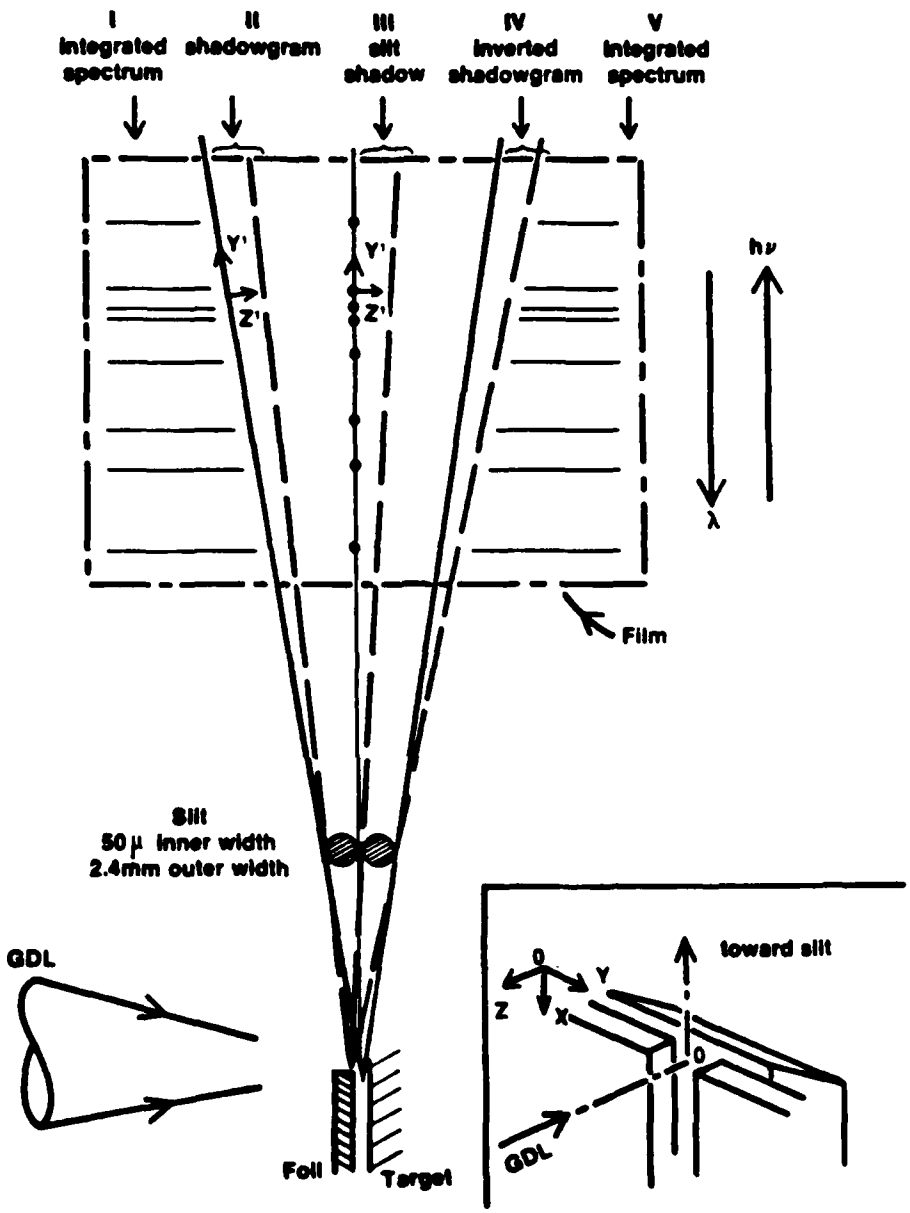

FIGURE 3-4 : GEOMETRY OF A SPATIALLY RESOLVING CRYSTAL SPECTROGRAPH.

3-3-b. Grating spectrograph. (Figure 3-5)

The grating, laid on a concave surface of radius r, not only disperses the incident XUV radiation but also forms a one-dimensional image of the entrance slit, on a curved film (radius r/2). All three elements, the slit, the grating, and the film, are on, or tangent to, the so-called Rowland circle of radius r/2 (Sawyer 1963). That arrangement insures that the imaging condition is satisfied, independent of wavelength, because the angle of incidence α is constant across the grating. An additional slit, in a direction perpendicular to the entrance slit and located anywhere between the source and the film, can provide one-dimensional spatial resolution of the plasma emission, with arbitrary magnification. The design of the spectrograph must meet the following requirements:

a/ Spectral range. It must cover a band of at least 100 Å centered around the line of interest, for a complete identification of the various ionic species in the plasma (see Appen.B).

b/ Resolution. The thermal Doppler broadening gives an upper limit for the realizable resolution of two adjacent lines:

$$(\lambda/\Delta\lambda)_D \simeq 410\ [M_{(amu)}/T_{i\,(kev)}]^{\frac{1}{2}} \qquad (3\text{-}1)$$

where M is the ion mass and T_i the ion temperature. Since typically T_i ≈100 ev in our experiments, it proved very difficult to study some promising laser-transition candidates such as $Al^{+11}(3^3D\text{-}4^3F)$ at 129.7 Å ($\Delta\lambda_D \simeq .03$ Å) which overlaps with the strong $Al^{+3}(2p\text{-}3d)$ line at 129.73 Å. Other transitions are more isolated. The nearest neighbors to the $Mg^{+10}(3^3D\text{-}4^3F)$ line at 154.4 Å are $Mg^{+4}(2s\ 2p^5\text{-}2s\ 2p^4\ 3s)$ at 152.5 Å and

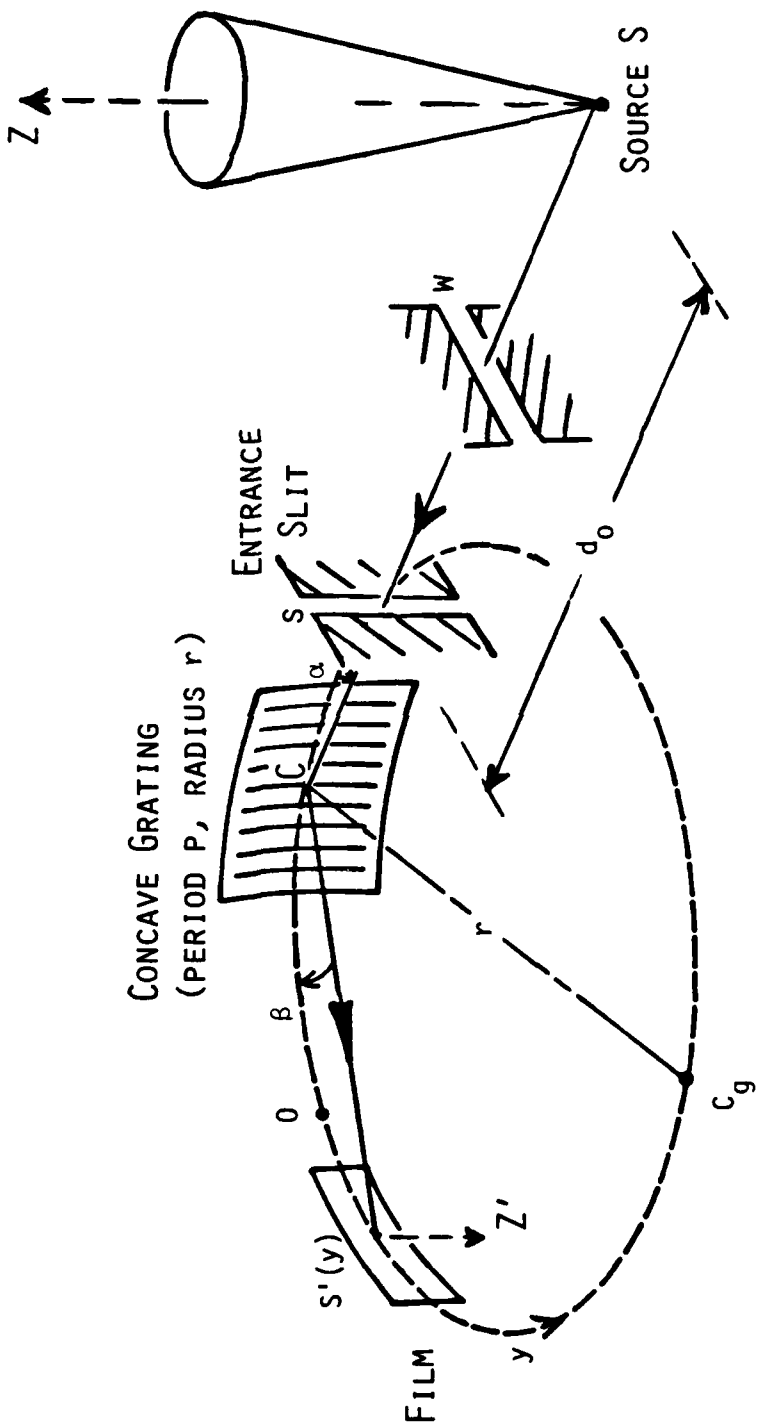

FIGURE 3-5 : GEOMETRY OF A SPATIALLY RESOLVING EUV GRATING SPECTROGRAPH.

possibly O^{+4}(2p-5d) at 153.95 Å, if the target used is free of Iron and Chromium impurities. The Balmer lines in F^{+8} are very easily resolved. Since we are only trying to record particular transitions, without studying their line-profile, a resolving power $\mathcal{R} \sim 1000$ is appropriate ($\Delta\lambda \sim 0.1$ Å).

c/ Etendue. It is difficult to set absolute specifications because in the EUV region there is no reliable calibration for the film we used, Kodak 101-01, and no data for the diffraction efficiency of commercial gratings. However one can compute the relative photometric efficiency of a particular geometry (see Appen.A).

d/ Dimensions. The optimal geometry of the spectrograph for a given wavelength is determined by the choice of grating (radius of curvature, spatial period, blaze angle). Additional constraints are introduced by the vacuum environment (inner diameter of the tank and of its ports).

A code (filename: DESIGN) has been written to select among the commercially available gratings those which are compatible with both the optical and mechanical requirements. For any grating the code computes (i) the angles of incidence and diffraction which satisfy the blaze condition at the wavelength of interest, (ii) the spectral dispersion and resolution, (iii) the relative photometric efficiency, (iv) the dimensions of the spectrograph and how they fit in the tank. For our purpose the most suitable gratings were the Bausch & Lomb models 35-5200-400, 710 and 810, of radius of curvature 400.7 mm. Their number of grooves/mm and blaze angle are (600, $1^{\circ}43'$), (1200, $3^{\circ}33'$) and (2400, $6^{\circ}54'$), respectively. They offer various compromises between proximity to the blaze condition (model 400) and good resolution (model 810).

Models 710 and 810 were ordered with a gold coating to improve their efficiency. They also had the advantage (after reduction of their blank size) of being ready for use in a rocket spectrograph lent to us by the Naval Research Laboratory, which contains a film cassette of the appropriate curvature.

The entrance slit was set to provide an angle of incidence $\alpha \simeq 5^{\circ}$. Its width was about 15 μm and its distance to the source 4-5 cm. No window was required: an aperture stop and proper shielding were enough to prevent light leaks. Eastman-Kodak, the manufacturer of 101-01 film, suggests that a distilled water presoak could minimize infectious development effects. We found that it did produce a more uniform, less granular film but the spectral lines were more fuzzy. We decided against presoaking, to avoid a loss of spectral resolution.

3-3-c. Pin-hole camera.

A pin-hole camera was used in a limited number of experiments to measure the size and aspect ratio of the X-ray emitting plasma. It was made of a ϕ 4 μm hole located d≃1 cm from the source and f≃10 cm from the film plane (Kodak RAR-2491). A 25 μm Beryllium filter limited the observation to the region $\lambda \lesssim 10$ Å (see Fig.3-3). To avoid vignetting, the observation was made at 45° from the normal to the target (which was also the laser axis), providing a 2-dimensional image of magnification $10 \times 10/\sqrt{2}$. The condition for optimal resolution (Woodall et al 1976), $\phi\,[(d+f)/\lambda df]^{\frac{1}{2}} \simeq 2$, is satisfied for $\lambda \simeq 5$ Å. The corresponding resolution element is $\Delta = 5/6\,(1+ d/f)\phi \lesssim \phi$. This was typically the spectral region we were interested in (see Chapter 4).

Chapter 4

Experimental Results

Recombination lasers in a laser-vaporized target material have been made to work in the visible part of the spectrum (Silfvast et al 1979-b, 1980). In order to extend their range to EUV and X-ray wavelengths, one needs either to consider higher stages of ionization or to move to higher atomic numbers Z along an isoelectronic sequence. How far one can go depends on the available pump, in our case a laser at 1.054 μm or 0.351 μm. This chapter presents results on the interaction between laser and matter, which were the basis for our choice of target materials and XUV transitions to investigate. A study of the target design was carried out (i) to optimize a population inversion in the XUV domain, (ii) to understand the mechanism(s) leading to that inversion. Experiments were done on the development of an actual device, which could lead to a meaningful gain measurement from recordings of the amplified spontaneous emission (ASE).

4-1. Laser-matter interaction.

A laser of intensity I is focused on a target of atomic number Z. Depending on the value of I (10^{13} to 3×10^{15} W/cm^2), a dense, highly ionized plasma can be created at the surface of targets of Z-number as high as $\sim$30. All electrons are stripped except those of the inner shell (K-shell), which have higher ionization barriers. The optical electric field (>10^7 V/cm) not only exceeds the breakdown value for solid materials but produces strong acceleration of the plasma

electrons, resulting in an electron temperature T_e in the kilovolt range. The ionization stage one reaches has an ionization potential χ of the order of 3 to 5 times that temperature (Whitney & Davis 1974), provided the plasma is heated long enough for ionization equilibrium to be established. χ is proportional to Z^2 while T_e has a relatively slow dependence on I ($T_e \sim I^{1/3}$). Hence there is a very steep scaling for the intensity necessary to reach the K-shell of targets of increasing Z-number.

The laser light actually propagates through the plasma only up to the point where the natural plasma oscillation frequency, $w_p=(4\pi e^2 N_e/m)^{1/2}$, is equal to the laser frequency w_L (N_e, electron density, e and m, charge and mass of the electron respectively, all in CGS units) (Hora 1981). This happens when $N_e(cm^{-3}) \approx 10^{21}/(\lambda_L(\mu m))^2$, called "critical density" $(N_e)_c$. The strong dependence of $(N_e)_c$ on the wavelength λ_L of the incident light shows that one may expect significant variations in the coupling of different lasers with a plasma, hence the interest in doing experiments at two different wavelengths (1.054 μm and 0.351 μm).

At short wavelength the laser radiation penetrates to higher density (10^{22} electrons/cm^3), where the plasma is more collisional and where collisional absorption , i.e. inverse bremsstrahlung, is more effective. At 1 μm there is also resonant absorption (resonant coupling between light and plasma waves) when the intensity approaches 10^{14} W/cm^2 (Max & Estabrook 1979). A large fraction of the absorbed energy is transferred into very energetic ("suprathermal") electrons instead of being used to ionize the target. Max & Estabrook (ibid.) postulate that

resonant absorption scales as $I\lambda^2$. That mechanism is dominant above 10^{14} W/cm^2 because, as the charged particles become more energetic, they exchange a relatively smaller fraction of their kinetic energy on collisions (Hora 1981). While at low intensities the fraction of incident light absorbed by the target is high ($\gtrsim$80%) at both wavelengths, at intensities of order 10^{14} W/cm^2 that fraction is typically 70% at 0.35 μm and 30% at 1 μm (Seka et al 1982). IR light is substantially less effective than the ratio of absorption would indicate because the suprathermal electrons serve as a non-useful channel for deposition of the incident laser energy.

In a plasma containing mainly Helium-like, Hydrogen-like and bare ions, the limited number of recombination channels is an advantage for the design of an X-ray amplifier because it limits the waste of pump energy. It also leads to simple spectra and, with proper filtering, the plasma can be used as a monochromatic X-ray source (Conturie & Forsyth 1980).

4-1-a. IR illumination.

Figure 4-1 shows spectra recorded with five different targets: Chlorine (Z=17), Calcium (20), Titanium (22), Iron (26) and Nickel (28). The plasmas were produced by 3×10^{15} Watts/cm^2 of IR light (175 Joules in 700 psec in a ϕ 100 μm focal spot). The pulse duration well exceded the ionization equilibrium time, which was of the order of 100 psec (Whitney & Davis 1974). The spectra were recorded with two flat-crystal spectrographs simultaneously, at 45° and 85° from the laser axis, equipped with collimating slits to reduce the background exposure due to suprathermal electrons generated around the target. The most prominent

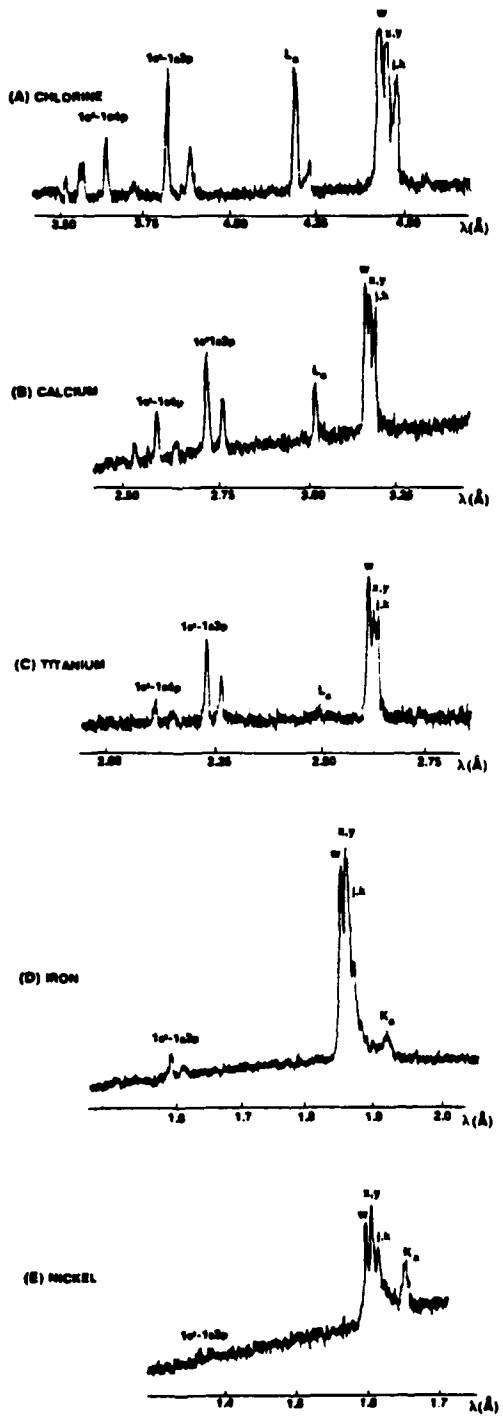

FIGURE 4-1 : X-RAY LINE EMISSION FROM VARIOUS LASER PRODUCED PLASMAS.

group of lines in each spectrum includes the Helium-like $1s^2$-1s2p transition (the so-called resonance line, labeled w), its associated intercombination lines (labeled x and y) and satellite lines arising from dielectronic recombination to doubly-excited levels in the Lithium-like ion and, for Iron and Nickel, in the Beryllium-like ion as well (labeled j and k). The relative intensity of the resonance line in that multicomponent group decreases for higher atomic numbers. It becomes harder and harder to ionize the atom up to the Helium-like stage (not to mention the Hydrogen-like stage) and the approximately constant electron temperature is adequate only for the excitation of L-shell electrons in the Lithium-like and Beryllium-like configurations. The overall spectral bandwidth of this group of lines is of the order of 1% or less so that, in many applications (Frankel & Forsyth 1979), the fine structure displayed here is unimportant.

The nearest spectral component to this group is the 1s-2p transition (labeled Lyman α) from the Hydrogen-like ion (and associated Helium-like satellites lines). As the atomic number of the target increases, the intensity of L_α drops rapidly compared to the fall-off in the intensity of the Helium-like ion resonance radiation. In the Iron spectrum the Hydrogen-like emission has disappeared altogether and the Helium-like emission is sensibly monochromatic for many applications. Similar spectra were recorded on targets of atomic number $Z \leq 14$, at lower intensity (see Sec.4-2). From these data, and using the film calibration described in Appendix A, we computed the number of X-ray photons radiated by the source. Since no significant difference was found between the two directions of observation, i.e. 45° and 85° from

the laser axis, we derived those numbers assuming that the emission from the source was isotropic. Figure 4-2 (lower curve) gives the fraction of incident laser energy converted into X-ray energy radiated in 4π on the Helium-like resonance line group. The conversion efficiency is about 10^{-3} for $Z \leq 17$ and decreases to 10^{-4} for Z=28.

For elements of atomic number Z>15, it is possible to isolate that group of lines by taking advantage of the fact that its wavelength is slightly longer than that of the K-absorption edge of the solid material. Therefore a thin foil of the target material may be used to remove the other line components present in the spectrum. An example is shown in Figure 4-3. Under identical conditions the spectrum of Chlorine was recorded (a) unfiltered (same spectrum as in Fig.4-1-a), (b) through 0.5 mil of Saran, $(C_2H_2Cl_2)_x$, (c) through 1 mil of Saran. The transmission curve of Saran is given in Fig.3-3-a. One may also notice that the continuum radiation from the source is too weak to be detected, otherwise one would see a difference in baseline level from one side of the Helium-like resonance line to the other, since the transmission through the Saran changes by more than an order of magnitude.

4-1-b. UV illumination.

A similar series of experiments was conducted using UV light (by ourselves in our experimental vacuum chamber, the "α-tank", except for Silicon and Nickel; by others in another chamber, the "β-tank", for those two elements and some duplicates, see Table A-1). Some of the spectra are shown in Figures 4-10 and 4-11. Using the same data

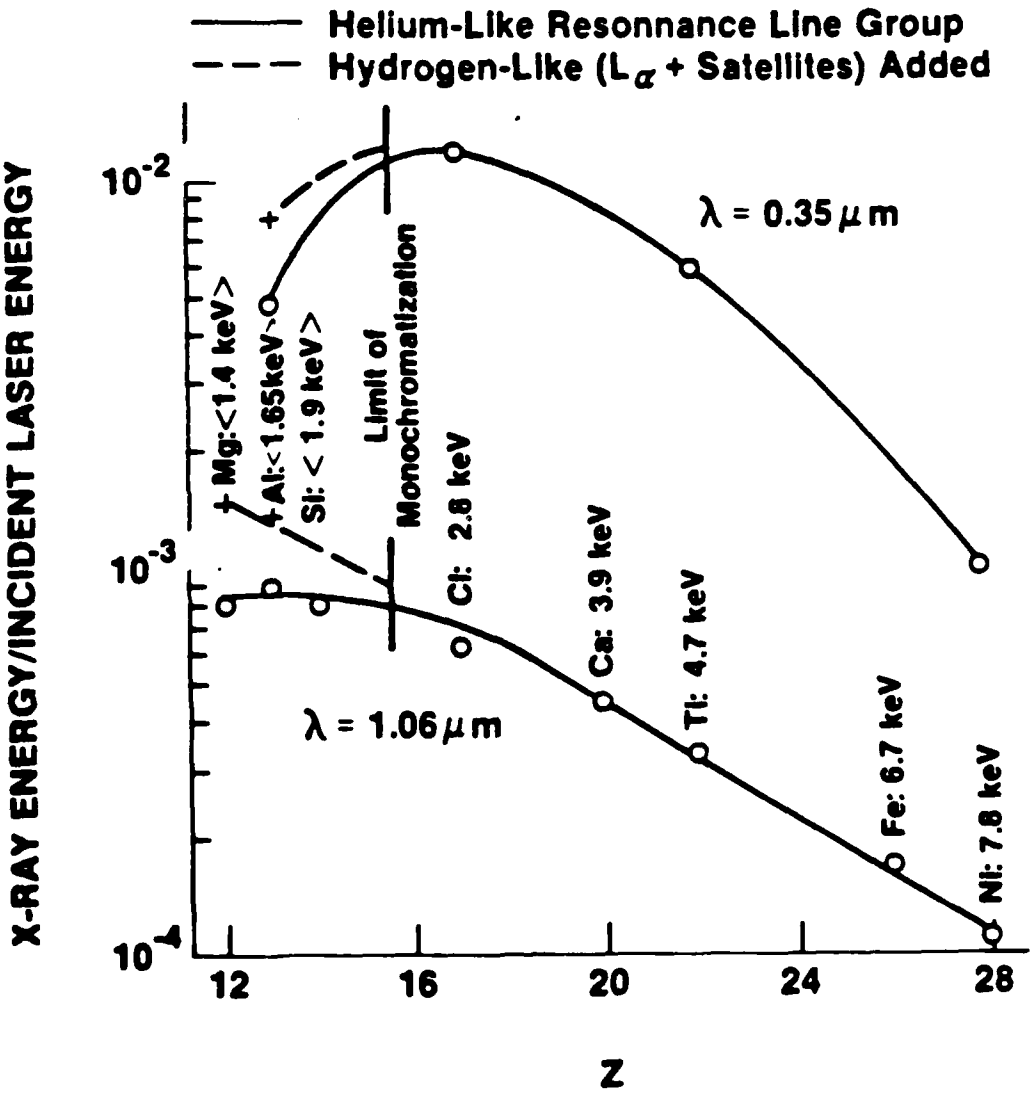

FIGURE 4-2 : X-RAY CONVERSION EFFICIENCY.

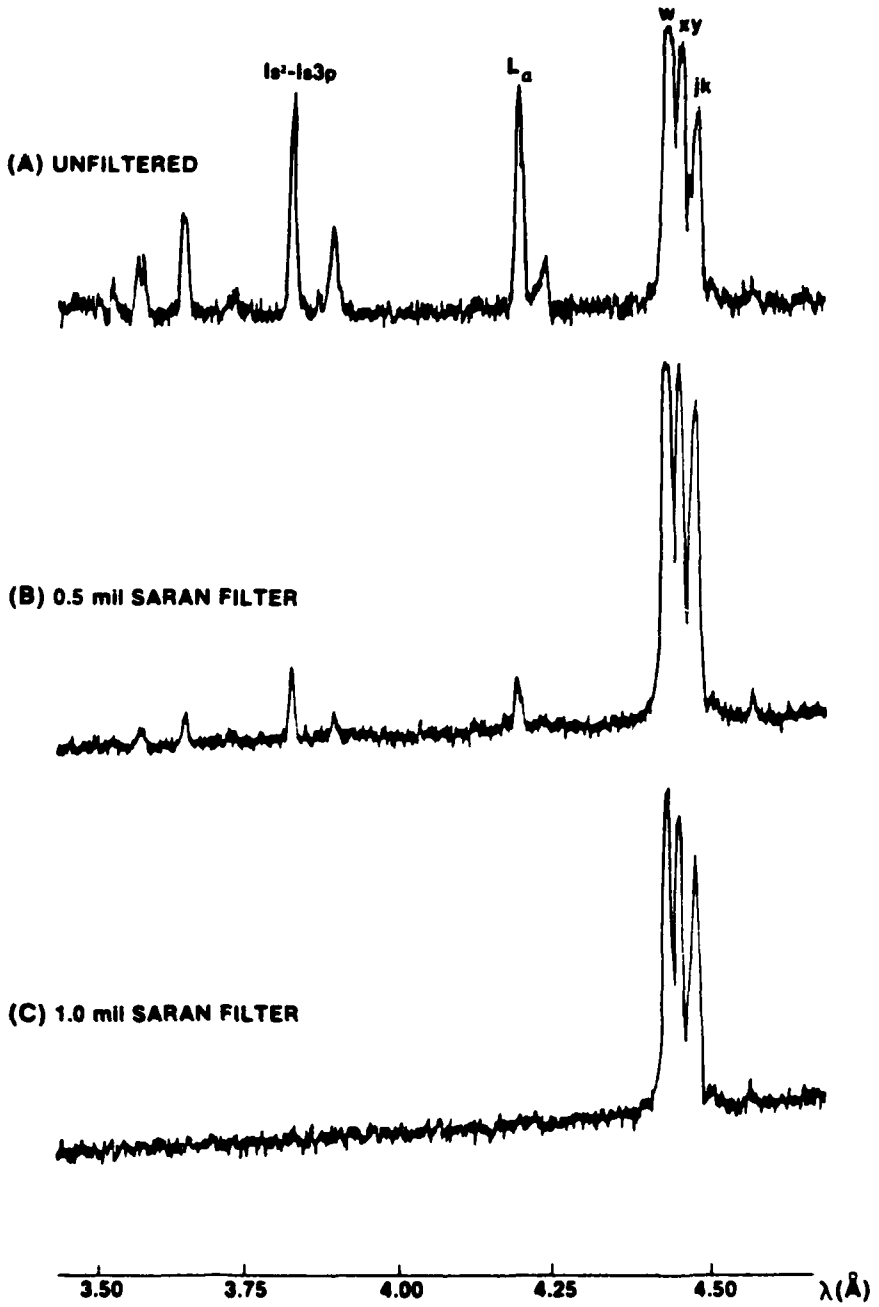

FIGURE 4-3 : MONOCHROMATIZATION OF LASER PLASMA X-RAY LINE EMISSION BY MEANS OF FOIL FILTRATION.

reduction procedure as in the IR case, we computed the X-ray yield on the Helium-like resonance line group for each target material. As is seen in Fig.4-2 (upper curve), UV irradiation is more efficient in producing X-rays, by a factor ($\simeq$10) which decreases with increasing Z. This observation at high Z is believed to be due to the significant presence, in IR laser irradiation, of suprathermal electrons which can contribute to the excitation of high energy X-ray lines (Yaakobi et al 1981-a). The main reason for the decrease in line intensity with increasing Z is the temperature profile in the target (see Fig.1-1). Lines of higher-Z ions are emitted mostly around peak temperature near the critical layer (where the laser deposits most of its energy), whereas lines of lower-Z ions come from inside the critical layer where the temperature is lower and the density higher.

The conclusions drawn from these experiments are the following.

a/ Laser-produced plasmas on targets of atomic number Z>15 can be used as very bright, sub-nanosecond point-sources of monochromatic X-rays. Their applications as a probe of transient phenomena include: (i) "Back-lighting" of micro-balloons in laser fusion (Key et al 1978). An X-ray source synchronized with the laser driving the target is used as a probe to study the highly-compressed imploded fuel; (ii) X-ray diffraction of biological samples. Progress has been made in that direction with the recent recording of the patterns from crystal proteins (Frankel & Forsyth 1982); (iii) Photopumping leading to lasing in the soft X-ray region (Jaegle, et al, 1981); our study of an XUV amplifier was not, however, focused in that direction; (iv) K-edge

fine-structure absorption studies (Yaakobi, et al, 1980).

b/ Short wavelength lasers couple their energy to the target more efficiently, resulting in a higher X-ray yield. Using UV illumination instead of IR leads to the formation of a higher density plasma, at approximately the same temperature, a significant advantage for the design of an X-ray amplifier based on three-body recombination (see Chapter 2). In such an amplifier one wants to form a large reservoir of bare nuclei (for recombination into Hydrogen-like ions), or of H-like ions (for recombination into Helium-like ions). With the lasers available to us, this sets a limit for the atomic number of the target, $Z \lesssim 15$.

4-2. Target design to achieve a population inversion.

In a dense, almost fully ionized plasma such as can be created at the surface of an aluminum target (Z=13), the recombination cascade is dominated by collisions, which tend to populate high-lying quantum states of the recombining ion (see Chapter 2). In particular the three-body recombination rate is proportional to N_e^2 while the radiative recombination rate goes as N_e. Also the probability of a three-body event is strongly dependent on the electron temperature T_e: it increases more rapidly than that of a radiative decay as T_e cools down (Griem 1964). Therefore, the idea is to produce a high density, low temperature plasma from an initially hot plasma (Gudzenko & Shelepin 1965). One may rely on free expansion for the cooling (Irons & Peacock 1974, Jacoby et al 1981) but it is accompanied by a large drop in density, greatly reducing the possibility of significant gain. An

alternate solution is to bring the plasma in contact with a heat sink (Bhagavatula & Yaakobi 1978): a foil placed a few hundred microns in front of the target allows a rapid cooling of the expanding plasma at an early stage of its recombination, by heat conductivity.

We pursued the latter approach and devised the target shown on Figure 4-4-b. The foil is designed as a slit which, if properly dimensioned, has several advantages: (i) large surface of contact with the plasma, without vignetting the incident laser beam, (ii) compatibility with a point-focus or a line-focus illumination, with a direction of symmetry ("x" on Fig.4-4-b) for a potential X-ray amplifier, (iii) good view of the interaction region for the diagnostic instruments. It also allows one, by removing one-half of the slit, to study the plasma-foil interaction separately from possible nozzle effects through the aperture.

4-2-a. Parametric study with IR illumination.

At 1.054 μm, the target (Fig.4-4-b) was studied over a parameter space which included (i) dimensions of the foil (gap width and distance to the target, (ii) foil and target materials, (iii) laser characteristics (energy, pulse width). To provide a baseline for the discussion of these parameters, we present on Figure 4-5 a spectrum (shot #972) which illustrates features observed in much of the data.

The laser beam (56 J, 600 psec, f/3.5) was focused on an aluminum slab. Two 80 μm foils of lead (Pb, Z=82) forming a 300 μm slit were placed 200 μm in front of the slab. The spectrum, recorded with a crystal spectrograph, is a direct illustration of the geometry shown in

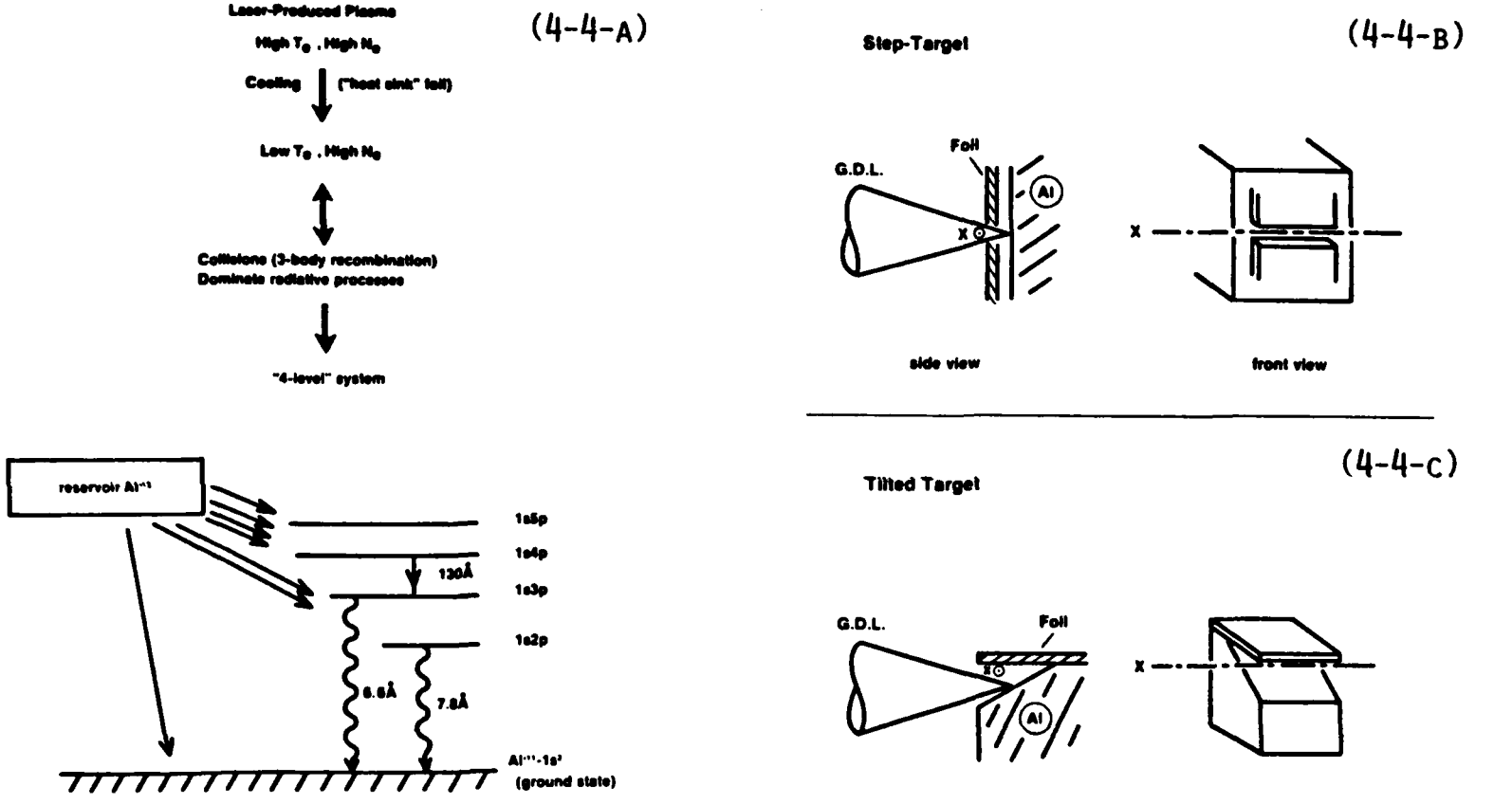

FIGURE 4-4 : SCHEME FOR AN X-RAY AMPLIFIER / TARGET GEOMETRY.

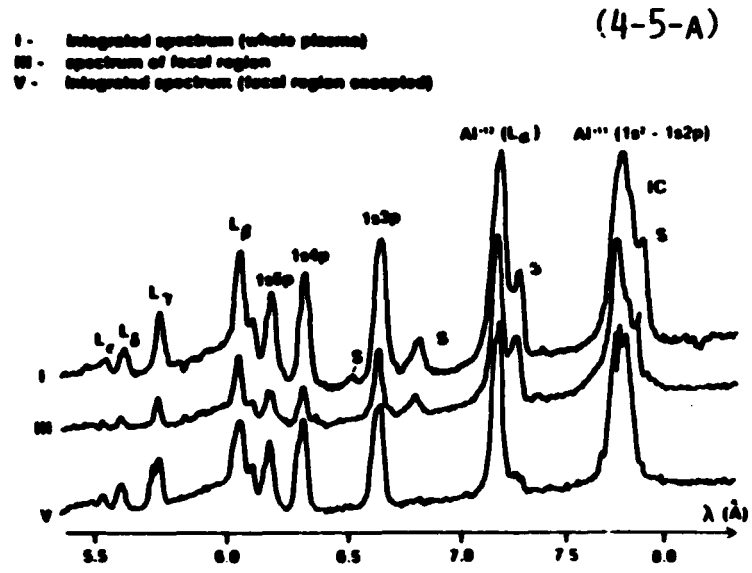

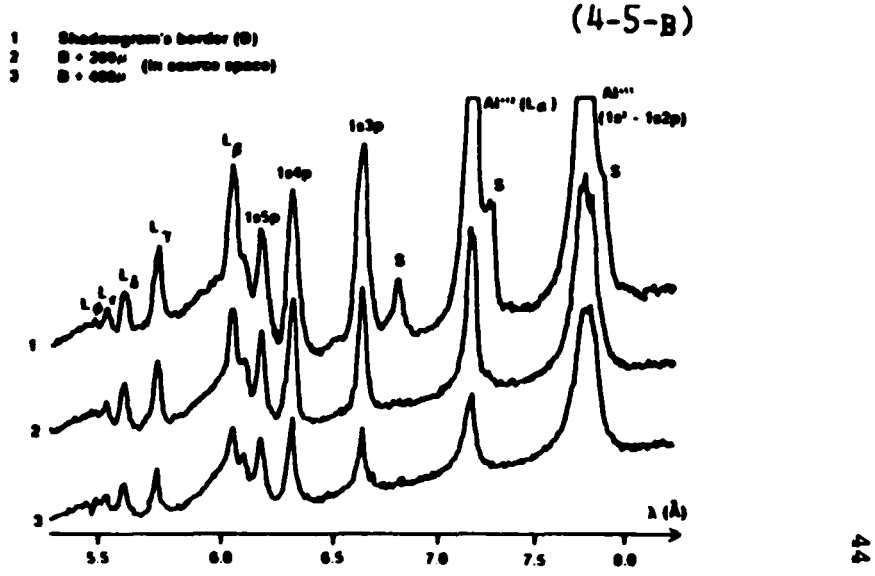

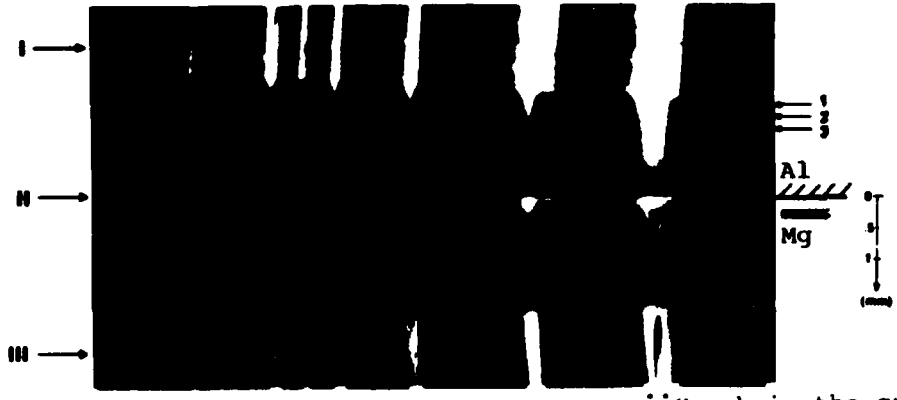

**Crack in the crystal

FIGURE 4-5 : REFERENCE TARGET / IR ILLUMINATION.

Aluminum (slab) + Lead (slit foil),

Shot #972 (56 J, 600 psec).

Fig.3-4. The set-up was such that the magnifications were $y'/y \simeq 2$ and $z'/z \simeq 3.3$ (Al^{+11}, resonance line) to 4.2 (Al^{+12}, Lyman δ). The scale on Fig.4-5 (and all through Fig.4-16) refers to the source space.

Figure 4-5-a compares a densitometer scan of the dense region of the plasma (III) with those of the two spatial integrations (I) and (V). Note in (V) the absence of satellite lines and, compared to (III), the smoother decrease along the H-like Lyman series (L_α has about the same intensity in the two spectra): as the electron temperature T_e drops, recombination into the higher excited states is favored. In (V) the $1s^2$-1s3p, $1s^2$-1s4p He-like lines and even the L_β, L_γ lines present ratio anomalies large enough to suggest population inversion on average over the expanding plasma.

The last discernible lines in the H-like and He-like series (1s-7p and $1s^2$-1s6p respectively) give an indication of the electron density N_e in the focal region. Using the Inglis-Teller relation (1939), although it may not be valid at temperatures higher than 500 eV, leads to $N_e \simeq 0.75 \times 10^{21}$ cm^{-3} in one case, $N_e \simeq 1.7 \times 10^{21}$ cm^{-3} in the other. This corresponds approximately to the critical density $(N_e)_c = 10^{21}$ cm^{-3} of the plasma at $\lambda_L = 1.054$ μm. The $Al^{+11}(1s^2\text{-}1s2p)$ resonance line is not well resolved from its associated intercombination and satellite lines but it appears to have an intensity comparable to that of $Al^{+12}(L_\alpha)$. Thus the electron temperature, on the basis of the collisional-radiative model which applies at high density (Bates, et al, 1962-a), is estimated to be $T_e \simeq 750$ eV.

The diameter of the plasma in the focal region is about 150 μm. It may be larger than that of the focal spot from GDL although it is in

agreement with the knife-edge test done on the alignment laser, a Nd:YAG which goes through the same optics as GDL. Thus the intensity on target is $\sim 5 \times 10^{14}$ W/cm^2. Part of the plasma is fully ionized: the emission on the Lyman series when the expanding plasma reaches the foil is produced by the recombination of Al^{+13}. The slight asymmetry in the wings is due to a miscentering of the GDL beam through the foil. Its shape is the result of two effects: (i) the plasma expands around each foil i.e. towards the center, (ii) the plasma emission reflects the distribution of the electronic heat sink, dense near the foils and also at some distance along the axis where its components merge.

Figure 4-5-b presents scans at several locations of the shadowgram. Scan #3, which represents an integration over the region y>400 μm, shows an intensity inversion between the Al^{+11} lines $1s^2$-1s3p, $1s^2$-1s4p and possibly between the Al^{+12} lines L_β, L_γ (the ambiguity due to the Helium-like continuum precludes a definite conclusion). The data reductions from the spatially resolved spectrum and the shadowgram yield consistent results: away from the foil the emission on the Al^{+11} lines $1s^2$-1s3p, $1s^2$-1s4p, $1s^2$-1s5p follows an exponential decay $\exp(-z/z_o)$ with $z_o \simeq 170$ μm, 340 μm and 430 μm respectively. Intensity inversion on 1s3p/1s4p and 1s3p/1s5p occurs 200 μm and 300 μm away from the foil while it is never observed on 1s4p/1s5p. Data are not presented for L_β and L_γ due to the ambiguity mentioned earlier.

4-2-a-1. Dimensions of the foil.

Changes are observed when the geometry is modified. (i) Localized cooling with very little deviation of the plasma expansion is observed on shot #547 (see shadowgram, Figure 4-6-a), where the foil is a

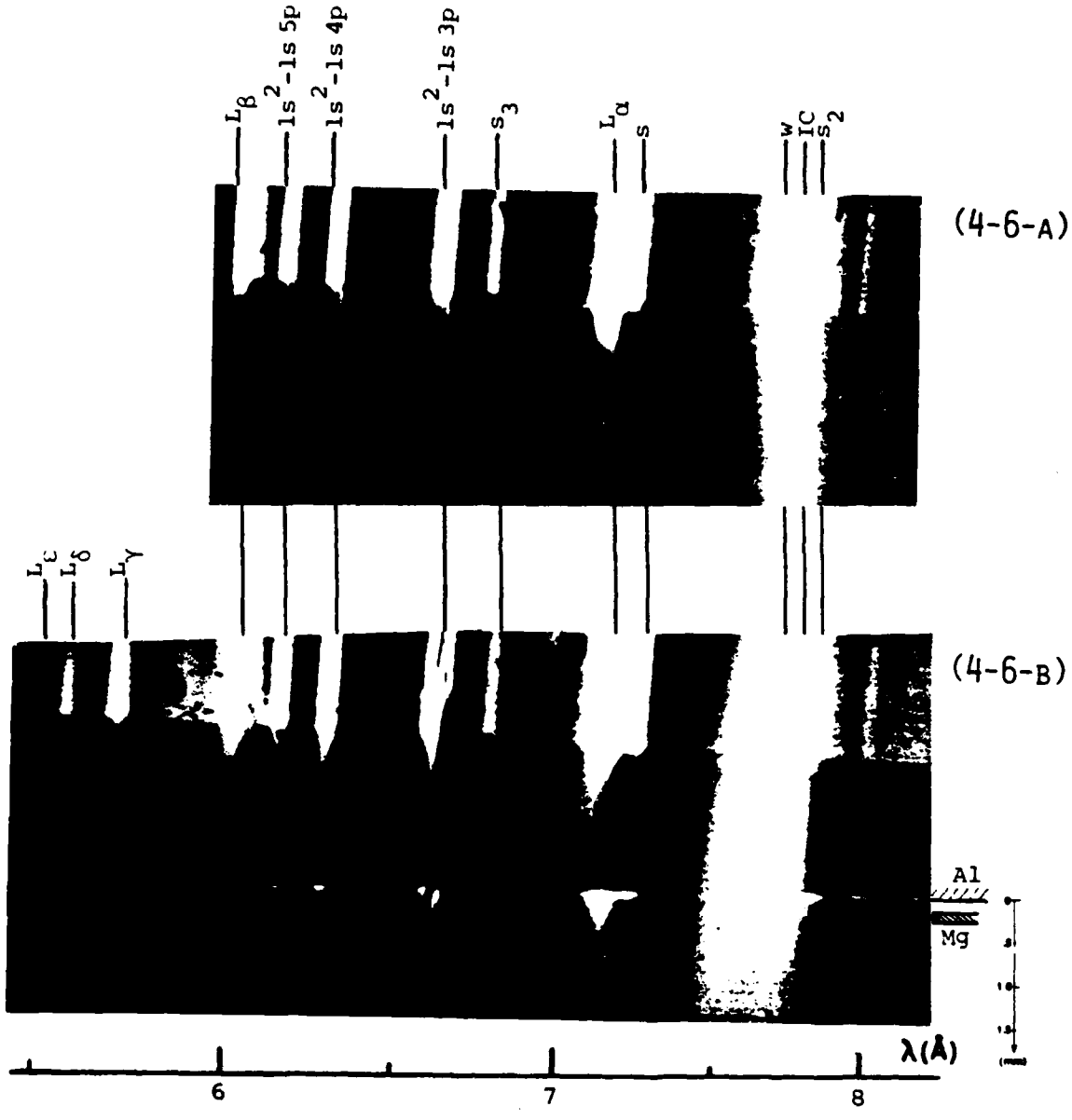

FIGURE 4-6 : LATERAL TRANSLATION OF THE FOIL.

Aluminum (slab) + Magnesium (half-plane foil),

a) Shot #547 (44 J, 600 psec, IR), foil at the edge of the beam

b) Shot #697 (63 J, 600 psec, IR), foil moved in.

half-plane of magnesium (thickness ∿100 μm, distance to the slab ∿ 150 μm) positioned just out of the incident beam (44 J, 600 psec). When the foil is moved in (Fig.4-6-b, shot #697, 63 J, 600 psec), the plasma emission follows the contour of the foil. (ii) An efficient cooling is achieved when the foil is 200 μm to 300 μm wide, about 200 μm from the slab. The slit is a compromise between obstruction of the laser beam and proximity to the plasma expansion.

4-2-a-2. Foil and target materials.

The choice of foil material does not strongly affect the result. One shot (#978, 54 J, 600 psec, see Figure 4-7-b) was taken with a slit made of one half-plane of magnesium, the other of lead for direct comparison. No clear spatial asymmetry is apparent, which is consistent with what is observed on shots taken with either type of foil alone. In many subsequent experiments, we used a foil of Titanium (Z=22) because (i) it does not lead to spectral overlap with the lines from the original plasma (Z<15), (ii) it has a relatively high melting point, 1668^{o}C, and does not produce a blow-off damaging to the optics (as a Pb foil does).

Other target materials were used: Magnesium (Z=12) and Silicon (Z=14). The results are shown in Fig.4-7-a (shot #4123, 54 J, 600 psec) and 4-7-c (shot #1740*, 20 J, 600 psec), respectively. As before, there is reemission of the original plasma as it reaches the vicinity of the foil, and population inversion occurs in the downstream expansion.

That set of data allows us to put aside models based on resonance mechanisms, such as photo-pumping (Bhagavatula 1980) and charge transfer (Elton et al 1979). Both are strongly material dependent. In

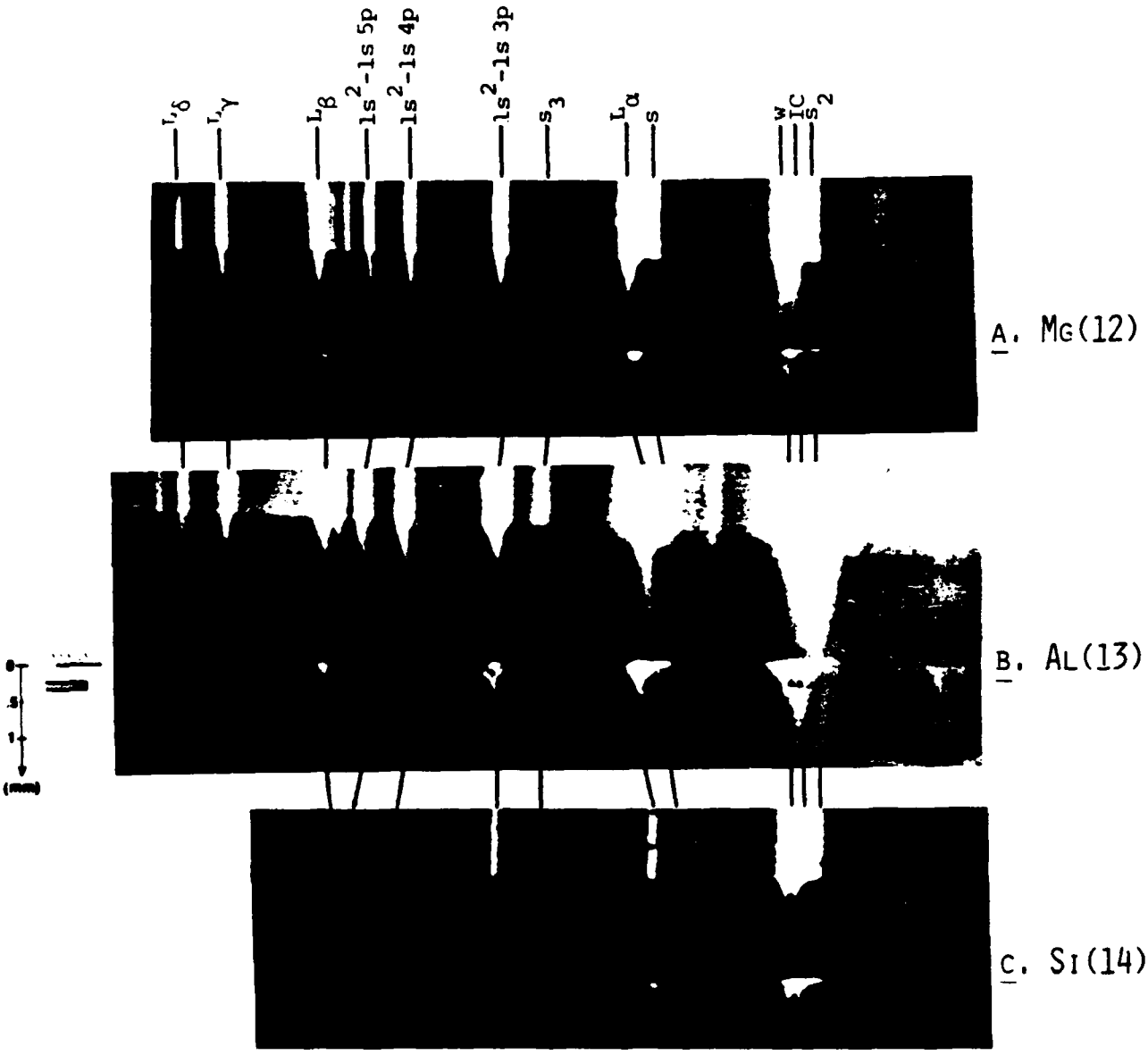

FIGURE 4-7 : TARGETS OF DIFFERENT MATERIALS (SLAB + FOIL).

a) Shot #4123 (54 J, 600 psec, IR), Mg + Ti

b) Shot # 978 (54 J, 600 psec, IR), Al + Mg/Pb

c) Shot #1740* (20 J, 600 psec, IR), Si + Mg

photo-pumping there must be resonant absorption of the pump radiation, a condition not satisfied in most combinations of target and foil materials mentioned above. In charge transfer it was suggested (ibid.) that Neon-like ions, which have a closed shell and are expected to be long-lived even in a transient plasma, could transfer an electron selectively to an excited level of hydrogenic or Helium-like ions of the same species. This would require a match between the binding energies of the electron in the two configurations, with some energy defect to insure an exothermic exchange. These conditions could be met in Al or Mg but not in Si.

To confirm the hypothesis of a lowering of the plasma temperature near the foil, leading to enhanced recombination, we used a target of alumina (Al_2O_3) instead of aluminum. Figure 4-8-b shows the oxygen (Z=8) spectrum recorded on shot #1108* (30 J, 600 psec, Mg foil). In the focal region (which is within the field of view of the spectrograph, as indicated by the recording of the Al^{+12} Lyman α line in third order), the temperature is too high for fully-stripped oxygen ions to recombine. Most of the line emission occurs near the foil. Without foil the emission is more diffuse, because it occurs during the plasma expansion, and only the space-integrated spectrum can be recorded (see Fig.4-8-a, shot #970*, 20 J, 600 psec).

4-2-a-3. Laser characteristics.

Most of the data presented so far were recorded on IR shots of energy $\sim$50 J and duration $\sim$600 psec. While plasma reemission near the foil is observed at laser energies as low as 6 J, the observation of a population inversion in the expanding plasma of, say, Al^{+11} requires at

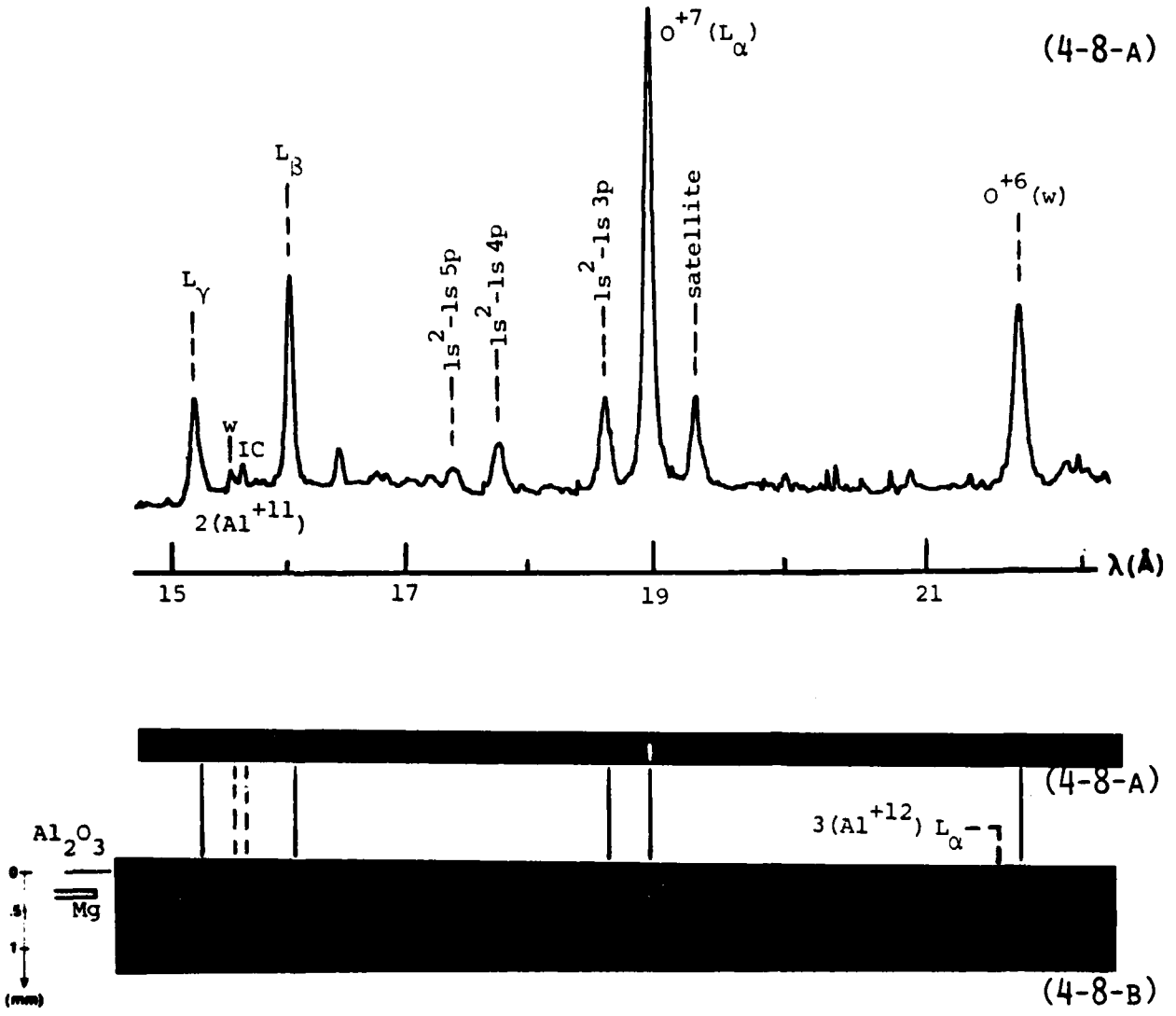

FIGURE 4-8 : OXYGEN SPECTRUM. AL_2O_3 TARGET.

a) Shot #970* (20 J, 600 psec, IR), flat target.

b) Shot #1108*(30 J, 600 psec, IR), Mg foil added.

least 20 J. Below 20 J, the pump is not strong enough to create a large reservoir of bare nuclei or hydrogenic ions. Above 50 J, most of the energy increment contributes to the production of suprathermal electrons, which do not participate in the formation of that reservoir. A few spectra were recorded with shorter pulses (~150 psec). The familiar pattern of X-ray emission in the focal region and near the foil was observed again but without population inversion. The onset of suprathermal electrons, which depends on the laser intensity on target, occurs at a lower energy level than in long pulse operation. The pump operates for a shorter time, without improved efficiency or any other advantage.

4-2-a-4. Other targets.

Two variations of the step target were studied, with the same idea of enhanced recombination in mind. Both were designed (i) to keep the plasma density high by containing its expansion, (ii) to improve the cooling by increasing its area of contact with the heat sink.

The first was a channel (Reintjes et al 1978, Silfvast et al 1980), i.e. a thick foil whose distance to the target was zero. Figure 4-9-a (shot #1826*, 51 J, 600 psec) shows the spectrum obtained with an Al target and a Mg channel (300 μm thick, 250 μm wide). The second was a tilted target (see Fig.4-4-c). Even though the expansion is expected to be mainly in the direction of the incident laser (Hora 1981), the design lengthens the interaction time between the plasma and the foil. Fig.4-9-b (shot #3091, 66 J, 750 psec) shows the spectrum obtained with an Al target and a Mg foil.

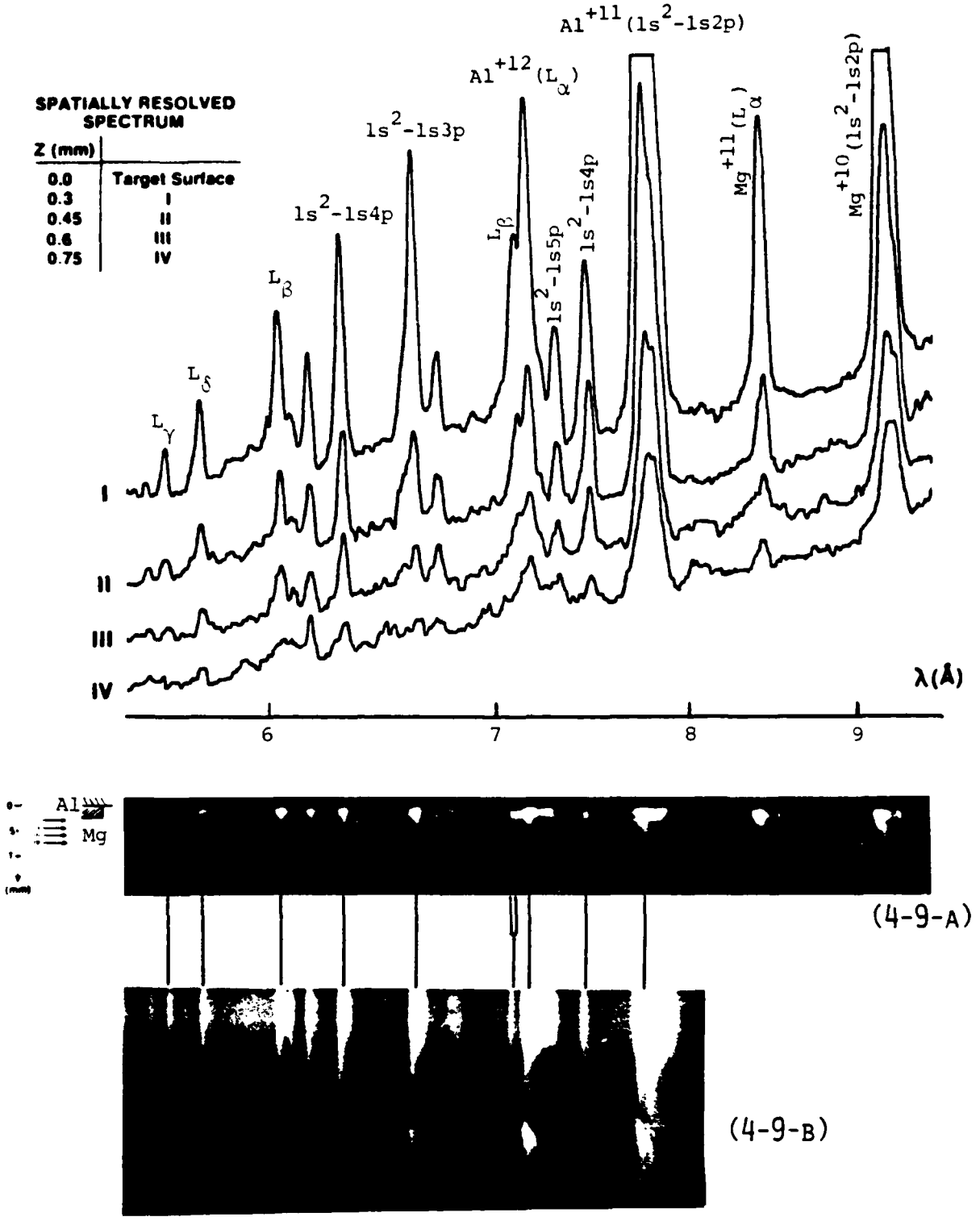

FIGURE 4-9 : ALTERNATE TARGET DESIGNS.

Aluminum (slab) + Magnesium (foil),

a) Shot #1826* (51 J, 600 psec, IR), Channel Target,

b) Shot #3091 (66 J, 750 psec, IR), Tilted Target.

In both cases a population inversion is observed between the levels n=4 and n=3 of the Al^{+11} ion. The inversion is of a magnitude and at a location in the expansion similar to that observed in shot #972 (Fig.4-5). Hence it appears that what counts to produce enhanced recombination is the presence, at an early stage of the expansion, of a foil. The geometry of the foil determines the path of the plasma flow, but the recombination is not influenced by it being a barrier (Fig.4-6), a nozzle (Fig.4-5) or a channel.

4-2-b. UV illumination.

Experiments on step targets, similar to those described in Sec.4-2-a, were done with the frequency-tripled GDL laser (0.351 μm) to take advantage of the superior coupling of short wavelength light to the target. Figure 4-10 shows the spectrum recorded when the UV laser (shot #2789, 20 J, 500 psec) is focused in a ϕ 100 μm focal spot at the surface of an aluminum slab. Two 100 μm foils of titanium, forming a 200 μm slit, were placed 200 μm in front of the slab. As before, aluminum X-ray emission is observed mainly in the focal region at the surface of the target and along the contour of the foil, with a more diffuse tail as the plasma expands beyond the foil. As is apparent on the densitometer trace, there is an intensity inversion at distances 600 μm into the expansion between the $1s^2$-1s3p and $1s^2$-1s4p lines in Al^{+11}, showing the possibility of gain at 129.7 Å on 3^3D - 4^3F. Without foil, emission strong enough to be recorded occurs only in the focal region where high density and temperature adequate for line excitation can be found along the gradient from the hot corona to the cold target

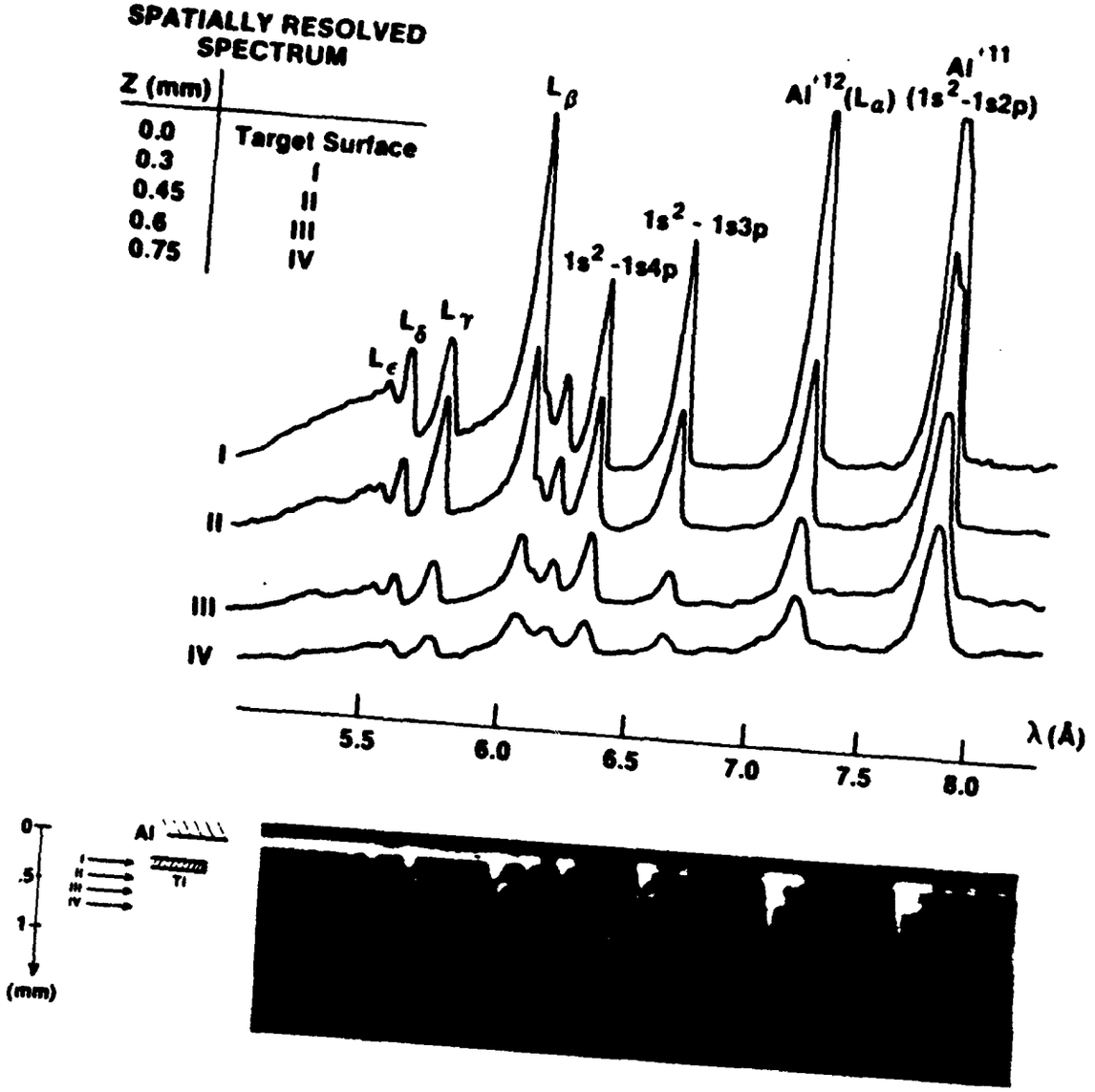

FIGURE 4-10 : REFERENCE TARGET / UV ILLUMINATION.

Aluminum (slab) + Titanium (slit foil),
Shot #2789*(20 J, 500 psec).

mass. The expanding plasma, initially at high temperature, is too dilute for measurement by the time it has cooled down to the point where the rate of ion recombination (and line radiation) is largest.

An attempt was made to scale the experiment up to higher atomic numbers. The UV laser was focused on a target of similar geometry, but whose slab and foil were of Titanium (Z=22) and Magnesium, respectively. Once again the choice of foil material was mainly based on avoiding spectral overlap. Figures 4-11-a and 4-11-b show the spectra recorded when the UV laser is focused on such a target (shot #3712*, 37 J, 1 nsec), and on a flat Titanium target without foil (shot #3713*, 32 J, 1 nsec), respectively. Because of the higher atomic number compared to Al, it is harder to achieve the corresponding ionization state. Thus, the smaller reservoir of hydrogenic and fully-stripped ions leads to a much reduced level of recombination into the helium-like stage when the plasma reaches the foil. Line reemission is still apparent on the Helium-like resonance transition group ($1s^2$-$1s2p\ ^1P$ & ^3P) and, very weakly, on the $1s^2$-1s3p and $1s^2$-1s4p transitions. There is evidence of enhanced recombination, as can be seen from the significant increase of the ratio $1s^2$-1s4p/$1s^2$-1s3p in the expansion, to $\sim$l about 500 μm from the target surface. The result, while marginal, illustrates the possibility of scaling towards shorter wavelengths when larger pump lasers are available. The transition $Ti^{+20}(3^3D$-$4^3F)$ is at 43 Å.

4-3. Design of an ASE device.

An XUV amplifier requires an elongated medium (i) to maximize the length of amplification, (ii) to permit an unambiguous diagnostic of

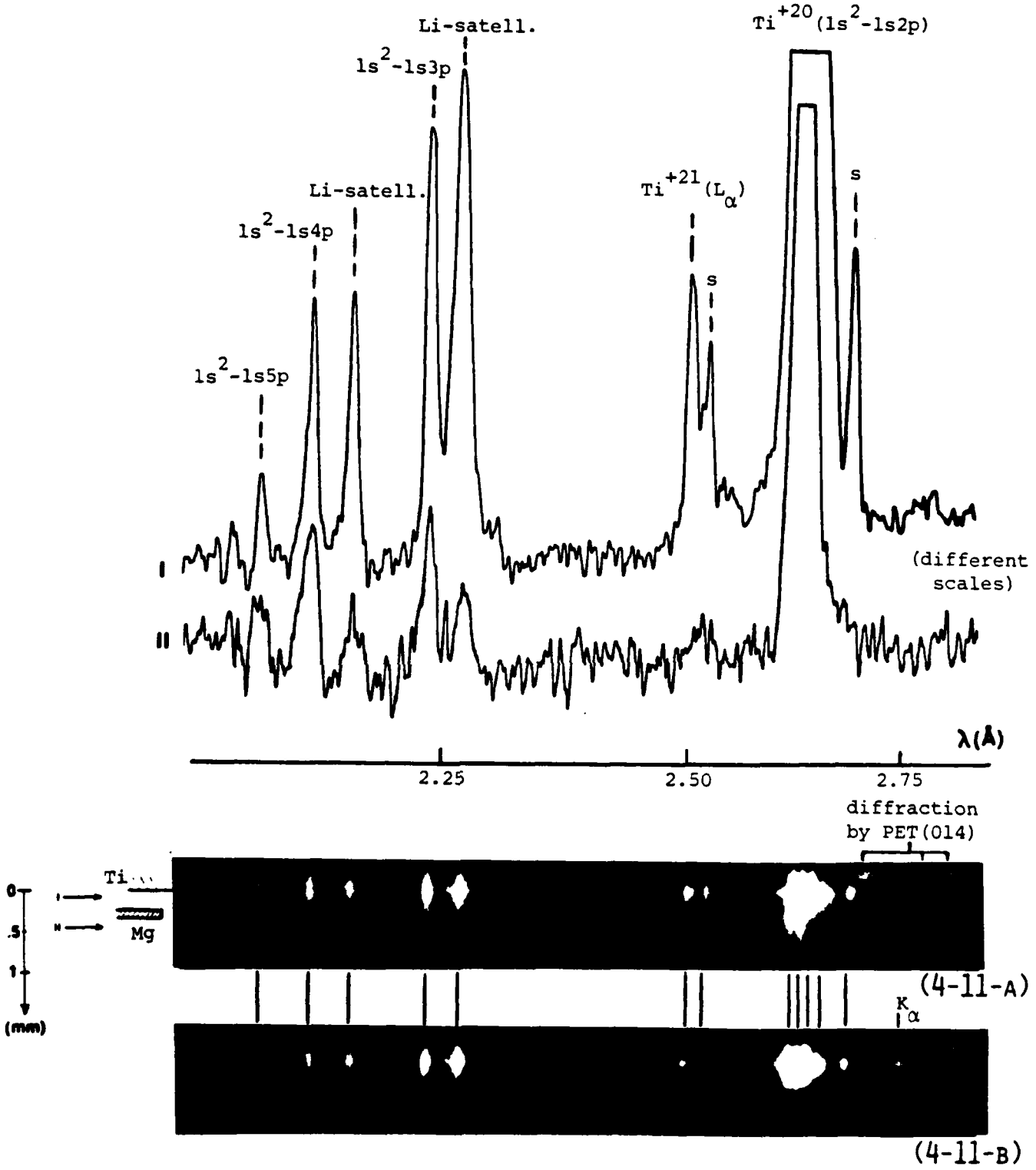

FIGURE 4-11 : TITANIUM TARGET.

a) Shot #3712*(37 J, 1 nsec, UV), Magnesium foil added,

b) Shot #3713*(32 J, 1 nsec, UV), flat target.

gain from the spatial distribution of the amplified spontaneous emission (Slaymaker 1978). That requirement, in schemes involving traveling waves (Chapline & Wood 1974, Duguay 1976), is an essential part of the design. In a steady-state type of pumping such as ours, the best approach is to use cylindrical optics to form a line-shaped plasma. The optics are described in Appendix C. However, as the focal area gets larger with a cylindrical lens, the intensity on target decreases and one needs to use materials of lower atomic number (Z) to form a fully ionized plasma. In addition, as Z decreases, the recorded spectrum is simpler and the detection of the relevant spectral lines is made easier.

4-3-a. Aluminum (Z=13) and Magnesium (12).

Experiments with IR light were done using a double aspheric lens which produced a 1 mm line-focus of aspect ratio ∿10:1. Figure 4-12-a shows a pin-hole picture of the X-ray emission (5 Å < λ < 9 Å) from the plasma formed at the surface of an aluminum target (shot #3311, 78 J, 600 psec, Mg foil). Figure 4-12-b shows a simulation with the ray-tracing code LINFOC (see Appen.C). However the data taken with crystal and grating spectrographs on that shot (as well as others) point to several difficulties:

a) the intensity on target ($I \simeq 10^{14}$ W/cm^2) is too low to create a population inversion in hydrogenic or helium-like aluminum, at least not one which could be recorded on a time-integrated basis.

b) target oxidation prior to the onset of vacuum leads to the recording, in the 100 Å region, of an oxygen spectrum superimposed on the spectrum of interest.

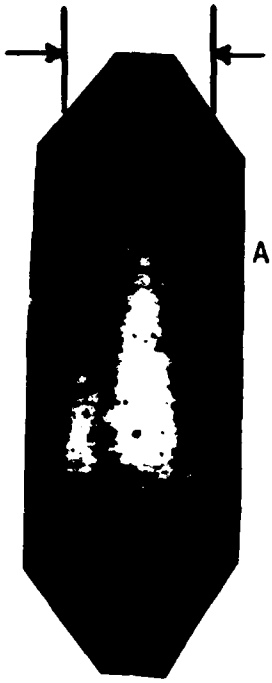

A- PIN-HOLE PICTURE.

Aluminum (slab) + Magnesium (foil)

- Notice the X-ray emission near the foil, on the left side of the slit.
- Vertical dimension reduced by $\sqrt{2}$ (observation at 45^{o}).

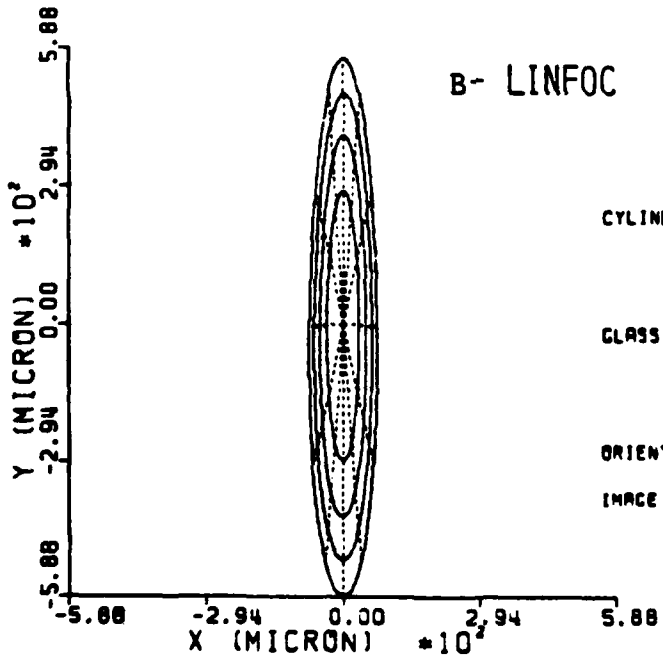

B- LINFOC

CYLINDRICAL LENS :
BEAM DIAMETER = 86.00 MM
FOCAL LENGTH (X) = 300.00 MM
FOCAL LENGTH (Y) = 303.50 MM

GLASS PLATE (BLAST SHIELD) :
THICKNESS = 6.00 MM
REFRACTIVE INDEX = 1.500
TILT / Z-AXIS = 10.00 DEG.MIN

ORIENTATION LENS/PLATE = 0.00 DEG.MIN

IMAGE PLANE Z = -2.25 MM

FIGURE 4-12 : LINE-FOCUS.

a) Shot #3311 (78 J, 600 psec, IR)

b) LINFOC simulation.

c) laser-transition candidates, such as $Al^{+11}(3^3D-4^3F)$ at 129.7 Å, cannot be resolved because they overlap with strong lines from other ionic stages of Al or O (see Chap.3).

All these problems can be solved by using UV light and a lower-Z target (see next section). It may, however, be possible to build a device and do the diagnostic without significantly changing Z. Problem b can be solved by having a pre-shot on the target (while protecting the foil and closing the aperture of the spectrographs), to remove the thin layer of surface oxide. An illustration of that idea is shown on Figure 4-13, which is a comparison of the spectrum from a flat aluminum target with and without a "clean-up" shot beforehand. The oxygen lines disappear almost completely when that procedure is used (shot #4021). Problem c can be solved by using a magnesium target (Z=12). Figure 4-14 shows that the line $Mg^{+10}(3^3D-4^3F)$ at 154.4 Å can be resolved from its neighbors. The full spectrum in the range 45 Å-200 Å was recorded on film (see Chap.3), the wavelength scale was determined with the code GRASPEC (see Appen.B), and the lines were found in good agreement with listed wavelengths (Kelly & Palumbo 1973). Most of the features around 154 Å are actually second order lines. The precise correspondence between the first and second order spectra give added confidence in the identification of the transition.

4-3-b. Fluorine (Z=9).

When the focal spot of the laser is extended from a point to a line, the intensity on target with currently available systems is such that only lower-Z materials are suitable for a population inversion

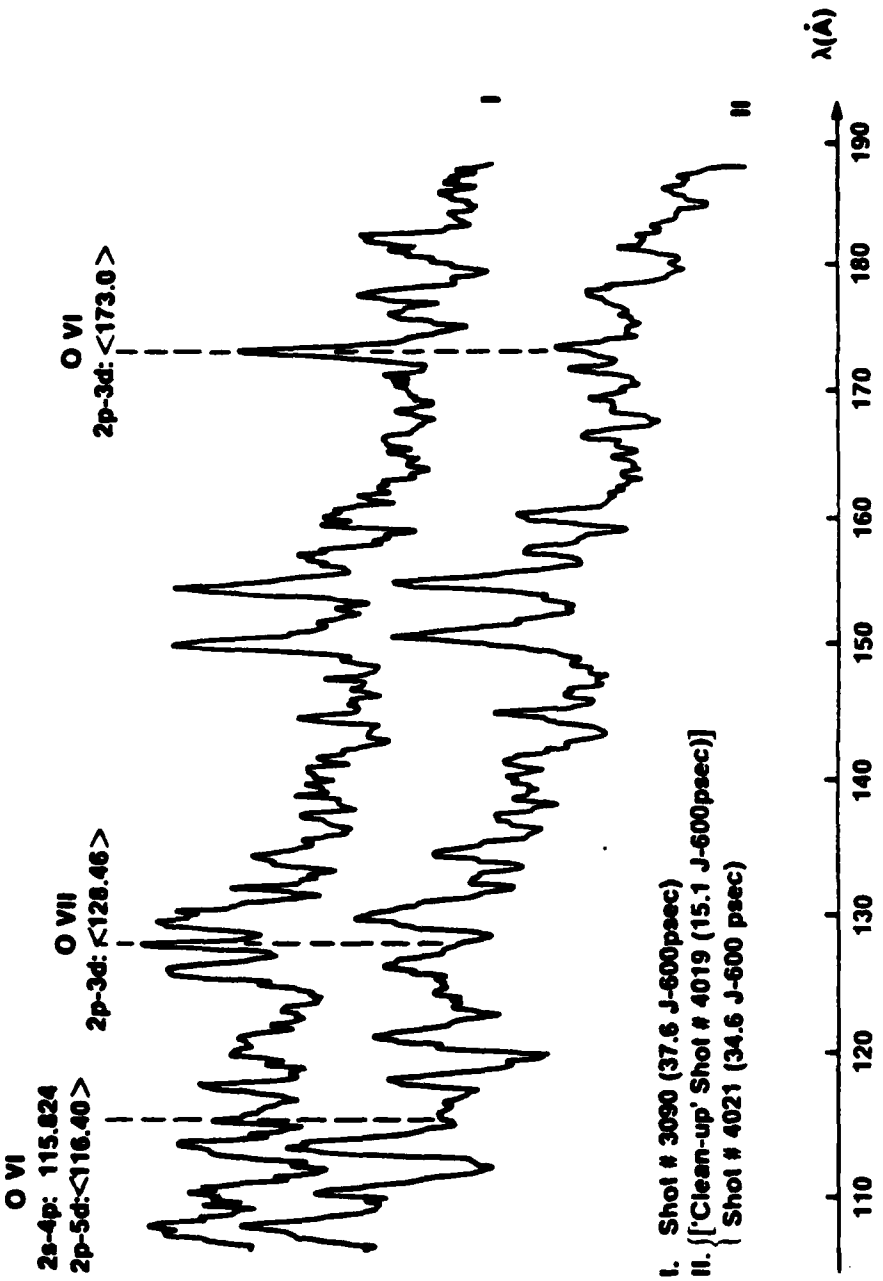

FIGURE 4-13 : REMOVAL OF THE OXYDIZED SURFACE LAYER OF AN ALUMINUM TARGET.

RECORDING OF 3d - 4f TRANSITION (154.4Å) IN HELIUM-LIKE MAGNESIUM

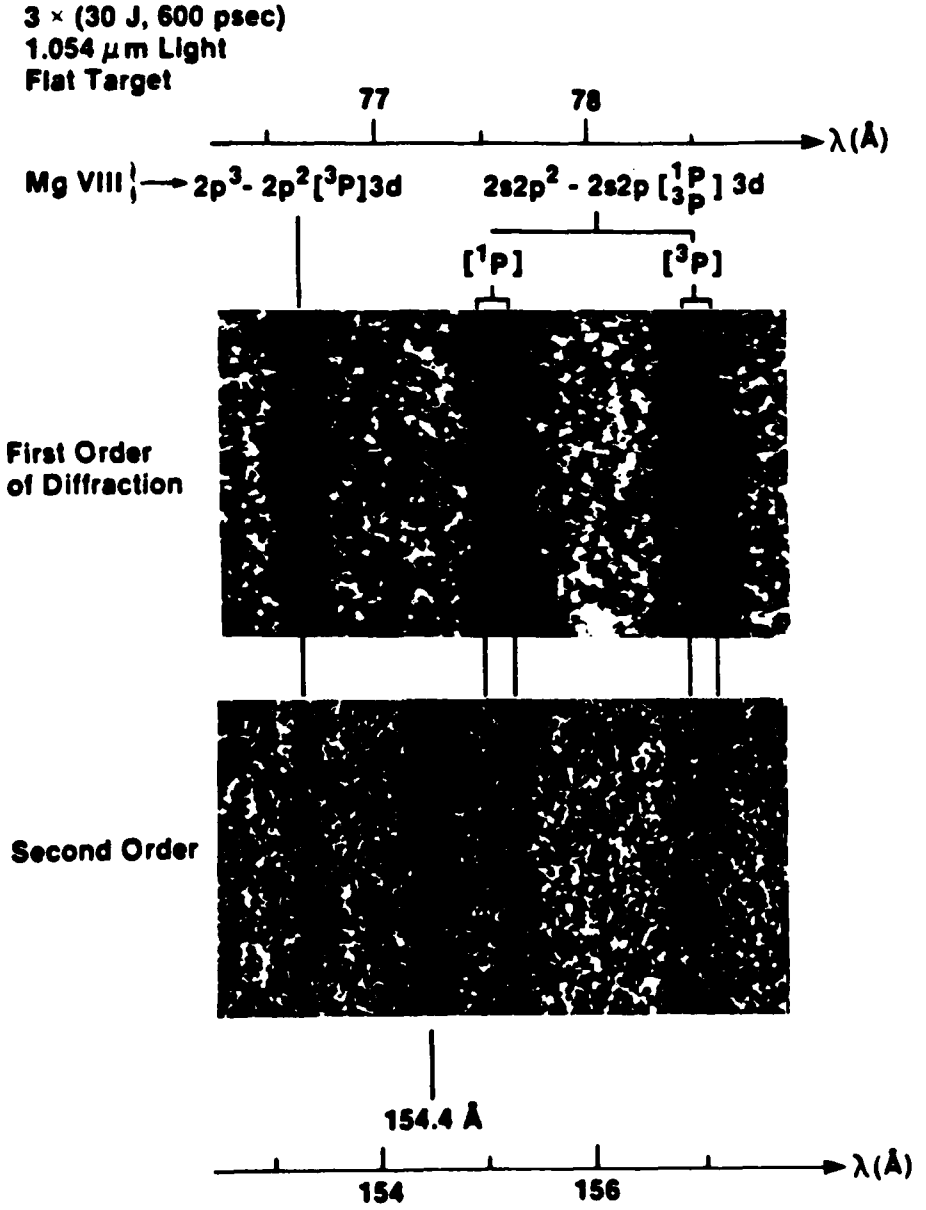

FIGURE 4-14

study. Figure 4-15-a shows the fluorine spectrum recorded when the UV laser (shot #4471*, 15 J, 500 psec) is focused on a 100 μm x 2 mm area of teflon ($(CF_2)_n$). Two titanium foils, 100 μm thick and forming a 200 μm wide slit, were placed 200 μm in front of the target. For comparison, Fig.4-15-b shows the spectrum recorded when the foils are removed (shot #4475*, 20 J, 500 psec).

In shot #4471*, the plasma expansion is very directional, planar instead of diverging. As is apparent on the film and densitometer traces, the transition Lyman β (1s-3p) is much more intense than Lyman α (1s-2p) almost everywhere, on a time-integrated basis. There are several caveats: (i) the heat sink partially blocks the line of sight of the spectrograph for the radiation emitted near the target, for λ>14 Å, (ii) the entrance window of the spectrograph (0.75 μm aluminum) transmits about 15% more at 12.64 Å (L_β) than at 14.98 Å (L_α), (iii) the film, RAR-2491, is more sensitive at the shorter wavelength (Benjamin et al 1977). However, even after taking those factors into account, there exists a strong intensity inversion between the two F^{+8} lines through most of the expansion, showing the possibility of gain at 80.91 Å. There is also some evidence of an inversion between L_γ (1s-4p) and L_β late in the expansion (≳1 mm from the target surface). Gain would be at 231.3 Å on 3d-4f and at 59.95 Å on 2p-4d.

An attempt was made to record these transitions <u>directly</u> with a grating spectrograph. Only a direct observation will lead eventually to

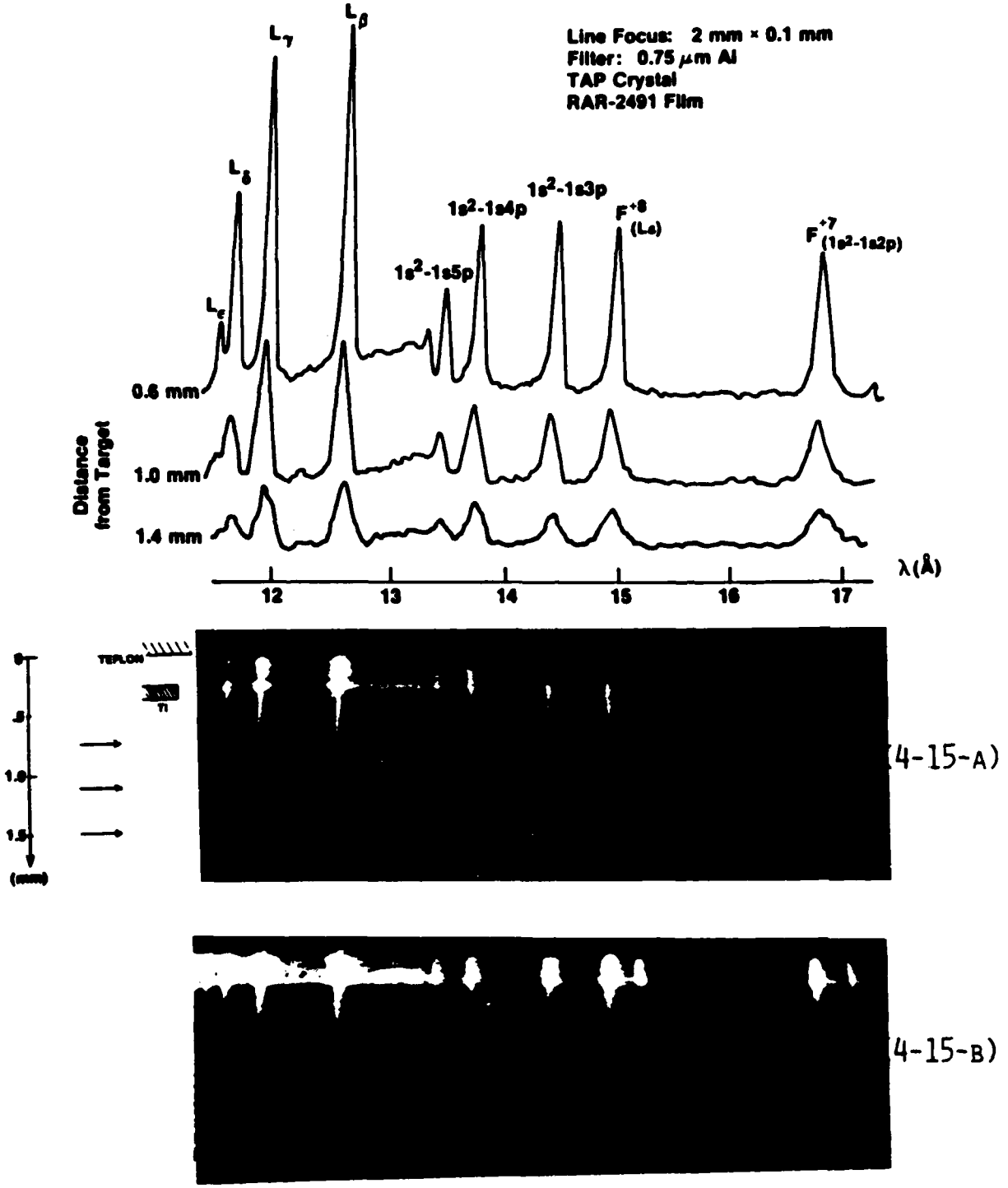

FIGURE 4-15 : LINE-FOCUS. TEFLON TARGET.

a) Shot #4471* (15 J, 500 psec, UV), Titanium foil added,

b) Shot #4475* (20 J, 500 psec, UV), flat target.

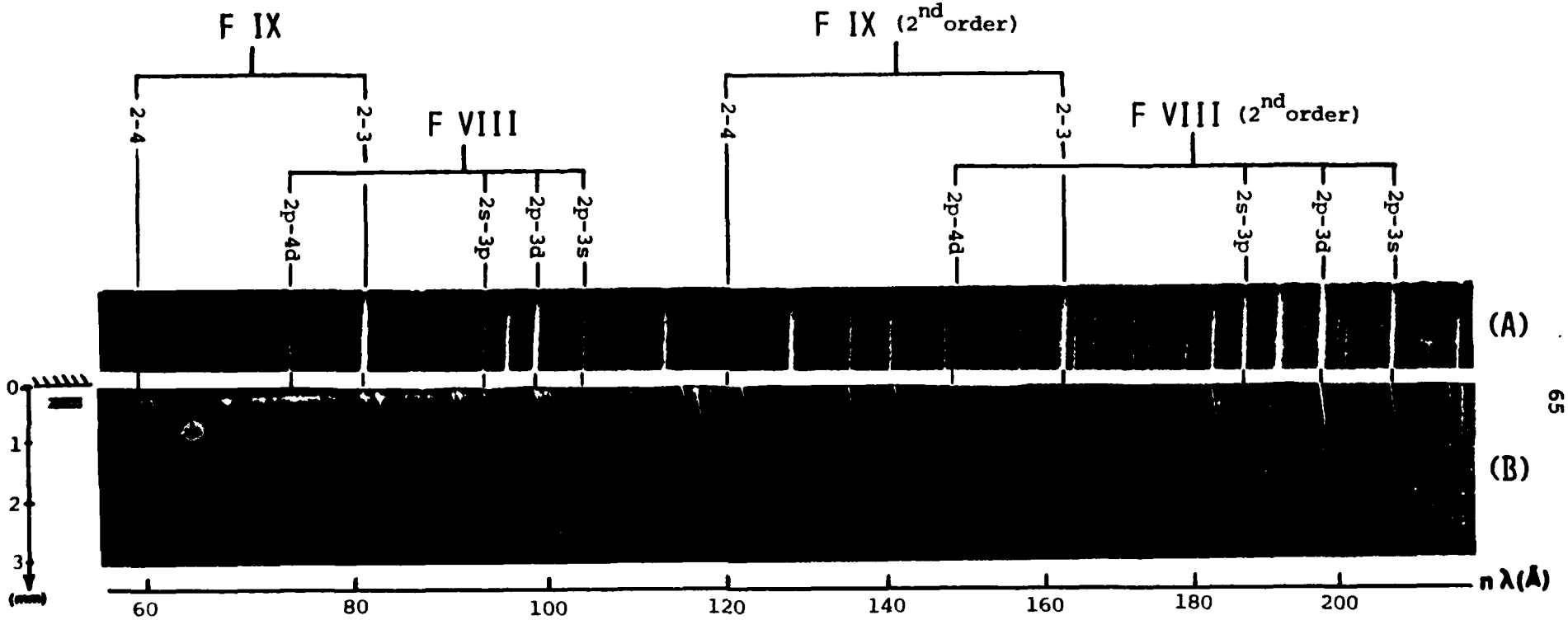

FIGURE 4-16 : FLUORINE SPECTRUM (60-220 Å).

a) Shot #2906* (10 J, 600 psec, UV, point-focus), flat teflon target, spatially integrated spectrum,

b) Shot #4518* (30 J, 1 nsec, UV, line-focus), titanium foil added, spatially resolved spectrum.

a conclusive demonstration of XUV amplification. If amplification occurs, the radiation emerging from the ends of the elongated plasma should be more intense than that emitted in other azimuths, because the photons travel a longer distance through the medium. Therefore, the angular distribution of the amplified spontaneous emission (ASE) should be peaked along or near the end direction (Slaymaker 1978). A meaningful diagnostic requires good discrimination between the angularly dependent signal and other types of radiation. The transition of interest must be recorded (i) on a single-shot basis, to avoid problems of reproducibility in illumination conditions and target design, (ii) with spatial resolution along the plasma expansion, to isolate the "gain region", (iii) free of overlap with other spectral components or strong continuum. Time resolution may also be required, due to the transient nature of the gain (see Chap.5). Figure 4-16 shows the spectrum recorded on shot #4518* (30 J, 1 nsec, same target and focusing conditions as shot #4471*), with an 80 μm spatially resolving slit. A reference spectrum (shot #2906*, 10 J, 600 psec, point focus ϕ 100 μm), taken without spatial resolution, is also presented. The spectral resolution in both cases is $\Delta\lambda \simeq 0.2$ Å. Hydrogenic (F IX) and Helium-like (F XIII) emissions are recorded up to distances $\gtrsim 1$ mm and $\gtrsim 2$ mm from the target surface, respectively. Transitions from lower ionic species are still observed at the edge of the instrumental field of view, 3 mm from the target surface. The Balmer α line (F IX, 2-3) is well isolated from other features and stong enough to be a suitable candidate for an actual study of the ASE. The value of the gain x length product is somewhat uncertain due to the limitations of our

model, as will be seen in the next chapter (Sec.5-3-c). Indications are that it is still below 1, even on an instantaneous basis, and that an angular measurement of the ASE would not be conclusive. Slaymaker (ibid.) calculates that, depending on the radiation environment, i.e. the noise level, a gain x length product $\gtrsim 5$ is required for detection. It is, however, a very promising direction of research and Fig.4-16 shows that the diagnostic capability is in place, ready to be used when higher gain is achieved.

In this chapter, we have shown that (i) short wavelength lasers couple their energy to the target more efficiently, (ii) targets of atomic number $Z>15$ can be used as sub-nanosecond point sources of monochromatic X-rays, (iii) targets of atomic number $Z<15$ can be used for the design of an X-ray amplifier based on enhanced recombination of an expanding plasma, with good scaling prospects when larger systems are available, (iv) the Balmer α line of fluorine (80.9 Å) is a prime candidate for direct gain measurement in the not-too-distant future.

Chapter 5

Computer Modeling

The experiments described in Chapter 4 were modeled with the 1-dimensional laser fusion code LILAC (Goldman 1973, Delettrez 1978-82). The code computed the hydrodynamic motion of the plasma while providing temperature and density of both ions and electrons at each time step and for each numerical cell. These parameters served as input for our subroutines modeling the atomic rate equations, radiation transport and plasma cooling relevant to the present study. This chapter gives some details about the program (file name CYLINE) containing the subroutines. A dummy calling program (YRATE) was written to run simulations for predetermined expansion characteristics ($N_e \sim T_e^{\times}$) and cooling times. Full-scale, time-dependent simulations with LILAC (in place of YRATE) are compared with the experimental data.

5-1. Program CYLINE.

CYLINE is based on the calculations by McWhirter & Hearn (1963) for the recombination of a fully-ionized plasma into an hydrogenic plasma, as reviewed in Chapter 2. We describe here some of the specific features of our program.

5-1-a. Rate equations.

The treatment of McWhirter & Hearn (ibid.) was also used for the Helium-like ions with (i) an apparent nuclear charge Z-1 instead of Z for the reduced electron temperature and density, (ii) the assumption of

a uniform population density among states of same principal quantum number, (iii) a proper count of the degeneracy factor for each energy level. Outside the range of validity of the calculations ($0.35\ Z^2 < T_e(eV) < 22\ (Z-1)^2$, no practical boundaries for N_e), the populations of the excited states were not computed. It is not a serious limitation because (a) in the upper range of temperature the plasma contains mainly bare nuclei, (b) in the lower range most hydrogenic and helium-like ions are in their ground state. For lower stages of ionization, we used a formula quoted by Stratton (1965), which applies to a plasma in coronal equilibrium:

$$\log(N_{i+1}/N_i) \simeq 8.15 + \log T_e - 3 \log \chi_i - \chi_i/2.3\, T_e + \log(\xi_o/n_o) \quad (5\text{-}1)$$

"where N_i and N_{i+1} are the relative numbers of ions of states of ionization i and i+1, (...) χ_i is the energy [in eV] required to ionize the ith ionization state, (...) n_o is the total quantum number of the ground state of the ith ionized atom, (...) ξ_{n_o} is the number of electrons in the n_oth shell, (...) and T_e is the electron temperature [in eV]" (ibid.). Coronal equilibrium, i.e. the regime of collisional excitation balanced by radiative recombination, applies when (ibid.)

$$N_e < 3\ 10^{13}\ \chi_i^3\ (k\, T_e)^{1/2} \quad (5\text{-}2)$$

Since the rapid laser heating produces a high-energy plasma, L-shell recombinations become significant only after the plasma has expanded and cooled. Condition 5-2 then holds true and justifies the use of Eq.5-1.

It is important to adapt the rate equations to the constantly changing temperature and density of the plasma. The rates of three-body

and radiative recombination and ionization (Elton 1970) were used to determine the plasma equilibrium time, τ_{eq}. τ_{eq} was set equal to the fastest of these rates and was compared to the time step, τ_h, of the hydrodynamic calculation. If $\tau_h < \tau_{eq}$, the populations $(N_i)_j$ calculated at step j do not change rapidly enough to reach their new equilibrium value $[(N_i)_{j+1}]_{eq}$ at step j+1. The actual populations $(N_i)_{j+1}$ were computed as follows:

$$(N_i)_{j+1} = (N_i)_j + \{[(N_i)_{j+1}]_{eq} - (N_i)_j\}[1 - \exp(-\tau_h/\tau_{eq})] \qquad (5\text{-}3)$$

Whenever necessary, the population distribution was renormalized to the total number of ions in each numerical cell.

5-1-b. Radiation transport.

CYLINE calculates the number of photons received by a detector placed at 90° from the laser axis (see Figure 5-1). The "detector", which simulates a crystal spectrograph, provides a 10 μm spatial resolution along the direction of expansion (that resolution could be changed easily if necessary). In a dense plasma, strong reabsorption of line radiation may occur. It affects not only absolute photon counts but also line ratios because it is proportional to the absorption oscillator strength (f) of the transition. Let us assume a uniform plasma of length l and absorption coefficient κ_ν (see Fig.5-1-b). The intensity measured at one end of the plasma is (Elton 1970)

$$I_\nu = (\varepsilon_\nu/\kappa_\nu)\ [1 - \exp(-\kappa_\nu l)] \qquad (5\text{-}4)$$

where ε_ν is the emission flux density (in the absence of absorption

EQUIVALENT TARGET IRRADIATION GEOMETRY USED IN ONE-DIMENSIONAL *(LILAC)* SIMULATION

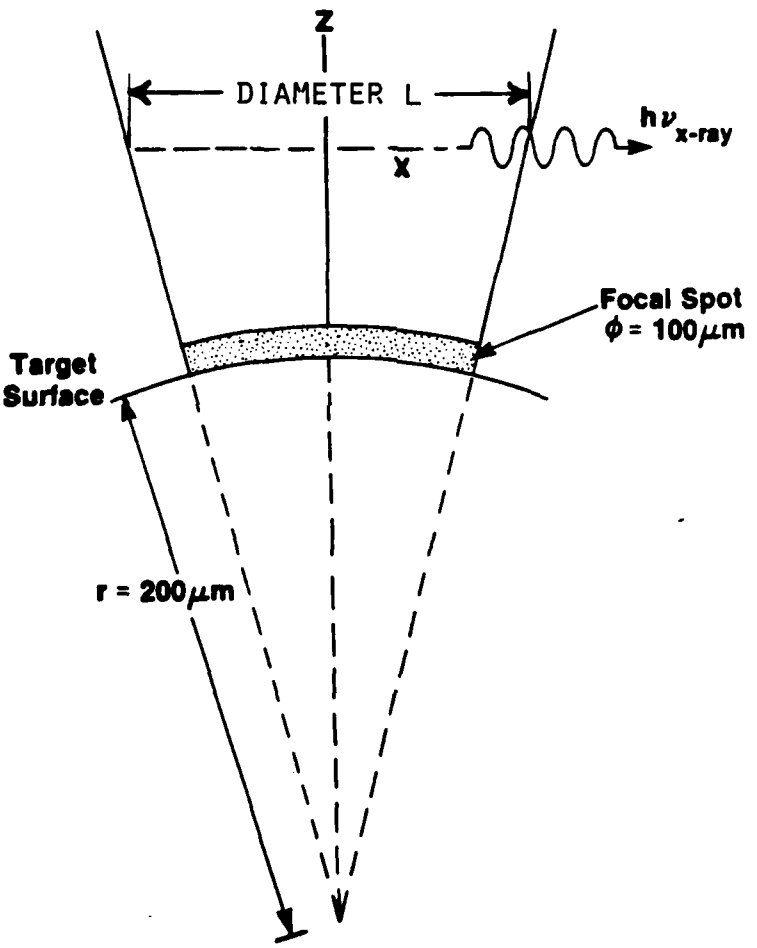

FIGURE 5-1

(κ_ν=0), I = ε_νl). Hence the transmission factor for the radiation at frequency ν is

$$\mathcal{t}_\nu = [1 - \exp(-\kappa_\nu l)]/\kappa_\nu l = [1 - \exp(-\tau_\nu)]/\tau_\nu \qquad (5\text{-}5\text{-}a)$$

where we define the optical depth, $\tau_\nu = \kappa_\nu l$. Eq.5-5-a has to be integrated over the normalized spectral profile S_ν of the transition ($\int_{-\infty}^{\infty} d\nu\, S_\nu = N$, density of absorbing ions per cm^3):

$$\mathcal{t}_\nu = \int_{-\infty}^{\infty} d\nu\, S_\nu \{[(1 - \exp(-\tau_\nu)]/\tau_\nu\} \;/\; \int_{-\infty}^{\infty} d\nu\, S_\nu \qquad (5\text{-}5\text{-}b)$$

Since τ_ν is proportional to S_ν,

$$\mathcal{t}_\nu = \int_{-\infty}^{\infty} d\nu\, [1 - \exp(-\tau_\nu)] \;/\; \int_{-\infty}^{\infty} d\nu\, \tau_\nu \qquad (5\text{-}5\text{-}c)$$

Let us consider the two basic cases of Lorentzian and Doppler spectral profiles.

5-1-b-1. Opacity for Lorentzian lines. If ν_o is the frequency at the center of the line (optical depth τ), and $\Delta\nu$ the fwhm, (Svelto 1982)

$$\tau_\nu = \tau(\Delta\nu/2)^2/[(\nu-\nu_o)^2+(\Delta\nu/2)^2] \qquad (5\text{-}6)$$

In the numerator on the right-hand side of Eq.5-5-c, the exponential can be written as a series. The term by term integration leads to (5-7)

$$\int_{-\infty}^{\infty} d\nu\, [1 - \exp(-\tau_\nu)] = \sum_{n=1}^{\infty} (-1)^{n+1} (\tau^n/n!)(\Delta\nu/2)^{2n} \int_{-\infty}^{\infty} d\nu/[(\nu-\nu_o)^2+(\Delta\nu/2)^2]^n$$

From the identity (Gradshteyn & Ryzhik 1980, p.292)

$$\int_{-\infty}^{\infty} dx / (x^2 + a^2)^n = a^{1-2n}\ \Gamma(1/2)\ \Gamma(n-1/2) \;/\; \Gamma(n) \qquad (5\text{-}8)$$

it follows that the right-hand side of Eq.5-7 is equal to

$$\pi(\Delta\nu/2)\ \{\sum_{n=1}^{\infty}(-1)^{n+1}\ (\Gamma(n-\tfrac{1}{2})\ /\ \Gamma(\tfrac{1}{2}))\ \tau^n/(n-1)!\ n!\} \qquad (5\text{-}9)$$

Finally, after dividing by $\int_{-\infty}^{\infty}d\nu\,\tau_\nu = \pi(\Delta\nu/2)\tau$, we get

$$\mathcal{L}_{\text{Lorentz}} = 1 + \sum_{n=1}^{\infty}(\Gamma(n+\tfrac{1}{2})\ /\ \Gamma(\tfrac{1}{2}))\ (-\tau)^n/\ n!\ (n+1)! \qquad (5\text{-}10)$$

The series converges because (i) consecutive terms are of opposite sign, (ii) the ratio of consecutive terms is $(n-0.5)\,\tau/n(n+1) < 1$ for large values of n ($n > \tau$).

5-1-b-2. Opacity for Doppler lines. In this case (Svelto 1982)

$$\tau_\nu = \tau\ \exp-[A(\nu-\nu_o)]^2 \qquad (5\text{-}11)$$

where A is a constant which need not be specified, as will be apparent in the final result. The same series expansion of the exponential in Eq.5-5-c leads to

$$\int_{-\infty}^{\infty}d\nu\ [1-\exp(-\tau_\nu)] = \{\sum_{n=1}^{\infty}(-1)^{n+1}\ \tau^n/n!\sqrt{n}\}\ \int_{-\infty}^{\infty}d\nu\ \exp-[A(\nu-\nu_o)]^2 \qquad (5\text{-}12)$$

After division by $\int_{-\infty}^{\infty}d\nu\,\tau_\nu$,

$$\mathcal{L}_{\text{Doppler}} = (-1/\tau)\ \sum_{n=1}^{\infty}(-\tau)^n/n!\sqrt{n} = \sum_{n=1}^{\infty}t_n \qquad (5\text{-}13)$$

The series converges for the same reasons as the previous one did.

The program CYLINE assumes Doppler-broadening of the spectral lines. Ion temperatures T_i in the range 0.1-1 keV produce linewidths $(\Delta\nu/\nu)_{\text{Doppler}}$ of order $1.5\text{-}5\times10^{-4}$ in aluminum (see Eq.3-1). Stark

broadening, which would produce a Lorentzian line profile, occurs at densities higher than those of the expanding plasmas studied here (Yaakobi et al 1981-b). Also, since it is proportional to the difference of the squared total quantum numbers of the upper and lower levels, it should be larger for transitions from high-lying states. That effect is not observed on any of the data presented in Chapter 4.

The optical depth at the center of the Doppler line profile is given by (Griem 1964, p.196):

$$\tau = 1.1\ 10^{-16}\ \lambda\ N<l>\ (M/T_i)^{1/2}\ f \qquad (5\text{-}14)$$

where M is the ion mass (amu), T_i the ion temperature (eV), λ the wavelength (Å) and $<l>$ (cm) the average length of the plasma in the direction of observation. Refering to Fig.5-1, (i) in a point-focus geometry, $<l>=(8/3\pi)(\phi/r)z$ where ϕ is the diameter of the focal spot, r the radius of the sherical target used in the simulation, z the radial distance and $8/3\pi$ an averaging factor over the circular cross-section of the expanding plasma, (ii) in a line-focus geometry, $<l>=L_f+0.5(z-r)$ where L_f is the length of the focal spot and 0.5 a factor chosen to simulate an expansion in a cone of half-angle $\alpha\simeq 14^{\circ}$. In order to compute Eq.5-13, we established (with a little code, file name OPACITY) an asymptotic relation for large values of τ, $\ell_{Doppler}\simeq(1.5+0.4\tau)^{-1}$. For $\tau<30$, CYLINE computes

$$\ell = \sum_{n=1}^{n^*} t_n + 1/2\ t_{n^*+1} \qquad (5\text{-}15\text{-}a)$$

where $n^*=3$ Integer(τ) + 10. For $\tau>30$, it computes

$$\ell = \ell_{30}\ 13.5/(1.5+0.4\,\tau) \qquad (5\text{-}15\text{-}b)$$

5-1-c. Plasma cooling.

The effect of the foil in front of the target, which acts as a heat sink, is treated by a simple, spatially dependent energy loss term proportional to $T_e(1-\exp(-t/\tau_c))$ where t is the instantaneous time step of the calling program (LILAC or YRATE), and τ_c is a "characteristic cooling time" used as free parameter. In CYLINE itself, that loss is written in the form of a temperature drop:

$$-\Delta T_e/T_e = 1 - \exp\{-(t/\tau_c)\ \exp-[(2z-z_2-z_1)/(z_2-z_1)]^4\} \qquad (5\text{-}16)$$

where z_1 and z_2 are the radial coordinates of the foil boundaries. The spatial modulation was introduced (i) to avoid step functions which might disrupt the computation, (ii) to model more closely the gradual cooling of the plasma, by heat conductivity, as it approaches the foil.

5-2. Simulations with YRATE.

YRATE is a calling program written to provide CYLINE with the necessary input when one wants to simulate plasmas in steady-state or with simple expansion characteristics. It was convenient as a debugging tool, prior to lengthy runs with LILAC, to make sure that (i) CYLINE gave reasonably physical results for any value of (T_e, N_e) within its range, (ii) some simplifications made to cut the computation time had a negligible effect on the results (taking into account the fact that this is a rather approximate model anyway). For more convenience, the program includes several graphic options.

5-2-a. Steady-state plasma.

Let us give some examples of what the program can do and how it models a steady-state aluminum plasma. We may make the following parameter comparisons:

1. Relative populations of the various ionic stages for a given set of conditions (T_e, N_e). Figure 5-2 shows that, in the range of densities relevant to this study, the plasma is mainly fully-ionized at 1200 eV, hydrogenic at 600 eV, and beryllium-like at 60 eV. It confirms that the boundaries (60 eV<T_e<3 keV) imposed by the availability of rate coefficients were not restrictive for our purpose. At lower temperatures, the program still computes the overall ionic distribution using Eq.5-1, but not the populations of the excited states of 1- and 2-electron ions.

2. Relative intensity of one line versus T_e for a given density N_e. Figure 5-3 shows the intensity of the resonance lines (a) L_α(H-like), (b) w(He-like), for an optically thin plasma. The conclusion is similar to that drawn from Fig.5-2, i.e. there is an optimal temperature, somewhat independent of density, for the line emission from different ionic stages.

3. Ratio of corresponding transitions in 1- and 2-electron ions versus T_e for a given density N_e. Figure 5-4 shows the intensity ratio of the lines L_α(H-like)/w(He-like) between 60 eV and 1 keV for various densities in the case of (a) an optically thin plasma, (b) an optically thick plasma of depth <1>=170 μm. Clearly, that ratio provides a very sensitive measurement of T_e (see Chap.2) unless the plasma density, hence the opacity, is high.

4. Ratio of different lines of the same ion versus T_e for a given

MODELING OF AN ALUMINUM PLASMA

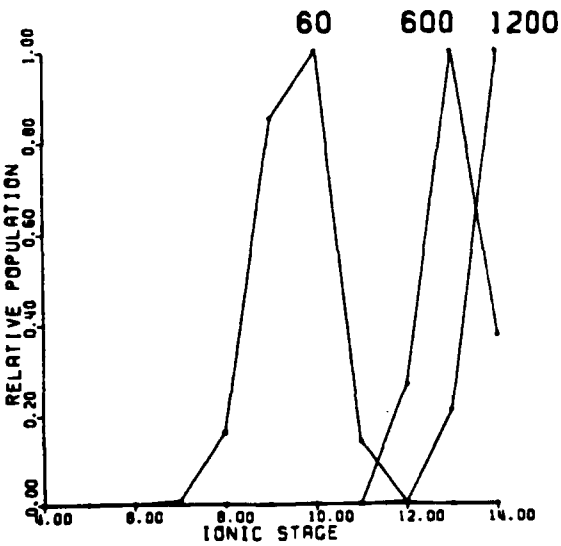

TE (EV) = 1200
600
60

NE (/CM**3) = 10**22.00

AL 1 : NEUTRAL ATOM
AL 14 : FULLY STRIPPED

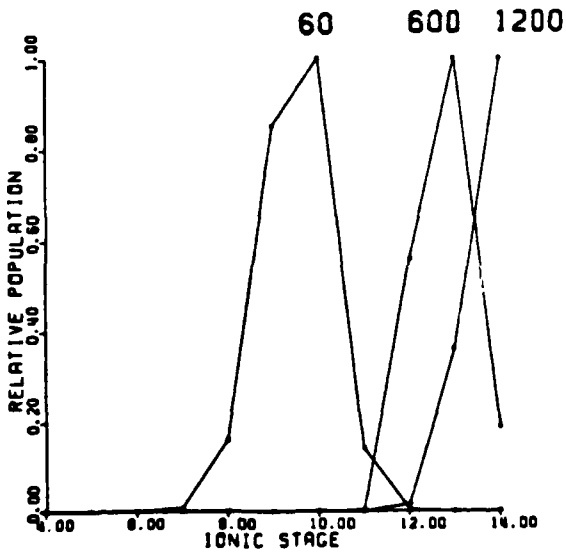

NE (/CM**3) = 10**16.00

FIGURE 5-2 : IONIC DISTRIBUTION.

MODELING OF AN ALUMINUM PLASMA

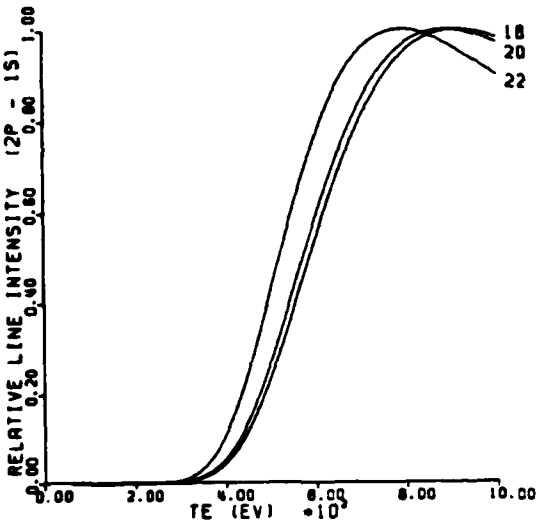

(5-3-A)

NO OPACITY

NE (/CM**3) = 10**22.00
20.00
18.00

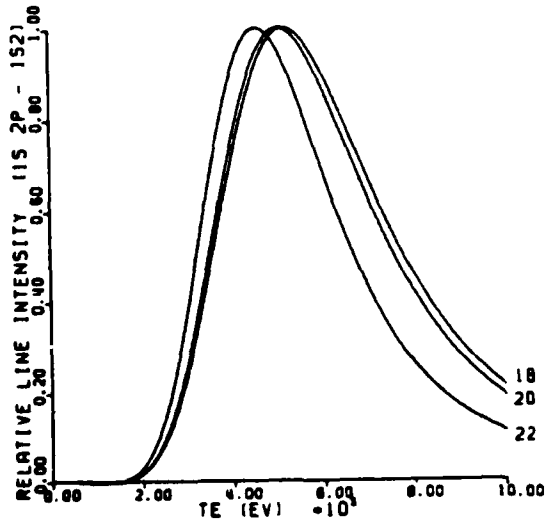

(5-3-B)

FIGURE 5-3 : RELATIVE LINE INTENSITY VERSUS TEMPERATURE.

a) hydrogen-like resonance line,

b) helium-like resonance line.

MODELING OF AN ALUMINUM PLASMA

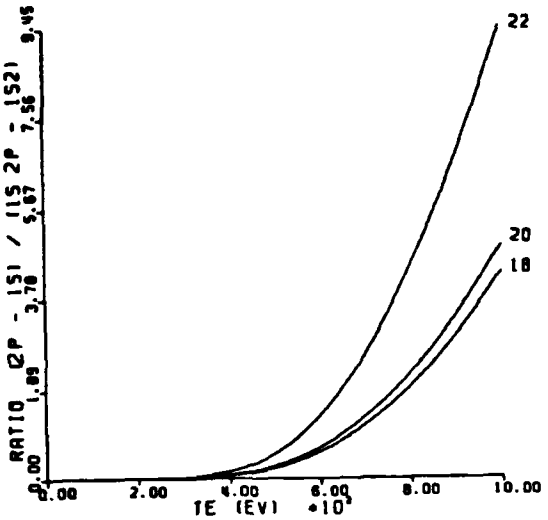

(5-4-A)

NO OPACITY

NE (1/CM**3) = 10**22.00
20.00
18.00

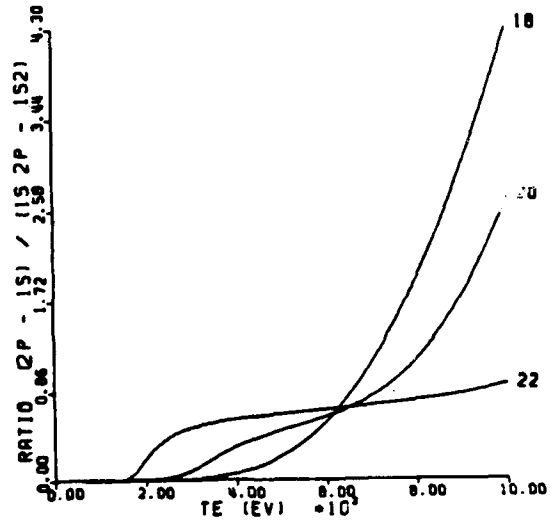

(5-4-B)

DISTANCE: Z-R= 200 MICRON
OPACITY : <L>= 170 MICRON

FIGURE 5-4 : INTENSITY RATIO OF THE HYDROGEN-LIKE TO HELIUM-LIKE RESONANCE LINES

a) optically thin plasma,

b) optically thick plasma.

MODELING OF AN ALUMINUM PLASMA

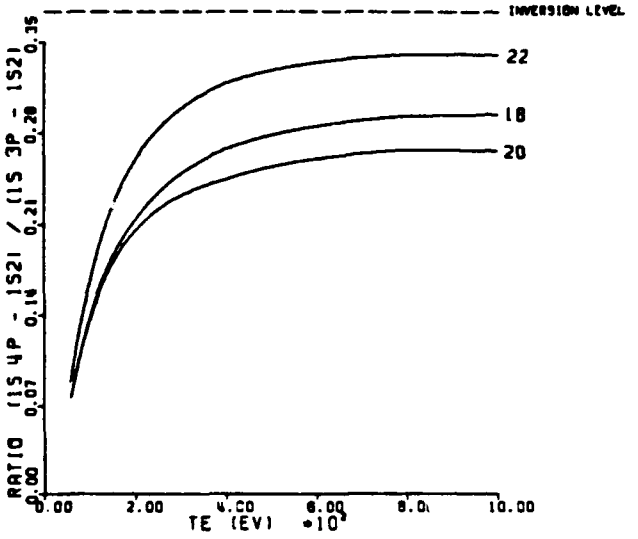

(5-5-A)

NO OPACITY

NE (/CM**3) = 10**22.00
20.00
18.00

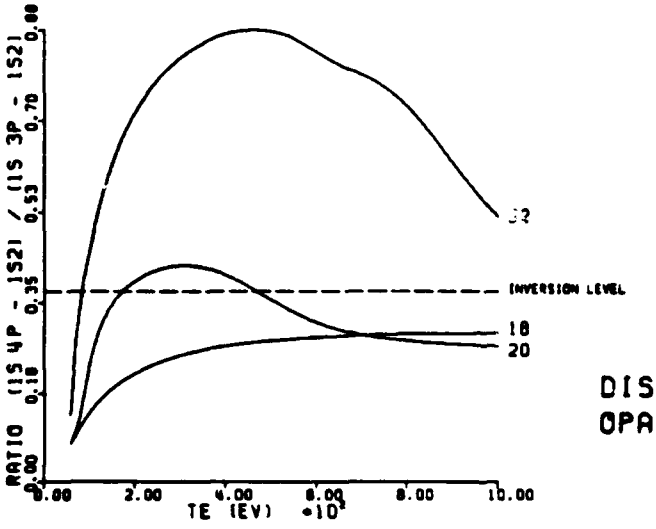

(5-5-B)

DISTANCE: Z-R= 200 MICRON
OPACITY : <L>= 170 MICRON

FIGURE 5-5 : INTENSITY RATIO $1s^2$-1s 4P / $1s^2$-1s 3P.

a) optically thin plasma,

b) optically thick plasma.

The "inversion level" refers to the line ratio required to infer population inversion in the optically thin case.

AD-A136 305 DEVELOPMENT OF X-RAY LASER MEDIA MEASUREMENT OF GAIN AND DEVELOPMENT OF C.. (U) ROCHESTER UNIV N Y LAB FOR LASER ENERGETICS J M FORSYTH FEB 83 2/2

UNCLASSIFIED AFOSR-TR-83-1136-VOL-1 AFOSR-81-0059 F/G 20/5 NL

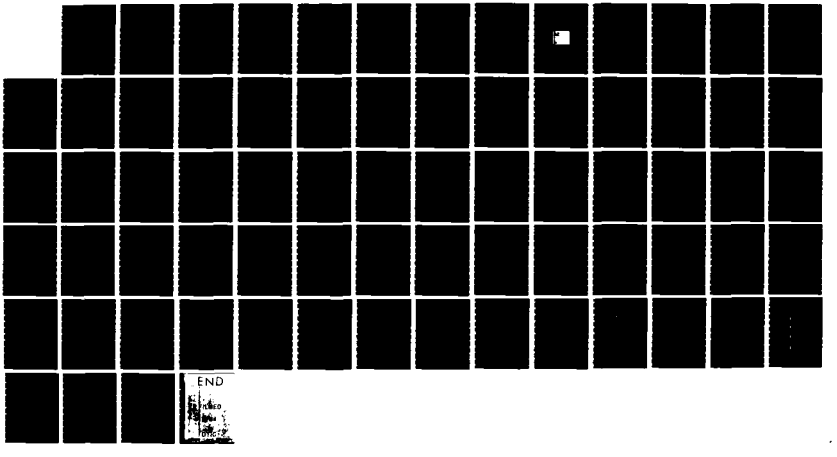

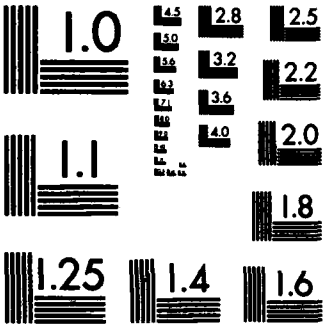

MICROCOPY RESOLUTION TEST CHART
NATIONAL BUREAU OF STANDARDS-1963-A

density N_e. Figure 5-5 shows the intensity ratio of the Helium-like lines $1s^2$-1s4p/$1s^2$-1s3p for (a) an optically thin plasma, (b) an optically thick plasma. The "inversion level" refers to the line ratio required to infer population inversion in the optically thin case. Note that the apparent population ratio is significantly increased by opacity, an important point to keep in mind when interpreting the data. The limit, in a steady-state plasma, is the blackbody spectrum where the emission from the two lines would be of approximately equal intensity.

5-2-b. Expanding plasma.

YRATE can also simulate plasmas with simple expansion characteristics, of the form $N_e \sim T_e^x$, and a cooling rate $R_c = -dT_e/dt$. Depending on the value of R_c, the atomic rate equations may not reach their steady-state solution before the plasma conditions change. This is exactly the situation we are interested in, because a population inversion may occur only if the plasma cooling time is short compared to its recombination time (see Chap.2). The electron density is such that $N_e/(N_e)_o = (z_o/z)^m$ where z is the radial coordinate (see Figure 5-1), $(N_e)_o$ and z_o the initial conditions, and m=1,2,3 for planar, cylindrical or spherical expansion. If the equation of state is such that $N_e \sim T_e^x$, it follows that $T_e/(T_e)_o = (z_o/z)^{m/x}$ and the cooling rate is

$$R_c = -(dT_e/dz)(dz/dt) = (m/x)(T_e/z)_o (z_o/z)^{1+(m/x)} v_{exp} \qquad (5\text{-}17\text{-}a)$$

where v_{exp} is the expansion velocity. If $(R_c)_o$ is the initial cooling rate,

$$R_c = (R_c)_o [N_e/(N_e)_o]^{1/m + 1/x} \qquad (5\text{-}17\text{-}b)$$

As will be seen in the next section, typical numbers in the 1-D simulation of point-focus experiments on aluminum targets ($I \simeq 5\ 10^{14}$ w/cm^2 at λ=0.351 μm) are m=3, z_o=200 μm, $(T_e)_o \simeq 2$ keV, $v_{exp} \simeq 10^8$ cm/sec. For an adiabatic expansion (x=3/2), the cooling rate would be $R_c = 20[N_e/(N_e)_o]$ eV/psec. However, heat conductivity maintains the temperature high in the coronal plasma, and expansion cooling is not effective on very short time scales (Forsyth, et al, 1976). Larger values of x are required to adequately describe the expansion. For x=3, $R_c = 10[N_e/(N_e)_o]^{2/3}$ eV/psec. About 200 μm above the target surface, the density has dropped by an order of magnitude, and the cooling rate is of order 1 eV/psec. The temperature is half its initial value. Taking the plasma at that point (T_e=1 keV, $N_e = 10^{21}$, 10^{20} or 10^{19} cm^{-3}), Figure 5-6 shows the intensity ratio of the helium-like lines $1s^2$-1s4p/$1s^2$-1s3p for an optically thin aluminum plasma, with different cooling rates. If the cooling is only that due to the spherical expansion (5-6-a), population inversion occurs at relatively low temperature, i.e. after a large density drop, especially if the initial density is high. When additional cooling is introduced (5-6-b), inversion occurs at an earlier stage. The limit is reached when the cooling is so fast (5-6-c) that the ionic populations are virtually frozen in their initial distribution.

5-3. Simulations with LILAC.

After having tested the subroutine CYLINE (which contains our computer modeling) with the simple YRATE code, we ran full-scale, time-dependent simulations with the 1-dimensional laser fusion code LILAC (op. cit.). We describe here the interface LILAC-CYLINE, and

MODELING OF AN ALUMINUM PLASMA

NO OPACITY

NE_0 (/CM**3) = 10**21.00
20.00
19.00

NE= C*TE**3.00

SPHERICAL EXPANSION

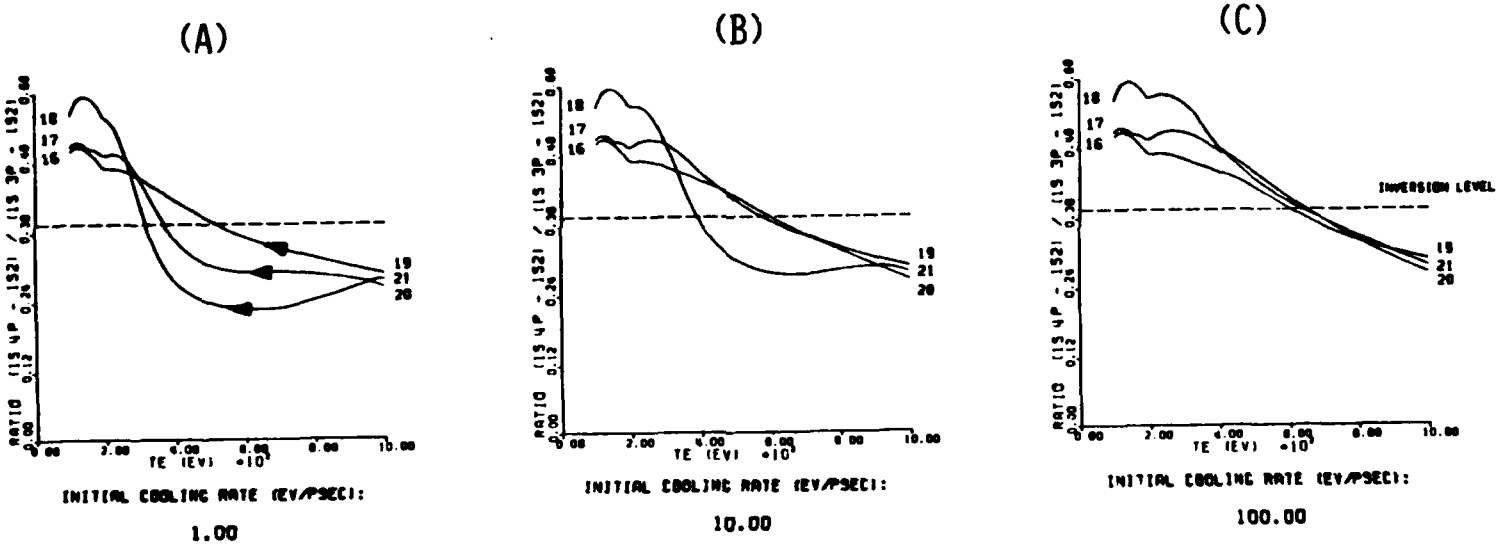

FIGURE 5-6 : INTENSITY RATIO $1s^2$-1s 4P / $1s^2$-1s 3P.

Plasma in spherical expansion, with various cooling rates (see text).
Graphs to be read from right (initial density) to left (final density).

simulations of (i) point-focus experiments on aluminum targets with either IR or UV illumination, (ii) line-focus experiments on fluorine (UV illumination only). Results are compared with the experimental data.

5-3-a. Code LILAC and interface with CYLINE.

LILAC (op. cit.) is a numerical code developed mainly to simulate spherical implosions of DT-filled micro-balloons for inertial confinement fusion (ICF). It computes the hydrodynamic motion of not only the imploding fuel and shell, but the expanding plasma as well. By increasing the wall-thickness of the balloons, it can simulate laser-matter interaction experiments on solid spheres. In the case of point-focus, the target was represented by a sphere of radius 200 μm, twice as large as the laser focal spot (see Fig.5-1), being subjected to the same irradiance as in the experiment but with higher total energy. The calculated X-ray intensity was then scaled to the measured laser pulse energy. This procedure is known to give best results when trying to simulate with a spherically symmetric code the inherently two-dimensional behavior of flat target irradiation (Delettrez 1978-82). The same method was used in the line-focus case, with a simple intensity scaling.

The code uses Lagrangian fluid dynamics. "The local density of the species is found from the instantaneous volume of each cell in [a] spatial grid. (...) The logic of the code (...) requires that all species have the same macroscopic velocity and that all of the ions have the same temperature. Only one momentum equation is then used, but two

energy equations, one for the electrons and one for the ions, are still necessary. Energy exchange mechanisms include flow work, thermal conductivity, coulomb collisions between the electrons and ions, (...) and laser absorption. The thermal conductivities are flux limited with the value of the limiter to be specified by the user" (Goldman 1976). Multigroup suprathermal electron transport (Delettrez & Goldman 1976) and multigroup radiation transport with opacities obtained from Local Thermodynamic Equilibrium tables (Huebner, et al, 1977) are also included.

The code can simulate experiments with (i) IR light (1.054 μm) where coupling of the radiation field to the target is due mainly to resonant absorption, with production of suprathermal electrons, (ii) UV light (0.351 μm), where inverse bremsstrahlung is the dominant absorption mechanism (see Sec.4-1). The temperature drop, ΔT_e, introduced in CYLINE to simulate the heat sink effect of the foil in front of the target (see Sec.5-1-c) translated into a loss term in LILAC's energy equation for the electrons: $\Delta E = n_e C_v \Delta T_e$, where n_e is the number of electrons in a zone, and C_v the heat capacity for electrons. This is equivalent to a radiation loss by the plasma. It was on that basis that LILAC computed a new electron temperature for the next time step.

The simulations were run with a gaussian laser pulse, fwhm=0.5 nsec, peaked at t=0.644 nsec (initial time: t=0). Depending on the laser intensity, hence the plasma expansion velocity, the simulations were stopped after 2 to 4 nsec, enough time for most of the plasma to be at distances ≥1 mm from the target surface, where the density is too low

for relevant experimental observations (at least in our set-up). The output listings, at time intervals 0.2 nsec, included the plasma parameters for each cell of the spatial grid (in particular (T_e,N_e), (T_i,N_i), v_{exp}), and several features specific to the subroutine CYLINE:

1. For each cell, the population densities of bare nuclei, and 1- and 2-electron ions in the ground state and excited states up to n=5 (n, principal quantum number). The average degree of ionization, $<Z>$, was also computed.

2. The cumulative photon count on a "detector" with 10 μm spatial resolution, placed at 90° from the laser axis (see Sec.5-1-b). The count was given for each line of the resonance series n→1 (n=2 to 5) of hydrogenic and helium-like ions. Results were given for (i) an optically thin plasma, (ii) an optically thick, Doppler-broadened plasma (see Sec.5-1-b-2).

3. The optical gain, both instantaneous and time-averaged (from the beginning of the pulse) on the resonance transitions just mentioned, with similar spatial resolution. The gain was computed in the direction perpendicular to that of the laser axis (along the line-focus if applicable).

A graphic routine was written to display and compare the results.

5-3-b. Simulation of point-focus experiments on aluminum.

Figure 5-7 shows the simulation of shot #2789* (see Fig.4-10), when UV light ($I \simeq 5\ 10^{14} W/cm^2$) was focused at the surface of an aluminum slab. A 100 μm foil, placed 200 μm in front of the slab, acted as a heat sink. The main experimental features (increased X-ray emission near the heat

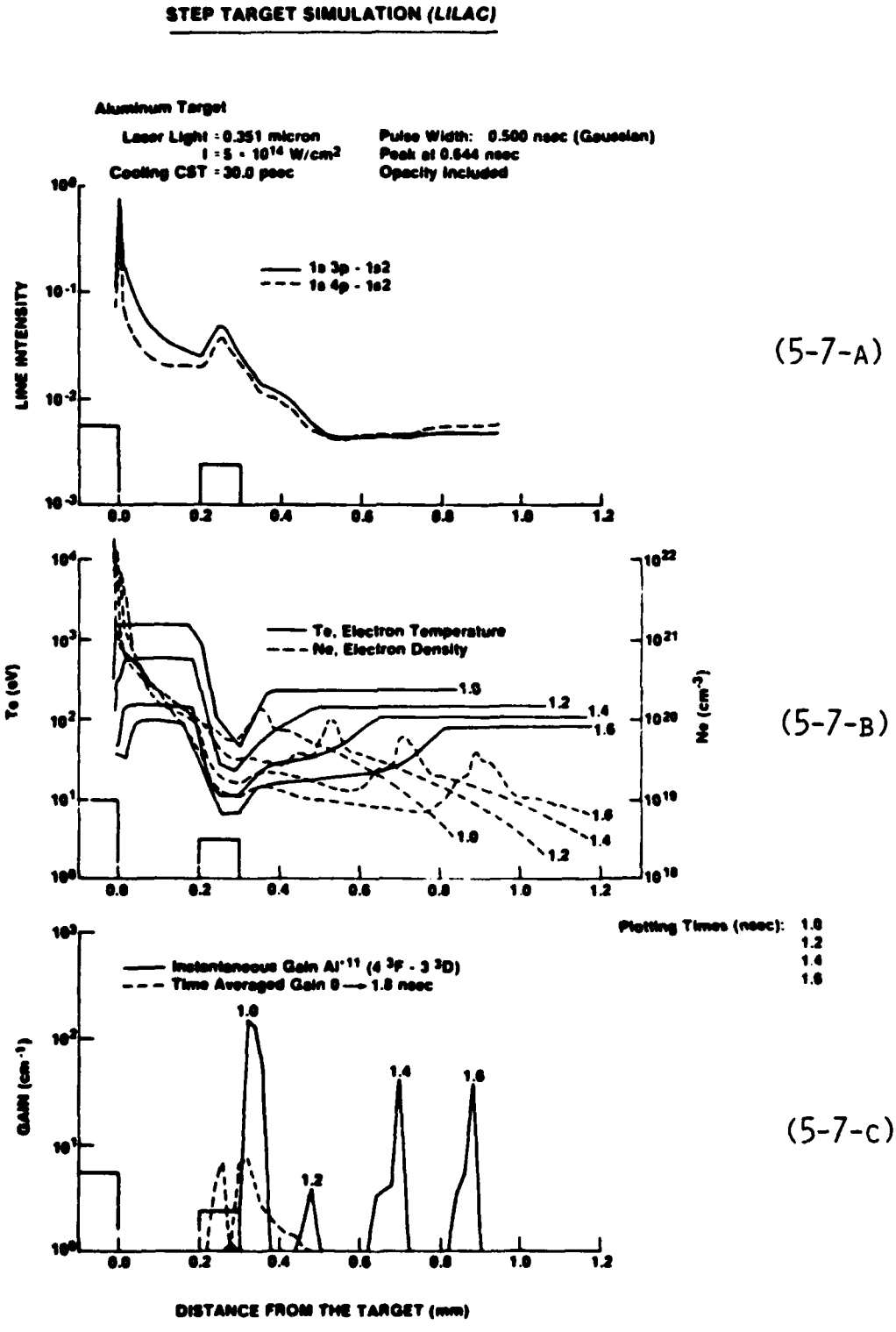

FIGURE 5-7 : SIMULATION OF SHOT #2789* (UV, POINT-FOCUS).

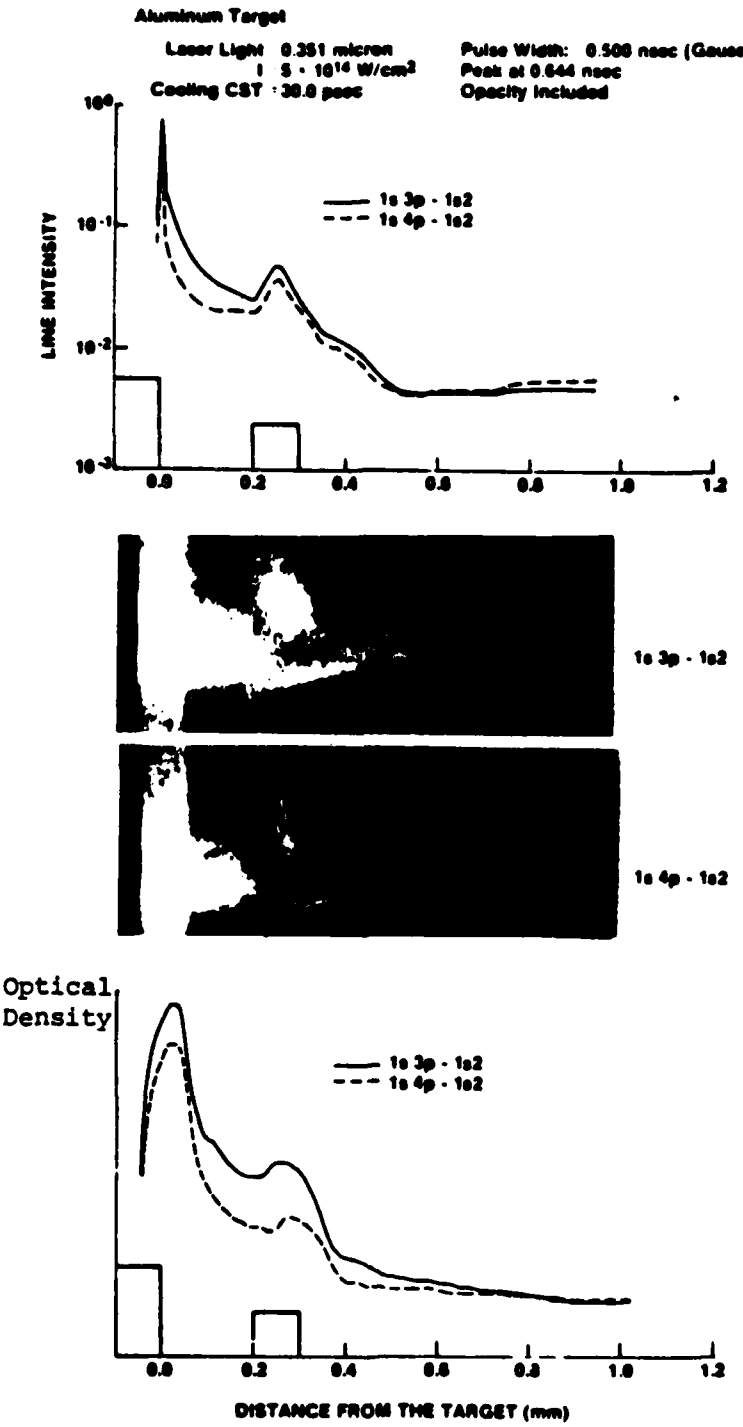

FIGURE 5-8 : COMPARISON OF SIMULATION (A) AND EXPERIMENT (B & C) FOR SHOT #2789*.

sink, anomalous line ratios, see also Figure 5-8), are well reproduced when the "characteristic cooling time" τ_c is set around 30 psec. It corresponds to an enhanced cooling rate R_c^*, in addition to that due to the expanding plasma (see Sec.5-2-b). In the vicinity of the foil, $R_c^* = -dT_e/dt \simeq T_e/\tau_c$. On the side of the foil nearest to the target, T_e is of order 1 keV and $R_c^* \simeq 30$ eV/psec. According to Fig.5-6, it is about the rate required to "freeze" a plasma of density $N_e \gtrsim 10^{20} cm^{-3}$ and to produce a population inversion in the helium-like ion.

As shown in Fig.5-7, the temperature drop near the heat sink produces a pressure gradient. The pressure exerted by the upstream plasma creates a dense region downstream after the foil, appropriate for enhanced recombination. The gain region travels with the velocity of the expanding plasma ($\simeq 10^8$cm/sec for shot #2789*). While the local gain averaged over the plasma recombination time does not exceed 10 cm^{-1}, the instantaneous gain can be much higher ($\sim$100 cm^{-1} over $\lesssim$100 psec). The gain x length product remains small because of the plasma dimensions, a few hundred microns in the transverse direction. Fig.5-8 is a side by side comparison of the simulation (5-8-a, same as 5-7-a) and the experimental data (5-8-b, similar to 4-10 limited to the $1s^2$-1s4p & $1s^2$-1s3p lines, and 5-8-c, densitometer scans).

Let us add a few comments about the simulation. Intensity inversion between the lines $1s^2$-1s4p and $1s^2$-1s3p is not observed

(i) when opacity is not included. Far from the target, the density is low but the size of the plasma is large and self-absorption is still important. It affects $1s^2$-1s3p more than $1s^2$-1s4p, in ratio of the lines' oscillator strengths (0.153 vs. 0.057). Opacity affects most

strongly the dense region near the target surface. If it were not taken into account, the ratio of the two peaks of the emission (i.e. at the target surface and near the heat sink) would be much higher than observed experimentally, by almost an order of magnitude.

(ii) when there is no heat sink, i.e. $\tau_c = \infty$. The line intensities decrease steadily with distance. During the expansion, their ratio remains approximately what it was at distance 100 μm from the target. The consequences of a different location for the heat sink are apparent on Fig.5-6. If the foil is closer to the target and interacts with a denser plasma, a very high cooling rate is required to "freeze" the ionic distribution. If the foil is farther away, intensity inversion may still occur but at low density, hence low gain. Furthermore these geometries are somewhat impractical experimentally (see Sec.4-2).

There is a large margin, factor ∿2-3, for the choice of τ_c. However, if τ_c is too long, the cooling is not efficient enough to produce an inversion. If τ_c is too short, not only may it become unphysical as a heat transfer time constant, but on practical grounds the computation cannot proceed properly: the temperature T_e quickly drops to the level where available rate equations do not apply (see Sec.5-1-a) and the photon count for the transitions of interest has to be temporarily bypassed. In our simulations, we used τ_c as a free parameter to get an approximate match with the experimental data. While the cooling rate R_c^* contains a space and temperature dependence, it would certainly be an improvement if LILAC were to do the calculation itself, taking into account all plasma parameters at each time step. It would have to calculate the behaviour of a hot plasma expanding toward a

cold surface. That may be possible in the near future, due to the current interest in double-shell targets for laser fusion. In our case, the incident laser would "ignore" the outer shell and create a plasma on the surface of the inner shell. The outer shell would then act as a heat sink for the expanding plasma.

LILAC was also run in its IR version (λ=1.054 μm). Figure 5-9 shows the simulation of shot #972 (see Fig.4-5) when IR light ($I \simeq 10^{15} W/cm^2$) was focused at the surface of an aluminum target similar to that used later in shot #2789*. As mentioned in Chap.4, when IR instead of UV light is used, (i) the density of the plasma formed at the surface of the target is one order of magnitude lower (10^{21} vs. $10^{22} cm^{-3}$), (ii) absorption of the light being less efficient, higher incident laser intensities are required to produce a population inversion in the helium-like ion. At comparable levels of absorbed intensity, the smaller number of absorbers leads to a somewhat higher temperature in the IR case (see Fig.5-9-b vs. 5-7-b). The combination of lower density and higher temperature reduces the rate of three-body recombination and makes it more difficult to achieve significant gain.

For this IR simulation, the "characteristic cooling time" τ_c was set at the same value, 30 psec, as previously (UV case). Basic experimental features are reproduced (increased X-ray emission near the heat sink, enhanced line ratios). While population inversion does occur in the expansion, there is no intensity inversion, one main reason being the absence of opacity, due to the lower density. Another consequence of lower density is the smaller pressure gradient produced by the

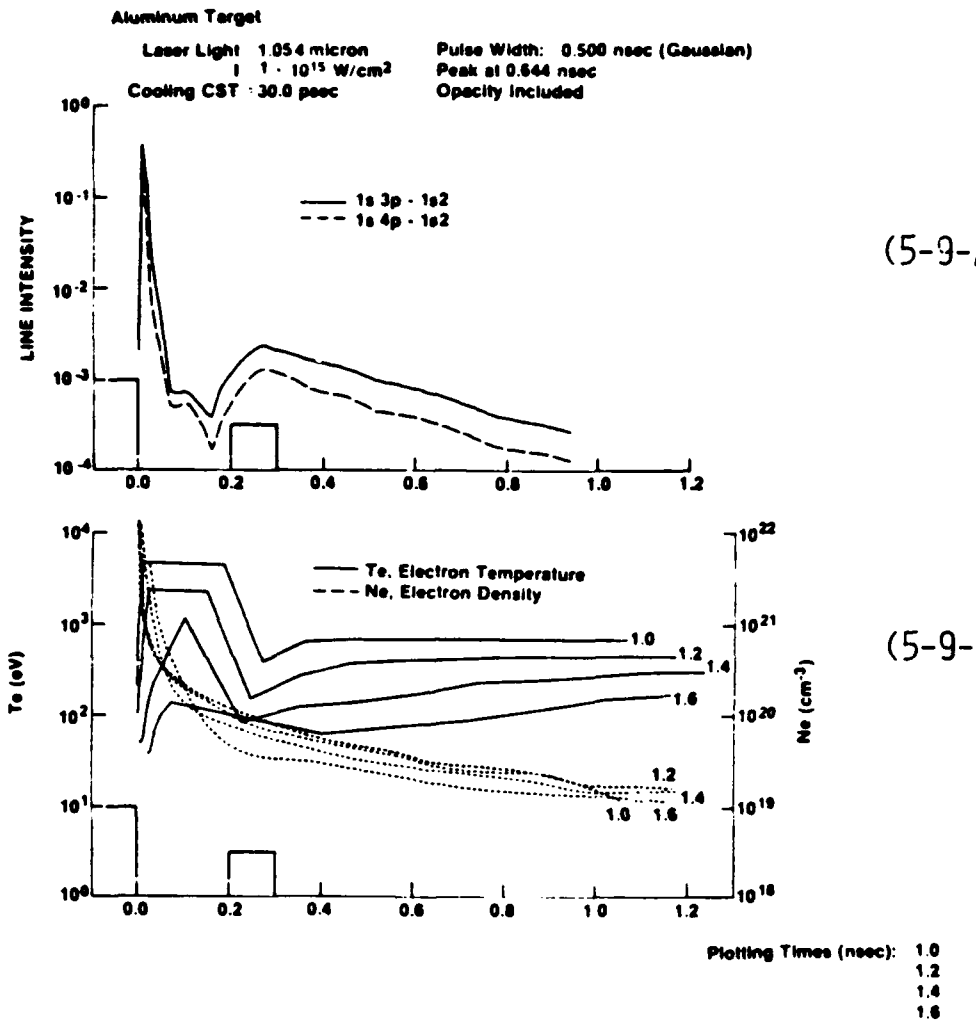

FIGURE 5-9 : SIMULATION OF SHOT #972 (IR, POINT-FOCUS).

temperature drop near the heat sink. The dense region that it creates downstream after the foil (see UV case, Fig.5-7-b) is barely visible in the IR case (Fig.5-9-b).

Finally, we should point out that, in both the UV and IR simulations, the X-ray yield and its distribution among the spectral lines of 1- and 2-electron ions were in general agreement with the experimental data (factor ~ 2 for the absolute yields, and $\lesssim 30\%$ for the line ratios). The fit is reasonable, considering the approximations in the model and the uncertainty in the film calibration.

5-3-c. Simulation of line-focus experiments on teflon.

Some changes were required on LILAC and CYLINE to run simulations of shots on teflon.

(i) Since the table of materials included in LILAC does not contain data for fluorine, we used instead of $(CF_2)_n$ a fictitious CO_2 target at solid density and room temperature (actually 0^oC). The similarity in composition and atomic number (Z=8 for O, 9 for F) should not lead to very different results.

(ii) A separate version of CYLINE (file name CYOXYG) was used, with atomic data for oxygen and the proper scaling laws.

Figure 5-10 shows the simulation of shot #4471* (see Fig.4-15), when UV light ($I \simeq 1.2\ 10^{13} W/cm^2$) was focused on a 100 μm x 2 mm area of teflon (i.e. "CO_2"). A 100 μm foil, placed 200 μm in front of the slab, acted as a heat sink. Fig.5-10-a compares the emission on the hydrogenic transitions L_β (1s-3p) and L_α (1s-2p). The "characteristic cooling time" τ_c was set at 300 psec. There is less cooling in the

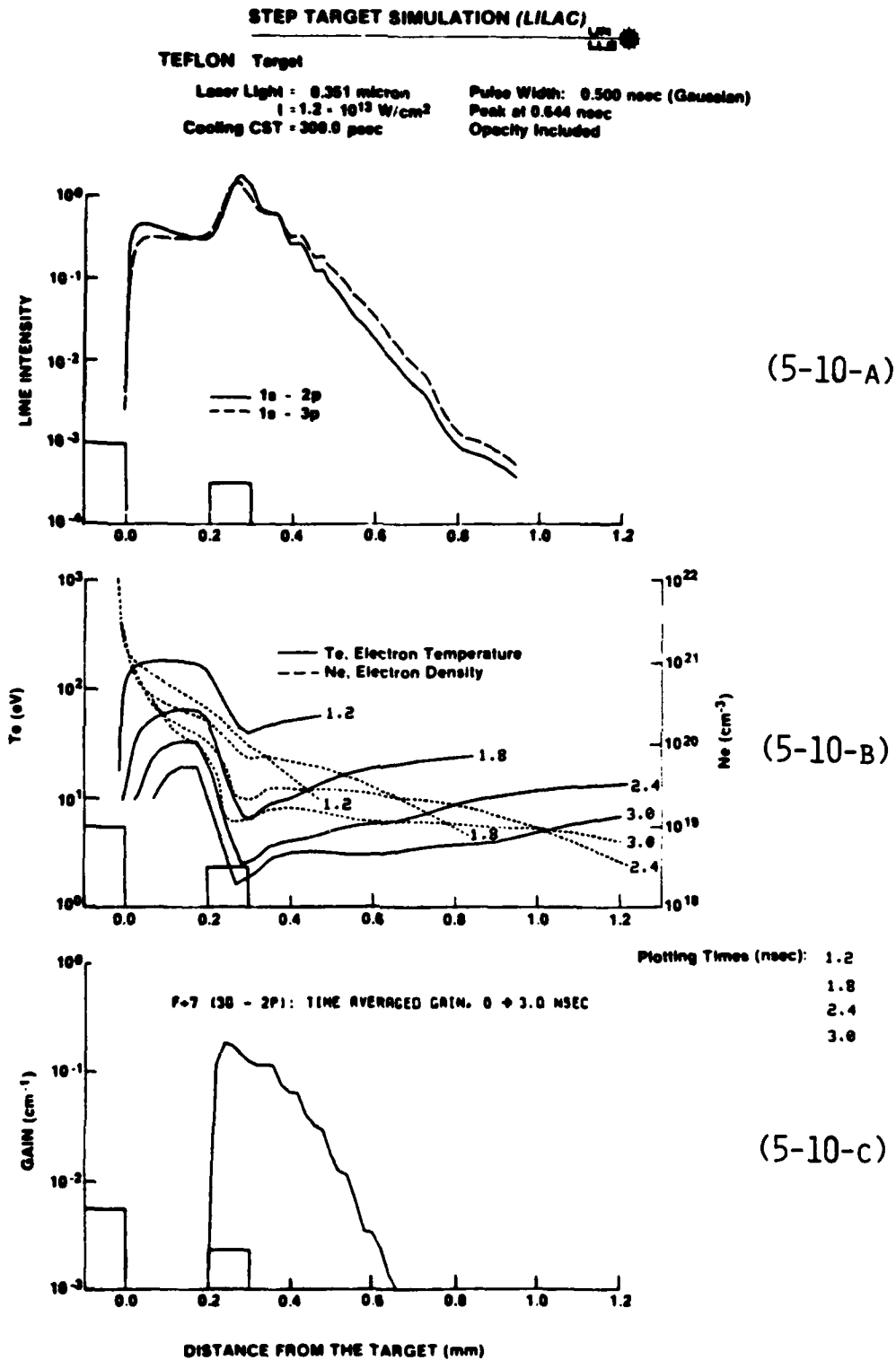

FIGURE 5-10 : SIMULATION OF SHOT #4471* (UV, LINE-FOCUS).

line-focus geometry, compared to point-focus, because the plasma has a smaller volume of nearby vacuum in which to expand. A periodic spatial variation in the pumping radiation should help solve that problem (Silfvast et al 1979-a).

Here again the main experimental features are well reproduced. X-ray emission increases near the foil, and is even stronger than at the target surface (in agreement with the pattern recorded for L_β), due to lower opacity and lower temperature. There is less opacity near the foil because the relative change in plasma length is small compared to the drop in density. The lower temperature is more adequate for bare-nuclei recombination than the hot focal region. The intensity inversion ($L_\alpha < L_\beta$) in the expansion is the combined result of (i) a population inversion, (ii) a difference in opacity (the oscillator strengths for L_α and L_β are in the ratio 0.42 vs. 0.08). The gain region, while moving in time, is more stable than in the simulation of shot #2789* (Fig.5-7: point-focus, aluminum target) because (i) the expansion velocity is lower (3×10^7 vs. 10^8 cm/sec), due to the lower laser intensity, (ii) the population inversion occurs earlier and is less dependent on the propagation of a high density, low temperature plasma.

The line intensities, however, decrease much faster than it appears in the data. This points to the difficulty of describing with a 1-dimensional code a line-focus experiment where the plasma expansion is cylindrical (or possibly planar, see Fig.4-15-a), rather than spherical. Our pseudo-planar geometry using a large sphere (Fig.5-1) can model the plasma overall divergence but not its asymetry and the associated (known

and unknown) hydrodynamic effects. In the vicinity of the foil, the gain averaged over the plasma recombination time is about 0.1 cm^{-1}. Its instantaneous value can reach 5 cm^{-1} over $\sim$ 200 psec for a gain x length product $\sim$ 1.

In this chapter, we have tried to model the experimental observation of intensity inversions in laser-produced plasmas (IR and UV illumination, point-focus and line-focus). Using existing laser fusion code (Delettrez 1978-82) and rate equations (McWhirter & Hearn 1963), we found good agreement with the data when we included (i) enhanced recombination, via cooling, (ii) plasma opacity. The gain region travels with the velocity of the expanding plasma. Its value, high locally in time and space, seems below the requirements for a time-integrated experimental observation.

Summary

This thesis describes the progress made in the development of an XUV amplifier based on the recombination of a laser-produced plasma. Experimental results and numerical simulations have led to a better understanding of the process leading to a population inversion during the plasma expansion. While several important questions require further study, direct demonstration of coherent amplification at $\sim$100 Å seems possible in the forseeable future. We review our results, their limitations, and the prospect for further study.

Population inversions were observed in the helium-like ions Al^{+11} & Mg^{+10} and the hydrogenic ion F^{+8}, by intoducing a foil in the plasma expansion. While the idea in itself is not new (Bhagavatula & Yaakobi 1978), (i) we demonstrated that the inversion was caused neither by resonance mechanisms such as photopumping or charge transfer, nor by channelling of the plasma flow, (ii) we defined, after a parametric study, the optimum target design (a slit-foil of an arbitrary material, 200 μm wide and 200 μm from the original plasma formation), and illumination conditions (short wavelength laser, λ=0.351 μm, of intensity in the range 10^{13}-10^{15} Watts/cm^2 for targets of atomic number 9 to 13). Our experiments used a pump laser focussed on the target in either a point-focus or a line-focus (using specially manufactured cylindrical optics). Inversion was observed in both cases, with appropriate target materials and laser intensities.

Simulations of the experiments were done by combining existing 1-dimensional hydrodynamic code (Delettrez 1978-82) & rate equations (McWhirter & Hearn 1963) with our model, which included (i) enhanced recombination, via cooling of the plasma in the vicinity of the foil, (ii) radiation transport (opacity). The main features of the time-integrated data (overall X-ray flux, increased X-ray emission near the foil, anomalous line ratios) could be reproduced with the proper choice of a "cooling rate". Lowering the temperature of a dense, highly-ionized plasma results in a recombination cascade dominated by collisions, which tend to populate high-lying quantum states of the recombining ion (Gudzenko & Shelepin 1965). The simulations predict that the gain region travels with the velocity of the expanding plasma. The gain could be high locally in time and space, 10^2 cm^{-1} over $\lesssim 100$ psec on $Al^{+11}(3^3D\text{-}4^3F)$ at 129.7 Å and 5 cm^{-1} over $\sim$200 psec on F^{+8}(Balmer α) at 80.9 Å, with point-focus and line-focus illumination respectively. However, the transverse dimensions of the plasma (about 200 μm and 2.5 mm in the region of highest gain) were such that the gain x length product was approximately 1 in both cases. This is 3-5 times less than what is required for a direct gain measurement from recordings of the amplified spontaneous emission (Slaymaker 1978).

Our study was limited in several respects: (i) the data were time-integrated, (ii) the simulations were done with a 1-dimensional code, (iii) a phenomenologic description was used for the interaction of the expanding plasma with the foil. This suggests directions for further research.

Measurements with an X-ray streak-camera (Letzering 1980) would give time-resolved information about the X-ray emission near the foil and the population inversion in the expansion. It would become possible to verify some of the code predictions such as that of a traveling inversion zone. Direct gain measurements are not in order at this point on a time-integrated basis (gain x length products are $\lesssim 0.3$, averaged over the plasma lifetime). With the time resolution, they could become feasible, considering that (i) we used only a fraction of the pump intensity now available at the laboratory (20 J vs. 60 J of UV light in 500 psec), (ii) further upgrade of the pump laser is forthcoming, in both single-beam (GDL) and multi-beam (frequency-tripled OMEGA) configurations, to almost 250 J in 1 nsec, (iii) progress in target design, hence gain, should be expected. With larger lasers, one could not only use a longer line-focus to increase the gain x length product, but also investigate higher-Z targets in order to scale the recombination scheme toward shorter (i.e. X-ray) wavelengths. Preliminary experiments with titanium (Z=22) were encouraging, showing an anomalous line ratio $1s^2$-$1s3p/1s^2$-$1s4p$ in the recombining ion Ti^{+20}.

The modeling could be improved in a variety of ways:

(i) <u>More accurate rate coefficients</u>. Atomic constants are difficult to calculate except for the hydrogenic ion, but updated values supported by experimental data are regularly proposed (see for example Landshoff & Perez 1976).

(ii) <u>Multi-dimensional hydrodynamic code</u>. Since our target design does not have spherical symmetry, 1-dimensional modeling is only

approximate. New codes developed for inertial confinement fusion research, such as the 2-dimensional codes LASNEX (Zimmerman 1973), used by Hagelstein (1981), or SAGE (Craxton 1978-82), would permit a more detailed description of the time- and space-dependent plasma parameters.

(iii) Plasma cooling. Our phenomenologic approach could be replaced by a more rigorous treatment combining plasma physics, thermodynamics, and numerical analysis. It was beyond the scope of this thesis to calculate the behaviour of a hot plasma expanding toward a cold surface, a problem as complex as the absorption of light in laser-matter interaction experiments, still only partially understood despite extensive studies in the laser fusion community (Godwin 1979, Max & Estabrook 1979).

In summary, we present in this thesis strong evidence of population inversion in a laser-produced plasma, due to enhanced recombination via cooling. That conclusion is drawn not from an isolated observation, but from an extended set of experimental data, whose main features are in general agreement with the predictions of an advanced hydrodynamic code.

Gain measurements seem possible in the near future because the two main problems, size of the pump laser and time resolution, can be addressed with present or forthcoming technologies. The projected energy available at 0.351 μm from either GDL or OMEGA (6 beams) being a factor 10 higher than what we used in this work, a 1-2 cm long line-focus should be possible instead of 2 mm. The travel time of a photon in such a medium, 30 psec/cm, is much shorter than the duration of the inversion (200 psec in F^{+8}). Current X-ray streak cameras (op.cit.) are already

faster than required by two orders of magnitude (∿1 psec). The increased X-ray intensity in a scaled-up experiment should compensate for the lower level of exposure in a time-resolving detection system.

Let us sketch an experiment which could demonstrate gain on F^{+8} (Balmer α) at 80.9 Å. A serrated target would be manufactured, made of stripes of teflon separated by deep grooves. Stripes and grooves would each be ∿1 mm wide. 200 Joules of UV light (0.351 μm), delivered in 1 nsec, would be focused on that target over a line (2 cm x 100 μm) transverse to the direction of the stripes. The incident laser, of intensity 10^{13} W/cm^2, would produce ten individual fluorine plasmas (1 mm x 100 μm). Two 100 μm sheets of titanium would be set to form a slit 200 μm wide and 200 μm above the teflon, in a direction parallel to that of the line-focus. Such a design would allow lateral cooling of the plasma, through expansion or contact with a heat sink, while maintaining the line-geometry required for an ASE diagnostic. Two grating spectrographs would record the 80.9 Å radiation emitted along the line-focus and in the transverse direction. The film plane of each spectrograph (Fig.3-5) would be replaced by the entrance slit of an XUV streak camera. The experiment would be repeated with a 90° rotation of both the line-focus and the target in order to cross-reference the two spectrographs. Additional data could be taken at other azimuths. The gain x length product is expected to be large enough (∿5 over 200 psec) to be detected by means of the angular variations of the XUV emission. Such project would require a significant engineering effort, but this thesis has shown that the fundamental obstacles have been overcome and that a direct demonstration of XUV amplification could be achieved soon.

Bibliography.

Bates D.R., Kingston A.E. and McWhirter R.W.P. (1962-a), "Recombination between Electrons and Atomic Ions. I. Optically Thin Plasmas", Proc. Roy. Soc. A 267, 297-312.

Bates D.R., Kingston A.E. and McWhirter R.W.P. (1962-b), "Recombination between Electrons and Atomic Ions. II. Optically Thick Plasmas", Proc. Roy. Soc. A 270, 155-67.

Benjamin R.F., Lyons P.B. and Day R.H. (1977), "X-Ray Calibration of RAR 2490 Film for Application to Laser Plasma Experiments", Appl. Opt. 16-2, 393-7.

Bhagavatula V.A. and Yaakobi B. (1978), "Direct Observation of Population Inversion between Al^{+11} Levels in a Laser-Produced Plasma", Opt. Comm. 24-3, 331-4.

Bhagavatula V.A. (1980), "Soft X-Ray Population Inversion in Laser Plasmas by Resonant Photoexcitation and Photon-Assisted Processes", IEEE Jour. Quant. Elec. 16-6, 603-18.

Brown D.B., Criss J.W. and Birks L.S. (1976), "Sensitivity of X-Ray Films I A Model for Sensitivity in the 1-100 keV Region", Jour. Appl. Phys. 47-8, 3722-31.

Brown D.C., Kelly J.H. and Abate J.A. (1981), "Active-Mirror Amplifiers: Progress and Prospects", IEEE Jour. Quant. Elec. 17-9, 1755-65.

Bunkenberg J., et al (1981), "The OMEGA High-Power Phosphate-Glass System: Design and Performance", IEEE Jour. Quant. Elec. 17-9, 1620-8.

Burton W.M., Hatter A.T. and Ridgeley A. (1973), "Photographic Sensitivity Measurements in the Vacuum Ultraviolet", Appl. Opt. 12-8, 1851-7.

Chapline G. and Wood L. (1974), "X-Ray Lasers", in "X-Ray/Gamma-Ray Laser Project Semiannual Progress Report", Lawrence Livermore Laboratory, UCRL-51823-74.

Conturie Y. and Forsyth J.M. (1980), "Efficient Laser Generation of Intense, Pulsed, Monochromatic Soft X-Rays", J. Opt. Soc. Am. 70-12, 1568.

Conturie Y., et al (1981), "Observation of New Lines of Xe XLIV, XLV, XLVI, and XLVII in the Range 2.5-3.0 A from Laser Imploded Targets", J. Opt. Soc. Am. 71-11, 1309-14.

Craxton S. (1980-82), Private Communication, Laboratory for Laser Energetics, Rochester, N.Y.

Delettrez J. and Goldman E.B. (1976), "Numerical Modeling of Suprathermal Electron Transport in Laser-Produced Plasmas", Laboratory for Laser Energetics, Rochester, NY, Report #36.

Delettrez J. (1978-82), Private Communication, Laboratory for Laser Energetics, Rochester, N.Y.

Dixon R.H. and Elton R.C. (1977), "Resonance Charge Transfer and Population Inversion Following C^{+5} and C^{+6} Interactions with Carbon Atoms in a Laser-Generated Plasma", Phys. Rev. Lett. 38-19, 1072-5.

Dixon R.H., Seely J.F. and Elton R.C. (1978), "Intensity Inversion in the Balmer Spectrum of C^{+5}", Phys. Rev. Lett. 40-2,122-5.

Dozier C.M., et al (1976), "Sensitivity of X-Ray Film II Kodak No-Screen Film in the 1-100 keV Region", Jour. Appl. Phys. 47-8, 3732-9.

Duguay M. (1976), "Soft X-Ray Lasers Pumped by Photoionization", in "Laser-Induced Fusion and X-Ray Laser Studies", PHQEA 3, Addison-Wesley, Reading MA, 557-79.

Egger H., et al (1982), "Generation of Tunable Coherent 79 nm Radiation by Frequency Mixing", Optical Society of America, Topical Meeting on Laser Techniques for Extreme Ultraviolet Spectroscopy, Boulder, CO.

Elton R.C. (1970), "Atomic Processes", in "Methods of Experimental Physics" 9-A, Griem & Lovberg Eds., Academic Press, New York & London, 115-68.

Elton R.C., et al (1979), "Short Wavelength Population Inversions Associated with Charge Transfer in Laser-Produced Plasmas", Fifth Workshop on "Laser Interaction with Matter", Rochester, NY.

Forsyth J.M., et al (1976), "Soft X-Ray Amplification in a Laser-Produced Plasma: a Review and Prognosis", in "Laser-Induced Fusion and X-Ray Laser Studies", PHQEA 3, Addison-Wesley, Reading MA, 581-629.

Frankel R.D. and Forsyth J.M. (1979), "Nanosecond X-Ray Diffraction from Biological Samples with a Laser-Produced Plasma Source", Science 204, 622-4.

Frankel R.D. and Forsyth J.M. (1982), "Application of Nanosecond X-Ray Diffraction Techniques to Bacteriorhodopsin", in "Methods in Enzymology" 88, Academic Press, New York.

Godwin R.P. (1979), "Absorption in Laser-Produced Plasma Experiments: a Personal View", Appl. Opt. 18-21, 3555-61.

Goldman E.B. (1973), "Numerical Modeling of Laser Produced Plasmas: the Dynamics and Neutron Production in Dense Sherically Symmetric Plasmas", Plasma Physics 15, Pergamon Press, Northern Ireland, 289-310.

Goldman E.B. (1976), "Numerical Modeling of Laser Produced Plasmas: Theory and Documentation for SIMSUP", Theory Group Report #6, Laboratory for Laser Energetics.

Gradshteyn I.S. and Ryzhik I.M. (1980), "Table of Integrals, Series and Products", Academic Press, 292.

Griem H.R. (1964), "Plasma Spectroscopy", McGraw-Hill, New York.

Griem H.R. (1975), "Spectral Line Broadening by Plasmas", Academic Press, New York & London.

Gudzenko L.I. and Shelepin L.A. (1965), "Radiation Enhancement in a Recombining Plasma", Sov. Phys. Dokl. 10-2, 147-9.

Hagelstein P.L. (1981), "Physics of Short Wavelength Laser Design", Ph.D. Thesis, MIT (MASS) and Lawrence Livermore Laboratory (CA).

Henke B.L., et al (1967), "X-Ray Absorption in the 2-to-200 A Region", Norelco Reporter, July-December, 112-134.

Henke B.L., et al (1978), "High-Efficiency Low-Energy X-Ray Spectroscopy in the 100-500 eV Region", Jour. Appl. Phys. 49-2, 480-94.

Hora H. (1981), "Physics of Laser Driven Plasmas", John Wiley & Sons, New York.

Huebner W.F., et al (1977), "Astrophysical Opacity Library", Los Alamos Scientific Laboratory, NW, LA-6760-M.

Inglis D.R. and Teller E. (1939), "Ionic Depression of Series Limits in One-Electron Spectra", Astrophys. Jour. 90-3, 439-48.

Irons F.E. and Peacock N.J. (1974), "Experimental Evidence for Population Inversion in C^{+5} in an Expanding Laser-Produced Plasma", J. Phys. B 7, 1109-12.

Jacoby D., et al (1981), "Observation of Gain in a Possible Extreme Ultraviolet Lasing System", Opt. Comm. 37-3, 193-6.

Jaegle P., et al (1971), "Experimental Evidence for the Possible Existence of a Stimulated Emission in the Extreme UV Range", Phys. Lett. 36A-3, 167-8.

Jaegle P., et al (1974), "Superradiant Line in the Soft X-Ray Range", Phys. Rev. Lett. 33-18, 1070-3.

Jaegle P., et al (1981), "X-ray Lasers", in "Lasers" vol. 5, Marcel Dekker Inc., New York.

Kelly R.L. and Palumbo L.J. (1973), "Atomic and Ionic Emission Lines below 2000 Angstroms", NRL Report 7599, Naval Research Laboratory,

Washington, D.C.

Key M.H., et al (1978), "Pulsed X-Ray Shadowgraphy of Dense, Cool, Laser-Imploded Plasma", Phys. Rev. Lett. 41-21, 1467-70.

Koppel L.N. (1974), "Sub-Kilovolt X-Ray Calibration of Photographic Film", Lawrence Livermore Laboratory, UCRL-75891, July 1974.

Lacour B., et al (1976), "Amplification of Soft X-Rays in a Picosecond Laser-Produced Plasma", in "Advances in X-Ray Analysis" 18, Plenum, London, 129-35.

Landshoff R.K. and Perez J.D. (1976), "Determination of Plasma Parameters of Laser-Produced Aluminum Plasma from X-Ray Line Radiation", Phys. Rev. A 13-4, 1619-32.

Letzering S. (1980), "Design and Development of an X-Ray Streak Camera for Laser-Produced Plasma Measurement", Ph.D. Thesis, University of Rochester, New York.

LLL, Lawrence Livermore Laboratory (1974 & 75), "X-Ray / Gamma-Ray Laser Project Semiannual Progress Report", UCRL-51823-74 and -75.

McWhirter R.W.P. and Hearn A.G. (1963), "A Calculation of the Instantaneous Population Densities of the Excited Levels of Hydrogen-like Ions in a Plasma", Proc. Phys. Soc. 82, 641-54.

Norton B.A. and Peacock N.J. (1975), "Population Inversion in Laser-Produced Plasmas by Pumping with Opacity-Broadened Lines", J. Phys. B 8-6, 989-96.

Pert G.J. and Ramsden S.A. (1974), "Population Inversion in Plasmas Produced by Picosecond Laser Pulses", Opt. Comm. 11-3, 270-3.

Reintjes J.F., Dixon R.H. and Elton R.C. (1978), "Extended Plasma Source for Short-Wavelength Amplifiers", Opt. Lett. 3-2, 40-2.

Reintjes J.F., Tankersley L.L. and Christensen R. (1981), "Generation of Coherent Radiation at 61.6 nm by Fifth Harmonic Conversion of Radiation from XeCl Laser", Opt. Comm. 39-5,334-8.

Rosenbluth A. (1982), "Reflecting Properties of X-Ray Multilayer Devices", Ph.D Thesis, University of Rochester, New York.

Salzmann D. and Wendin G. (1978), "Calculation of the Photoabsorption Coefficient in a Hot and Dense Aluminum Plasma", Phys. Rev. A 18-6, 2695-700.

Sawyer R.A. (1963), "Experimental Spectroscopy", Dover Publications Inc , New York, Third Ed.

Scully M.O., Louisell W.H. and McKnight W.B. (1973), "A Soft X-Ray Laser

Utilizing Charge Exchange", Opt. Comm. 9-3, 246-8.

Seely J.F. and McKnight W.B. (1977), "Soft X-Ray Laser Pumped by Charge Exchange between C VII and Ar III in Expanding Laser-Produced Plasma", J. Appl. Phys. 48-9, 3691-6.

Seka W., et al (1980), "High-Power Phosphate-Glass Laser System: Design and Performance Characteristics", Appl. Opt. 19-3, 409-19.

Seka W., et al (1981), "GDL: a High-Power 0.35 m Laser Irradiation Facility", IEEE Jour. Quant. Elec. 17-9, 1689-93.

Seka W., et al (1982), "Measurements and Interpretation of the Absorption of 0.35 m Laser Radiation on Planar Targets", Opt. Comm. 40-6, 437-40.

Silfvast W.T., Szeto L.H. and Wood II O.R. (1979-a), "Ultra-High-Gain Laser-Produced Plasma Laser in Xenon using Periodic Pumping", Appl. Phys. Lett. 34-3, 213-5.

Silfvast W.T., Szeto L.H. and Wood II O.R. (1979-b), "Recombination Lasers in Nd and CO_2 Laser-produced Cadmium plasmas", Opt. Lett. 4-9, 271-3.

Silfvast W.T., Szeto L.H. and Wood II O.R. (1980), "Power Output Enhancement of a Laser-produced Cd Plasma Recombination Laser by Plasma Confinement", Appl. Phys. Lett. 36-7, 500-2.

Slaymaker P.A. (1978), "Angular Distribution of Amplified Spontaneous Emission A Comparison of Theory and Laser-Pumped Dye Amplifier Experiment", Ph.D Thesis, University of Rochester, New York.

Stratton T.F. (1965), "X-Ray Spectroscopy", in "Plasma Diagnostic Techniques", Huddlestone & Leonard Eds., Academic Press, New York London, 359-97.

Svelto O. (1982), "Principles of Lasers", Plenum Press, New York & London, Third Ed.

Weisheit J.C. (1975), "Recombination in Dense Plasmas", J. Phys. B 8-15, 2556-64.

Whitney K.G. and Davis J. (1974), "Hot-spot Model of K-line Emission from Laser-heated plasmas", Jour. Appl. Phys. 45-12, 5294-302.

Whitney K.G., Davis J. and Apruzese J.P. (1980), "Influence of Broadband Photocoupling on K-Shell Excitation in Aluminum", Phys. Rev. A 22-5, 2196-210.

Wiese W.L., Smith M.W. and Glennon B.M. (1966-69), "Atomic Transition Probabilities", Vol.I, "Hydrogen through Neon", NSRDS-NBS-4; Vol.II, "Sodium through Calcium", NSRDS-NBS-22, U.S. Gov. Printing Office,

Washington, D.C.

Woodall D., Yaakobi B. and Lubin M. (1976), "Review of Diagnostics for Laser-Pellet Interaction Experiments", in "Laser-Induced Fusion and X-Ray Laser Studies", PHQEA 3, Addison-Wesley, Reading MA, 191-250.

Yaakobi B., et al (1980), "X-Ray-Absorption Fine-Structure Measurement using a Laser-Compressed Target as a Source", Appl. Phys. Lett. 37-9, 767-9.

Yaakobi B., et al (1981-a), "High X-Ray Conversion Efficiency with Target Irradiation by a Frequency Tripled Nd:Glass Laser", Opt Comm 38-3, 196-200.

Yaakobi B., et al (1981-b), "X-Ray Spectroscopy of Laser Imploded Targets", Phil. Trans. R. Soc. Lond. A-300, 623-30.

Zimmerman G.B. (1973), "Numerical Simulation of the High Density Approach to Laser-Fusion", Lawrence Livermore Laboratory, UCRL-75173.

Appendix A

Photometry and film calibration

Photometry can be an accurate science, but is especially difficult when it involves use of film. Considerable effort was made to define a standard procedure to reduce our data, making it reasonable to compare the results of different experiments. This is important for the crystal spectrograph because the set-up, adapted to the particular goal of each experiment, can affect the film exposure in a number of ways: dimension and position of the source, width of the resolving slit, angle of observation, types of filter, crystal, film, etc... It is also necessary to be consistent in the way the microdensitometry is done. This appendix presents the procedure we used, our film calibration and a comparison with pubished data. A computer program (filename PHOTON) was written to handle that information. At this stage of the X-ray amplifier project, the grating spectrograph was used more to obtain qualitative than quantitative results. We present its imaging characteristics but no film calibration.

A-1. Data reduction procedure.

First one must establish the film exposure geometry. With the coordinates (x,y,z) and (y',z') indicated on Figure 3-4 and $M_z=z'/z$ the transverse magnification between the source and the film, the time dependent population density $n_u(\underline{r},t)$ of the upper level of the recorded transition is related to the time integrated illumination $\bar{E}$ (photons/unit area) on the film as follows:

$$A \int_0^\infty dt \int_{\text{plasma}} d\underline{r}\; n_u(\underline{r},t)\; k(\underline{r},t) \,.\, \text{Rect}[z/\, w(1+1/M_z)] * \delta\,(z-z'/M_z)$$

$$= (4\pi L/\mathcal{R}\mathcal{t}) \int_{\text{spectral line}} dy'\; \bar{E}(y',z') \qquad \text{(A-1)}$$

$\mathcal{R}$ is the integrated reflectivity of the crystal, $\mathcal{t}$ the transmittance of the filter(s), w the width of the slit, L the distance traveled by the X-rays from the source to the film, A the Einstein coefficient for the transition, and k the opacity factor in the direction of observation. Except for w, these quantities are wavelength dependent. Eq.(A-1) assumes that the acceptance angle in the spectral direction is crystal limited. In the two extreme cases, no slit ($w >> \phi_s^*$ apparent source size) and narrow slit ($w << \phi_s^*$), the spatial integration over the plasma reduces to

$$\int d\underline{r}\; n_u(\underline{r},t)\; k(\underline{r},t) \qquad w >> \phi_s^* \qquad \text{(A-1-a)}$$

$$w(1+1/M_z) \int dx\, dy\; n_u(\underline{r},t)\; k(\underline{r},t) \,.\, \delta\,(z-z'/M_z) \qquad w << \phi_s^* \qquad \text{(A-1-b)}$$

When a shadowgram is cast by the outer edge of the slit or by a semi-infinite aperture, one gets

$$\int_{z'/M_z}^\infty dz \int dx\, dy\; n_u(\underline{r},t)\; k(\underline{r},t) \qquad \text{(A-1-c)}$$

The right-hand side of Eq.(A-1) is equivalent to the formula used by Henke et al (1978) to compute the total number N_T of photons emitted by the source into 4π. That formula is valid only if (i) there is no slit, (ii) the emission from the source is isotropic, that is to say

opacity does not depend on the direction of observation. In the most general case one can compute N_T^*, the apparent value of N_T in the direction of observation, by adding up the photons recorded in each resolution element on the film:

$$N_T^* \simeq (4\pi L/\mathcal{R}\ell) \sum_{j=0,\infty} \int_{\text{spectral line}} dy' \, \bar{E}[y', z'=jw(M_z+1)] \qquad (A-2)$$

Figure A-1-a shows how the microdensitometry is done. A Joyce-Loebl model 3C-S has been used. l_t and l_s are the dimensions of the area scanning the film in the spectral direction:

$$l_t l_s = L_t L_s / (2.2\, M_o)^2 \qquad (A-3)$$

L_t and L_s are the dimensions of the adjustable slit in front of the Joyce-Loebl's detection system, M_o is the magnification of the microscope objective collecting the light (O), "2.2" comes from the built-in choice of optical conjugation between film and detector. A typical line has the profile indicated on the graph D versus Y'. We assume that it can be described as follows:

$$D(Y',Z') = D_0 + (D_m - D_0) \exp[-(2\,Y'/\,FWHM)^2 \ln 2] \qquad (A-4)$$

Since the relationship $D(y',z') \leftrightarrow \bar{E}(y',z')$ between density and exposure (number of photons/unit area of film) is non-linear, the most convenient way to proceed is to sample Eq.(A-4) (see Figure A-1-b). As interval of sampling on the film one takes the width of the scanning area (i.e. ml_s on the paper trace) and one stops at $y' \leq fwhm$ where the value of the exponential has dropped to .06:

$$p_0 = \text{Integer}(fwhm/l_s) = \text{Integer}[2.2\,(FWHM/L_s)\,(M_o/m)] \qquad (A-5)$$

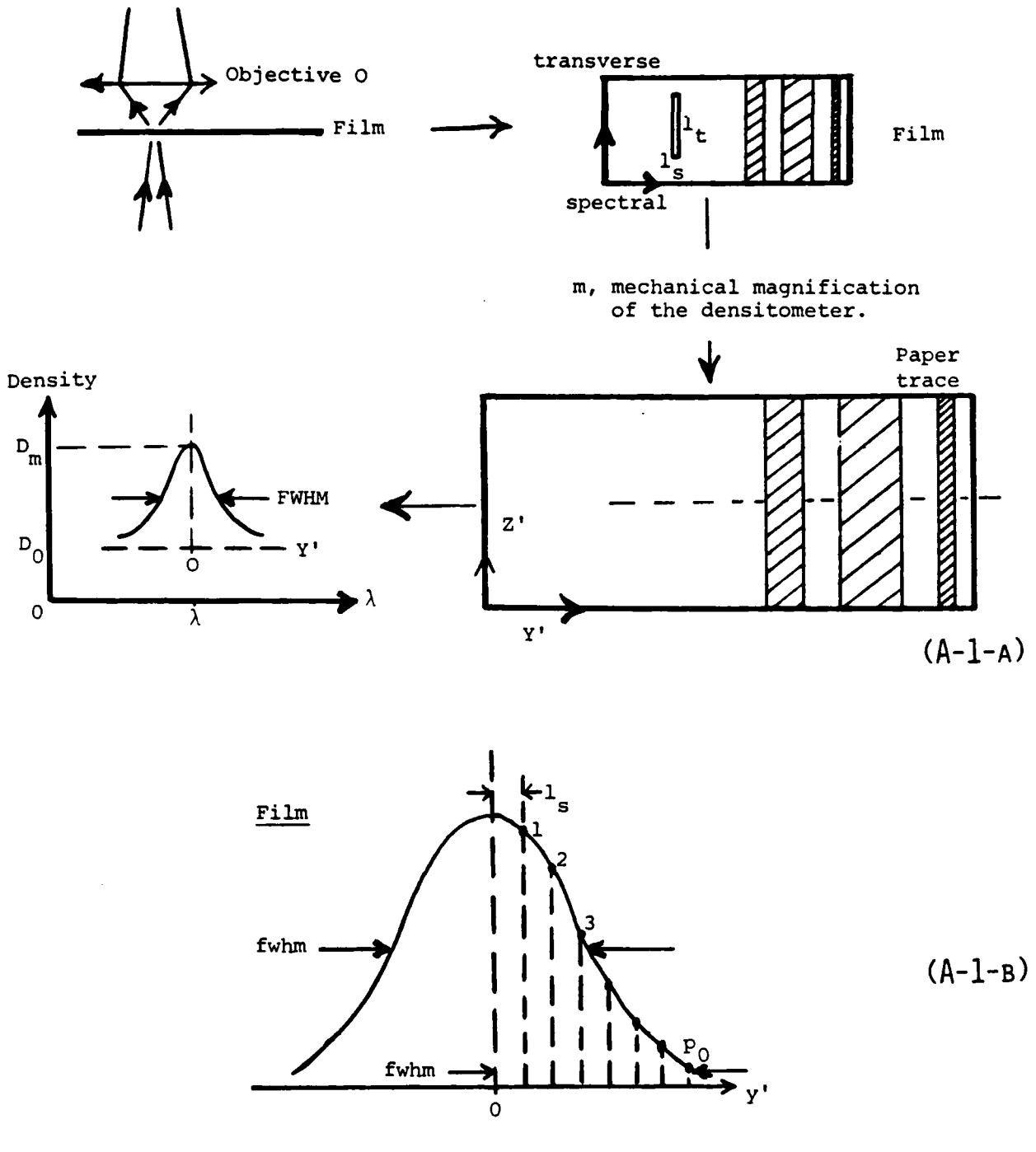

FIGURE A-1 : FILM DENSITOMETRY.

For a reasonable sampling accuracy, L_s must be chosen such that $p_o > 5$. L_t is chosen large enough to reduce the noise from film granularity without affecting the resolution. It follows:

$$\int_{\text{spectral line}} dy' \, \bar{E}(y',z') \simeq l_s \sum_{p=-p_0,p_0} \{\bar{E}(Y'=p\,m\,l_s, Z') - \bar{E}(D=D_0)\} \qquad \text{(A-6)}$$

Let us combine Eq.(A-2) and (A-6):

$$N_T^* \simeq (4\pi L/\mathfrak{A}\mathfrak{t}) \, l_s \sum_{j=0,\infty} \sum_{p=-p_0,p_0} \{\bar{E}(Y'=p\,m\,l_s, Z'=j\,m\,w(M_z+1)) - \bar{E}(D=D_0)\} \qquad \text{(A-7)}$$

With an adequate film calibration, a digitized reading of optical densities on the paper trace leads directly to N_T^*.

A-2. Film calibration.

In the crystal spectrograph we used the films Kodak RAR-2491 (for $\lambda > 4$ Å) and Kodak No-screen ($\lambda < 8$ Å). Before drawing the correspondence between exposure and density for those films at various wavelengths, it is necessary to define what is actually measured with the microdensitometer. If all the light emerging from the film, i.e. direct and scattered components, are collected, one measures the so-called diffuse density. As the numerical aperture of the objective (O) decreases (see Fig.A-1-a), less scattered light is collected and the measured density increases. The correction, which depends on the particular scattering properties of each film, has been modeled and measured for No-screen by Brown (1976), Dozier (1976) et al. We checked that correction and extended it to RAR-2491. The Joyce-Loebl densitometer was equipped with four different objectives (numerical apertures .10, .25, .40, .85) to scan exactly the same region of samples

from each film. The results are shown on Figure A-2. In both cases the baseline is the same for the four traces. Note for example that on No-screen the density at the maximum of the $Al^{+11}(1s^2-1s2p)$ resonance line ("w") drops from 2.1 to 1.45 when the numerical aperture of the objective collecting the light is changed from .10 to .85. Our data for No-screen fit reasonably well the correction "measured density/diffuse density" suggested by Dozier et al. The correction required for RAR-2491 is very similar to the one used for No-screen.

The film calibration itself was done by recording spectra through Aluminum filters of various thicknesses (see Table A-1). Data for No-screen were taken around three wavelengths and compared to those given by Dozier et al. Data for RAR-2491 were taken around 7 Å-8 Å and compared with the calibration given for RAR-2490 by Benjamin et al (1977). *The results for No-screen are presented on* Figure A-3-a. Our H-D curves, arbitrarily positioned along the exposure scale to be in coincidence with Dozier's curves at low optical density, have significantly lower slopes. Much closer agreement is found between our data on RAR-2491 and Benjamin's data.

Note that the Aluminum spectrum was recorded simultaneously on No-screen and RAR-2491 (shots #2138 and 2201). Fig.A-2 shows that the line $Al^{+11}(w)$ has about the same density on both films, suggesting that the H-D curves should be close to each other around $D_{diffuse} \simeq 1.5$. This is confirmed by other data such as shots #2903 and 2904 where the spatially resolved spectra from identical step targets were successively recorded on RAR-2491 and No-screen. Possible causes of error, such as differences in filter thickness and crystal reflectivity between the

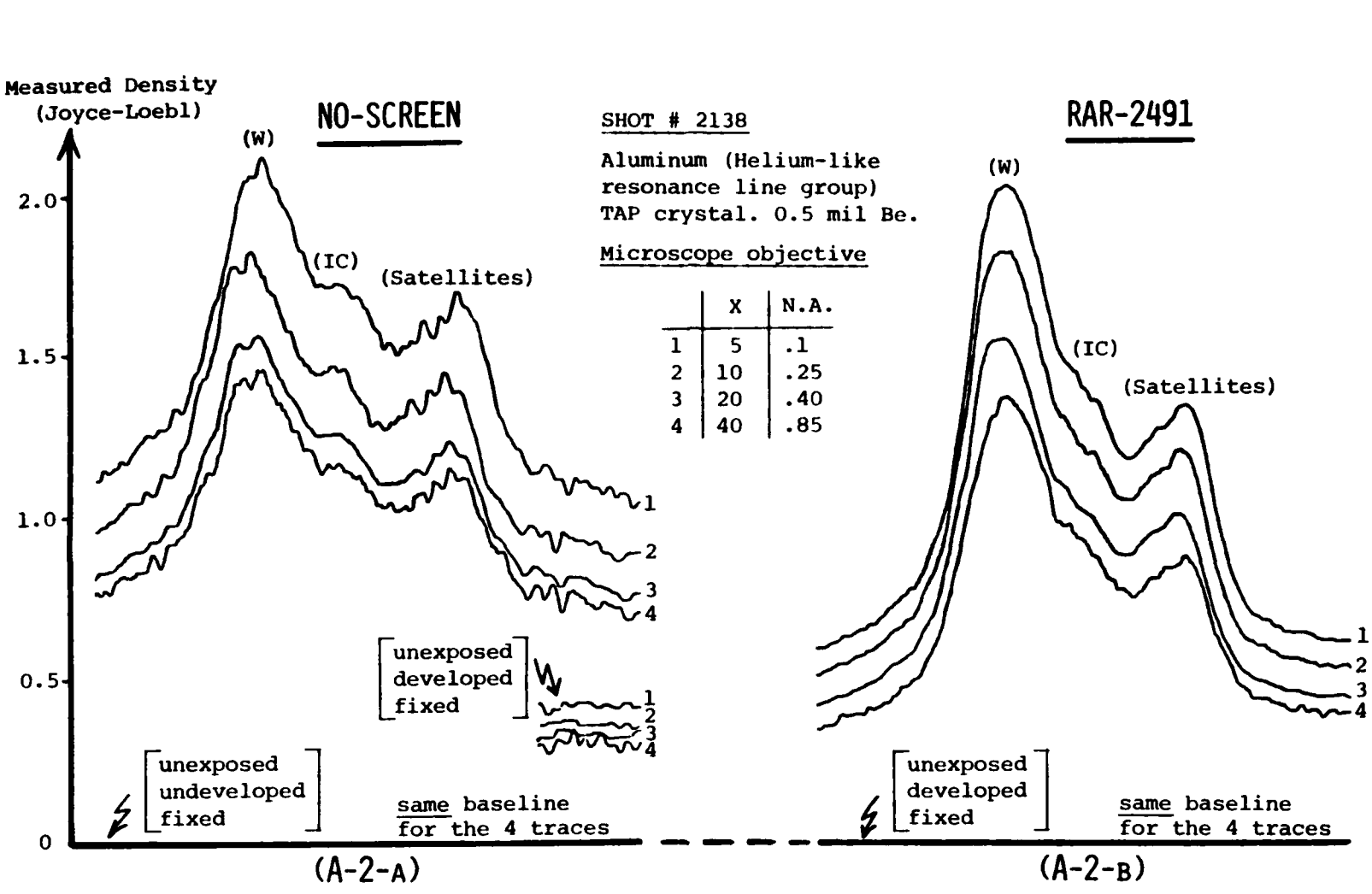

FIGURE A-2 : EFFECT OF THE MICROSCOPE OBJECTIVE COLLECTING THE LIGHT ON THE MEASURED OPTICAL DENSITY.

Film	Spectral line(s)	GDL shot	Aluminum filter		Reference*
NO-SCREEN	Ti^{+20} [$1s^2$-1s3p (2.23 Å) $1s^2$-1s2p (2.62 Å)	#1064 (β-tank) 39 J at 0.351 μm #1097 (β-tank) 37 J at 0.351 μm	n (15 μm)	n=0,1 n=0,1,2,3	V : K_α (2.50 Å)
	Cl^{+15} [$1s^2$-1s3p (3.79 Å) $1s^2$-1s2p (4.44 Å)	#1134 (β-tank) 35 J at 0.351 μm #1305 (β-tank) 39 J at 0.351 μm	n (15 μm)	n=0,1 n=0,1	K : K_α (3.74 Å) Cl: K_α (4.73 Å)
	Al^{+12} [Lyman α (7.17 Å)	#2138 (α-tank) 20 J at 1.054 μm #2201 (α-tank) 26 J at 1.054 μm	n (0.75 μm)	n=0,1,2 n=0,1,2,3	Si: K_α (7.13 Å)
RAR-2491	Al^{+12} [Lyman α (7.17 Å)	#2138 #2201 #2453 (α-tank) 15 J at 0.351 μm	n (0.75 μm)	n=0,1,2,3,4 n=0,1,2,3 n=0,1,2,3	Si: K_α (7.13 Å)

* No-screen : Dozier et al (1976)

RAR-2491 : Benjamin et al (1977)

TABLE A-1 : FILM CALIBRATION EXPERIMENTS.

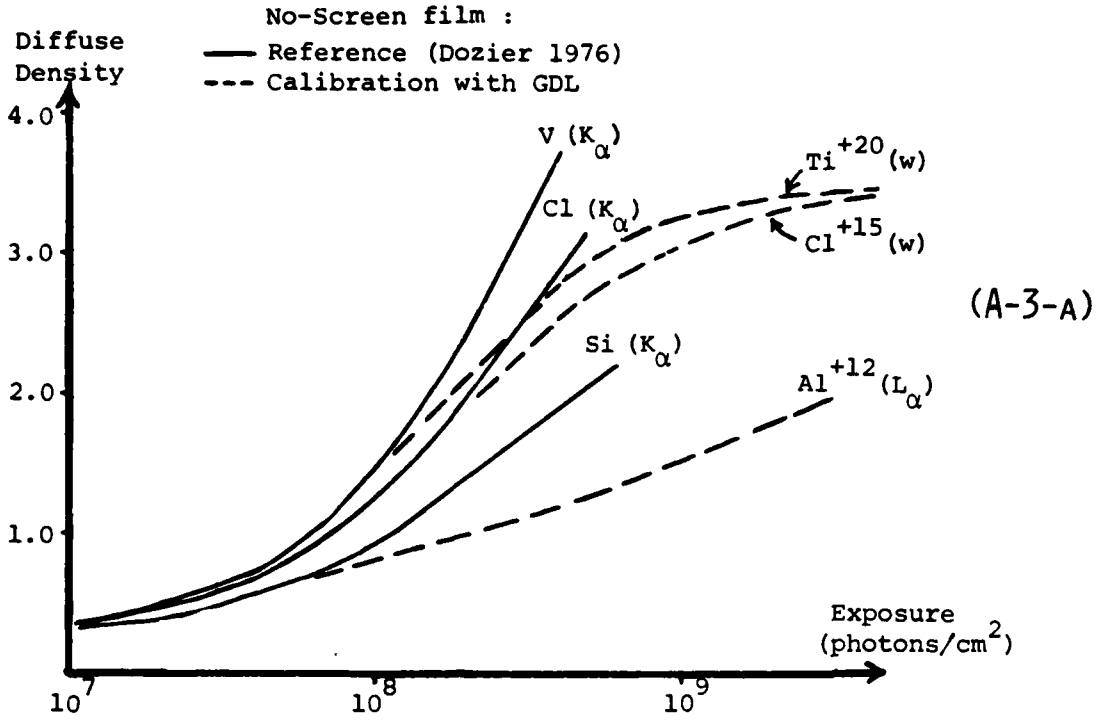

(A-3-A)

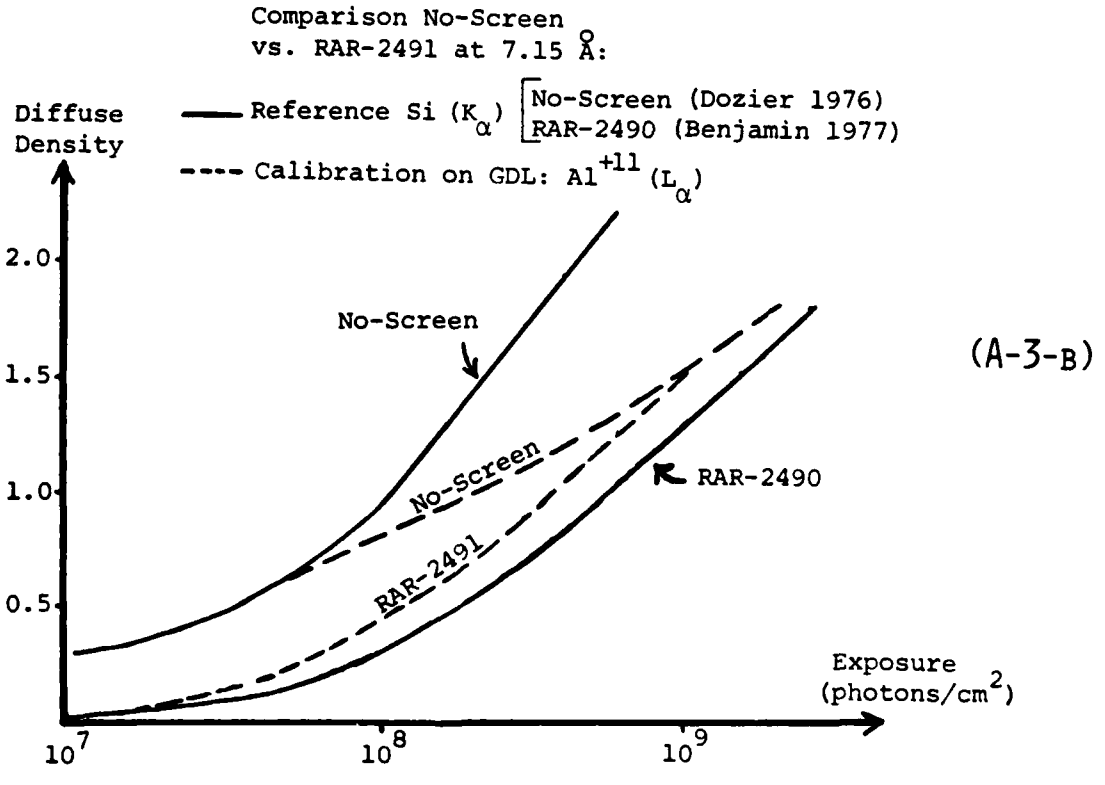

(A-3-B)

FIGURE A-3 : FILM CALIBRATION WITH GDL.

A- CALIBRATION OF NO-SCREEN FILM,

B- COMPARISON OF NO-SCREEN AND RAR-2491 FILMS.

spectrographs used to record the two spectra, were checked through control experiments. One has to take into account the fact that RAR-2491 is somewhat more sensitive than RAR-2490 in the blue. It may very well hold in the X-ray regime too. A translation of the RAR-2490 H-D curve (factor $\gtrsim$ 1.5 on the logarithmic scale for the exposures), combined with the correction previously mentioned for No-screen, make the data compatible. That double correction is shown on Figure A-3-b.

A-3. Code PHOTON.

The code carries out the procedure described in Sec.A-1. It contains film calibration curves for No-screen (1.6 Å to 11 Å) and RAR-2490 (1.6 Å to 44 Å) from Dozier and from Benjamin as well as our own curves over the same spectral range, using corrections consistent with those described in Sec.A-2. Tables (Dozier et al 1976) necessary for the conversion "measured density/diffuse density" are also included. That information is used as a grid: the exposure corresponding to any density for any numerical aperture at any wavelength within the grid is determined by linear interpolation from the nearest available curves.

The code requires as input the user' selection of a film calibration and the relevant parameters of the microdensitometer: magnification (M_o) and numerical aperture of the objective collecting the light, width (L_s) of the slit in front of the detector, scale of the density wedge, magnification (m) paper trace/film. It also requires for each spectral line the wavelength, width (FWHM), height at the peak and at the base of the profile on the paper trace. The output gives for each line the value of $(\mathcal{R}\mathcal{E}/L).N_T$, see Eq.A-2. $\mathcal{R}_l$ and $\mathcal{E}$ are readily

available in the literature, L is provided by another code (CRYSPEC, see Appendix B).

A-4. Photometry of the grating spectrograph.

Eq.A-1 given for the crystal spectrograph applies also to the grating spectrograph (see Fig.3-5) if the quantity $L/\mathcal{R}$ on the right-hand side is replaced by

$$d_0 [d_0 + r(\sin\alpha + \sin\beta)] / \xi s$$

ξ is the efficiency of the grating in the relevant order of diffraction, r its radius of curvature, α and β the incidence and diffraction angles measured from the surface of the grating, s and d_o the width of the entrance slit and its distance to the source, respectively. The same substitution can be made in the other equations of Sec.A-1. However the procedure for microdensitometry loses its relevance because the lines on the film are much narrower than they are in the non-focusing crystal spectrograph.

The film used, Kodak 101-01, was not calibrated because the diffraction efficiencies of our gratings at different wavelengths and for different orders were not known. References to 101-01 in the literature (Burton et al 1973, Koppel 1974) are limited to wavelengths outside the spectral range we are interested in (50 Å-200 Å) and it is unclear how an extrapolation should be done.

Appendix B

Experimental wavelength determination

Most of the data presented in this thesis were recorded with spectrographs whose dispersive element was either a flat (non-focusing) crystal or a concave (focusing) grating. When a crystal is used, the wavelength scale depends on the relative position of the source with respect to the spectrograph; the wavelength determination has to rely on some known lines in the recorded spectrum. When a grating is used, the wavelength scale is independent of the source position but needs to be determined with accuracy to get full benefit from the resolving power of the instrument.

This appendix describes for each case a method to determine the wavelength scale from the recorded spectrum itself provided that the wavelengths of a minimum number of lines are known. For completeness a method applying to the curved-crystal spectrograph is also presented. The curvature may be accidental (a "flat" crystal improperly characterized or subject to stress in its mount) or deliberate, to increase the spectral range of the spectrograph when the crystal cannot be positioned near the source.

B-1. Flat-crystal spectrograph.

B-1-a. Description of the problem.

Figure B-1 shows the geometrical arrangement of recording a spectrum of a point source for general angles α ($\alpha < 90^{\circ}$) between the film ($\mathcal{F}$) and crystal surface ($\mathcal{S}$) and ψ between $\mathcal{S}$ and the diffracting

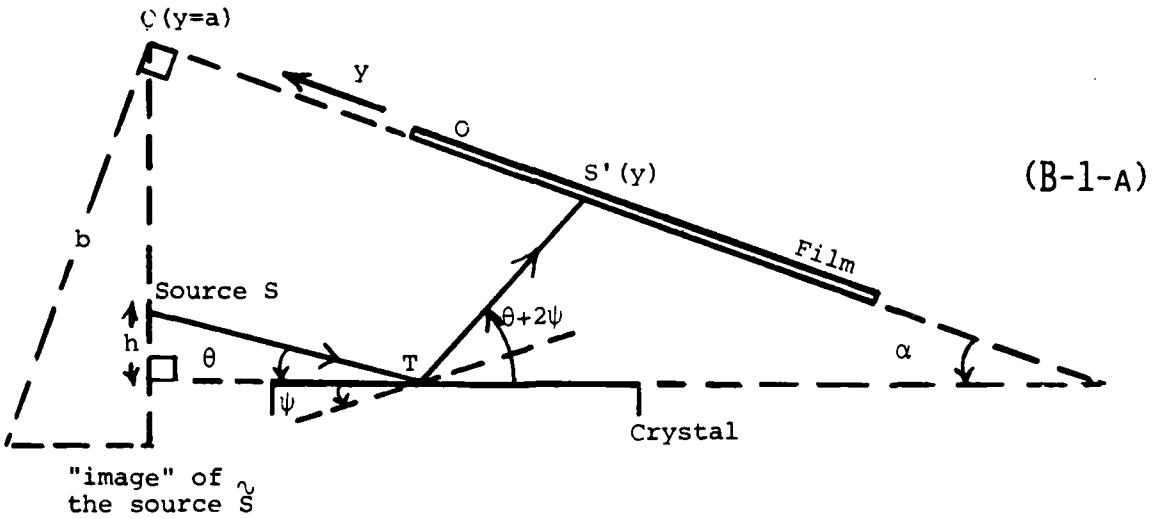

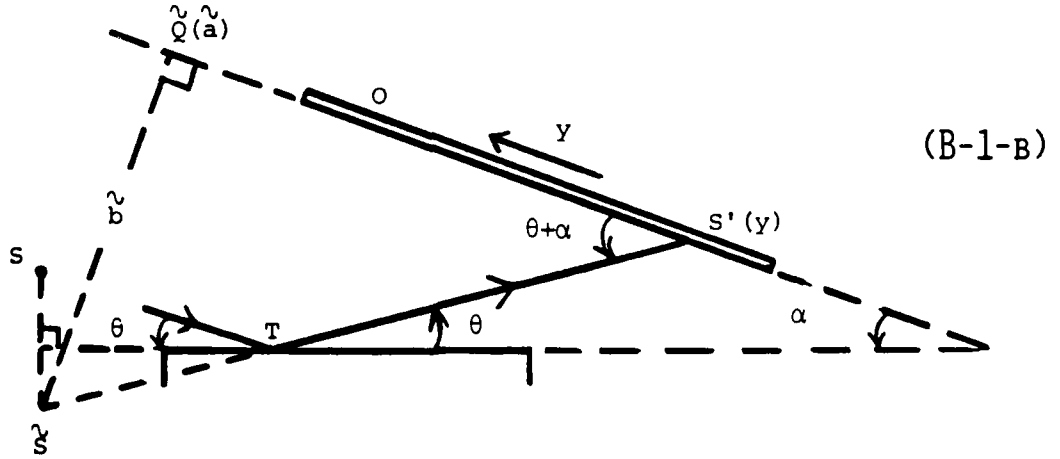

FIGURE B-1 : GEOMETRY OF A FLAT-CRYSTAL SPECTROGRAPH.

planes ($\mathcal{S}$). The normals to $\mathcal{F}$, $\mathcal{S}$ and $\mathcal{P}$ are assumed to be coplanar. The X-rays are diffracted according to Bragg's law $\lambda=2D.\sin(\theta+\psi) =2D.\sin\theta^*$, where D is the interplanar spacing of the crystal. One gets from Fig.B-1-a

$$y = a + b/[\tan\alpha + \tan(\theta^*+\psi)] + h \sin 2\psi / \sin(\theta^*-\psi) \sin(\alpha+\theta^*+\psi) \qquad (B\text{-}1)$$

Positions y on the film are measured with respect to an arbitrary point O whose distance to the point Q is a. The distance (STS') that the ray of wavelength λ travels from the source to the film is

$$L = [b \cos^2\alpha + 2 h \sin\psi \cos(\alpha+\theta^*) / \sin(\theta^*-\psi)] / \sin(\alpha+\theta^*+\psi) \qquad (B\text{-}2)$$

This distance is useful for (i) photometric calculations, (ii) the determination of the wavelength-dependent linear magnification of a slit in a spatially-resolving arrangement.

If a densitometer of magnification m is used, Eq.(B-1) still applies provided one makes the following substitutions: Y=my, A=ma, B=mb, H=mh. In the most general case Eq.(B-1) involves five independent parameters (A, B, α, H, ψ). The sensitivity of Y and L to these parameters is measured by the partial dervatives:

$$\partial Y/\partial A = 1$$

$$\partial Y/\partial B = [\tan\alpha + \tan(\theta^*+\psi)]^{-1}$$

$$\partial Y/\partial \alpha = -B(\partial Y/\partial B)^2 / \cos^2\alpha - H(\partial Y/\partial H) / \tan(\alpha+\theta^*+\psi) \qquad (B\text{-}3)$$

$$\partial Y/\partial H = \sin 2\psi / \sin(\theta^*-\psi) \sin(\alpha+\theta^*+\psi)$$

$$\partial Y/\partial \psi = -B(\partial Y/\partial B)^2 / \cos^2(\theta^*+\psi) + H(\partial Y/\partial H)^2 [\cos\alpha - \cos 2\psi \cos(\alpha+2\theta^*)]/\sin^2 2\psi$$

and

$$\partial L/\partial A = 0$$

$$m\,\partial L/\partial B = \cos^2\alpha / \sin(\alpha+\theta^*+\psi)$$

$$m\,\partial L/\partial\alpha = -[B(\tfrac{1}{2}\sin 2\alpha + \partial Y/\partial B) + H\,\partial Y/\partial H] / \sin(\alpha+\theta^*+\psi) \qquad \text{(B-4)}$$

$$m\,\partial L/\partial H = (\partial Y/\partial H)\cos(\alpha+\theta^*) / \cos\psi$$

$$m\,\partial L/\partial\psi = -B(m\,\partial L/\partial B)/\tan(\alpha+\theta^*+\psi) + H(m\,\partial L/\partial H)\,[\cos\psi + (\partial Y/\partial H)\sin(\alpha+2\psi)\,/\,2\cos\psi]$$

The dispersion in wavelength is

$$\partial Y/\partial\lambda = -[B(\partial Y/\partial B)^2/\cos^2(\theta^*+\psi) + H(\partial Y/\partial H)^2/\sin 2\psi\,\sin(\alpha+2\theta^*)]\,/\,2D\cos\theta^* \qquad \text{(B-5)}$$

B-1-b. Special case: $\psi = 0$ (Conturie et al 1981).

B-1-b-1. Analytic solution. In order to solve Eq.(B-1) one needs to have at least as many known lines in the spectrum as there are unknown parameters. In the general case it is best done on the computer. However one often chooses crystals cut along the direction of the diffracting planes, i.e. $\psi = 0$. Eq.(B-1) reduces to an expression analytically easy to handle:

$$\tan\theta = -\tan\alpha + B/(Y-A) \qquad \text{(B-6)}$$

In order to solve for the three parameters, A, B and $\tan\alpha$, one needs to know three lines in the spectrum. Calling the coordinates of these lines (Y_1,θ_1), (Y_2,θ_2), (Y_3,θ_3), and adopting for the indices the convention that i+3 stands for i, we have

$$A = \sum_{i=1,3} Y_i[\tan\theta_i(Y_{i+1}-Y_{i+2})] \Big/ \sum_{i=1,3} \tan\theta_i(Y_{i+1}-Y_{i+2})$$

$$B = -\prod_{i=1,3}(Y_i-Y_{i+1})(\tan\theta_i-\tan\theta_{i+1}) \Big/ \left[\sum_{i=1,3} Y_{i+2}(\tan\theta_i-\tan\theta_{i+1})\right]^2 \qquad \text{(B-7)}$$

$$\tan\alpha = -\sum_{i=1,3} \tan\theta_i[Y_i(\tan\theta_{i+1}-\tan\theta_{i+2})] \Big/ \sum_{i=1,3} Y_i(\tan\theta_{i+1}-\tan\theta_{i+2})$$

The partial derivatives are

$$\partial A/\partial Y_i = (Y_{i+1}-A)(Y_{i+2}-A) \Big/ (Y_{i+1}-Y_i)(Y_{i+2}-Y_i)$$

$$\partial B/\partial Y_i = -B[(Y_{i+1}-A)+(Y_{i+2}-A)] \Big/ (Y_{i+1}-Y_i)(Y_{i+2}-Y_i) \qquad \text{(B-8)}$$

$$\partial\tan\alpha/\partial Y_i = -B/(Y_{i+1}-Y_i)(Y_{i+2}-Y_i)$$

If errors ΔY_i (i=1,3) are made in the true positions of the three reference lines, the error in the deduced wavelength of an unknown line (Y,θ) can be obtained by differentiating Eq.(B-6) with respect to Y_i (i=1,3). The result is

$$\Delta(\tan\theta) = -B \sum_{i=1,3} (Y-Y_{i+2})(Y-Y_{i+1})(Y_{i+2}-Y_{i+1})\Delta Y_i \Big/ (Y-A)^2 \prod_{i=1,3}(Y_{i+2}-Y_{i+1}) \qquad \text{(B-9)}$$

<u>B-1-b-2.</u> <u>Discussion of the solution.</u> We have not included the 2D-spacing of the crystal among the parameters. Its value is usually well known and, in addition, the wavelength determination is insensitive to an error in it. Differentiation of the Bragg condition and of Eq.(B-6) leads to

$$\partial\lambda/\partial(2D) = \lambda/2D + 2D\cos^3\theta\,\partial\tan\theta/\partial(2D) \qquad \text{(B-10)}$$

$$\partial\tan\theta/\partial(2D) = -\partial\tan\alpha/\partial(2D) + \{\partial B/\partial(2D) + [B/(Y-A)]\partial A/\partial(2D)\}/(Y-A) \qquad \text{(B-11)}$$

For the three reference lines, $\partial\lambda_i/\partial(2D) = 0$ (i=1,3), and one can solve for the quantities $\partial A/\partial(2D)$, $\partial B/\partial(2D)$, and $\partial\tan\alpha/\partial(2D)$. The resulting error in the measured wavelength is given by

$$\partial\lambda/\partial(2D) = (2D)^{-3} \prod_{i=1,3} (\lambda - \lambda_i \cos\theta/\cos\theta_i) \qquad \text{(B-12)}$$

In most cases the right-hand side of Eq.(B-12) is very small ($\lesssim 10^{-4}$), and the value of the 2D-spacing need not be known with great accuracy.

Since the parameter $\tan\alpha$ is easy to measure and does not change with the position of the spectrometer, we single it out and show here that the measurement of $\tan\alpha$ with only modest precision can improve considerably the precision in determining the wavelength of an unknown line. Starting with Eq.(B-6) and assuming that $\tan\alpha$ is known, we solve for A and B:

$$A = [Y_2(\tan\theta_2 + \tan\alpha) - Y_1(\tan\theta_1 + \tan\alpha)] \;/\; (\tan\theta_2 - \tan\theta_1)$$
$$B = -[(Y_2 - Y_1)/(\tan\theta_2 - \tan\theta_1)](\tan\theta_2 + \tan\alpha)(\tan\theta_1 + \tan\alpha) \qquad \text{(B-13)}$$

Their partial derivatives are (with the convention i+2=i)

$$\partial A/\partial Y_i = (\tan\theta_i + \tan\alpha) \;/\; (\tan\theta_i - \tan\theta_{i+1})$$
$$\partial B/\partial Y_i = B \;/\; (Y_i - Y_{i+1}) \qquad \text{(B-14)}$$

The differentiation with respect to $\tan\alpha$ of Eq.(B-6), where A and B are functions of $\tan\alpha$ (see Eq.(B-13)), allows us to compute the error in the determination of the wavelength of an unknown line (Y,θ) for a given error in $\tan\alpha$:

$$\partial\lambda/\partial\tan\alpha = -2D[1-(\lambda/2D)^2]^{3/2}(Y-Y_1)(Y-Y_2)/(Y-A)^2 \qquad \text{(B-15)}$$

An error of 1^{o} in α will cause an error in the wavelength $\Delta\lambda/\lambda$ of $\sim 2\ 10^{-4}$. The error in A and B from Eq.(B-14) is about one order of magnitude smaller than that given by Eq.(B-8). The error in the determined wavelength that is due to errors in Y_i (i=1,2) is obtained by differentiating Eq.(B-6) and by using Eq.(B-14):

$$\Delta\lambda = 2D[1-(\lambda/2D)^2]^{3/2} B[(Y-Y_2)\Delta Y_1-(Y-Y_1)\Delta Y_2]/[(Y_1-Y_2)(Y-A)^2] \qquad (B\text{-}16)$$

B-1-b-3. Dispersion characteristics. When $\psi=0$, Eq.(B-5) reduces to

$$\partial Y/\partial\lambda = -B\cos^2\alpha \ / \ 2D\cos\theta\sin^2(\alpha+\theta) \qquad (B\text{-}17)$$

It is convenient to use the dimensionless quantities $U=(Y-A)/B$, $\Lambda=\lambda/2D$, $\Sigma=1/\Lambda$ to compute the dispersions in wavelength $\partial U/\partial\Lambda$ and wavenumber $\partial U/\partial\Sigma$. Results are summarized in Table B-1 and illustrated in Figures B-2-a and B-2-b. The flat-crystal spectrograph is not a constant dispersion device (neither in wavelength nor in frequency), which precludes extrapolation far outside of the range where known lines lie. For any angle $0^{o}<\alpha<90^{o}$, $\partial U/\partial\Lambda$ goes through an extremum for some wavelength $\Lambda=\Lambda_o(\alpha)$, while this happens to $\partial U/\partial\Sigma$ only for negative values of α. $\partial U/\partial\Lambda$ varies less when α is large, $\partial U/\partial\Sigma$ varies less when α is small. The dispersion in wavelength is relatively constant around the extremum, where a linear interpolation might yield acceptable precision. To estimate the error in using a linear interpolation we develop the function $U(\Lambda)$ in a series expansion around the extremum $\Lambda=\Lambda_o$ up to third order (the second order term, of course, vanishes). We finally get for the error

$$(\Lambda-\Lambda^*)/\Lambda \simeq -(\Lambda-\Lambda_1)(\Lambda-\Lambda_2)(\Lambda+\Lambda_1+\Lambda_2-3\Lambda_o).(1-\Lambda_o^2/2)/[2\Lambda(1-\Lambda_o^2)^2] \qquad (B\text{-}18)$$

Dispersion in wavelength ($\Lambda = \lambda / 2D$)	Dispersion in wavenumber ($\Sigma = 2D / \lambda$)
$\partial U/\partial\Lambda = -(1-\Lambda^2)^{-\frac{1}{2}}(\Lambda + \sqrt{1-\Lambda^2}\ \tan\alpha)^{-2}$	$\partial U/\partial\Sigma = \Sigma\ (\Sigma^2-1)^{-\frac{1}{2}}(1 + \sqrt{\Sigma^2-1}\ \tan\alpha)^{-2}$
$\partial^2 U/\partial\Lambda^2 = 0$ for $\Lambda=\Lambda_0$ such that	$\partial^2 U/\partial\Sigma^2 = 0$ for $\Sigma=\Sigma_0$ such that
$\tan\alpha = (1 - 3\,\Lambda_0^2/2)\ /(3\,\Lambda_0/2)\ \sqrt{1-\Lambda_0^2}$	$\tan\alpha = -[(2\,\Sigma_0^2 + 1)\ \sqrt{\Sigma^2-1}\ ]^{-1}$
It corresponds to a minimum of $-\partial U/\partial\Lambda$:	It corresponds to a minimum of $\partial U/\partial\Sigma$:
$[\partial U/\partial\Lambda]_{\Lambda_0} = -\,9\,\Lambda_0^2/\,4\,\sqrt{1-\Lambda_0^2}$	$[\partial U/\partial\Sigma]_{\Sigma_0} = (2\,\Sigma_0^2+1)^2\ /\ 4\,\Sigma^3\ \sqrt{\Sigma_0^2-1}$
Also $U(\Lambda_0) = (3\,\Lambda_0/2)\ \sqrt{1-\Lambda_0^2}$	Also $U(\Sigma_0) = (1+\,1/\,2\Sigma_0^2)\ \sqrt{\Sigma_0^2-1}$
$\partial U/\partial\Lambda \to -\infty$ when $\Lambda \to -\sin\alpha$	$\partial U/\partial\Sigma \to +\infty$ when $\Sigma \to -1/\sin\alpha$
$\partial U/\partial\Lambda \to -\infty$ when $\Lambda \to 1$	$\partial U/\partial\Sigma \to +\infty$ when $\Sigma \to 1$
$\partial U/\partial\Lambda \to -1/\tan^2\alpha$ when $\Lambda \to 0$	$\partial U/\partial\Sigma \to 0$ when $\Sigma \to +\infty$ (except when $\alpha=0$. Then $\partial U/\partial\Sigma \to 1$)

TABLE B-1 : DISPERSION CHARACTERISTICS OF A FLAT-CRYSTAL SPECTROGRAPH.

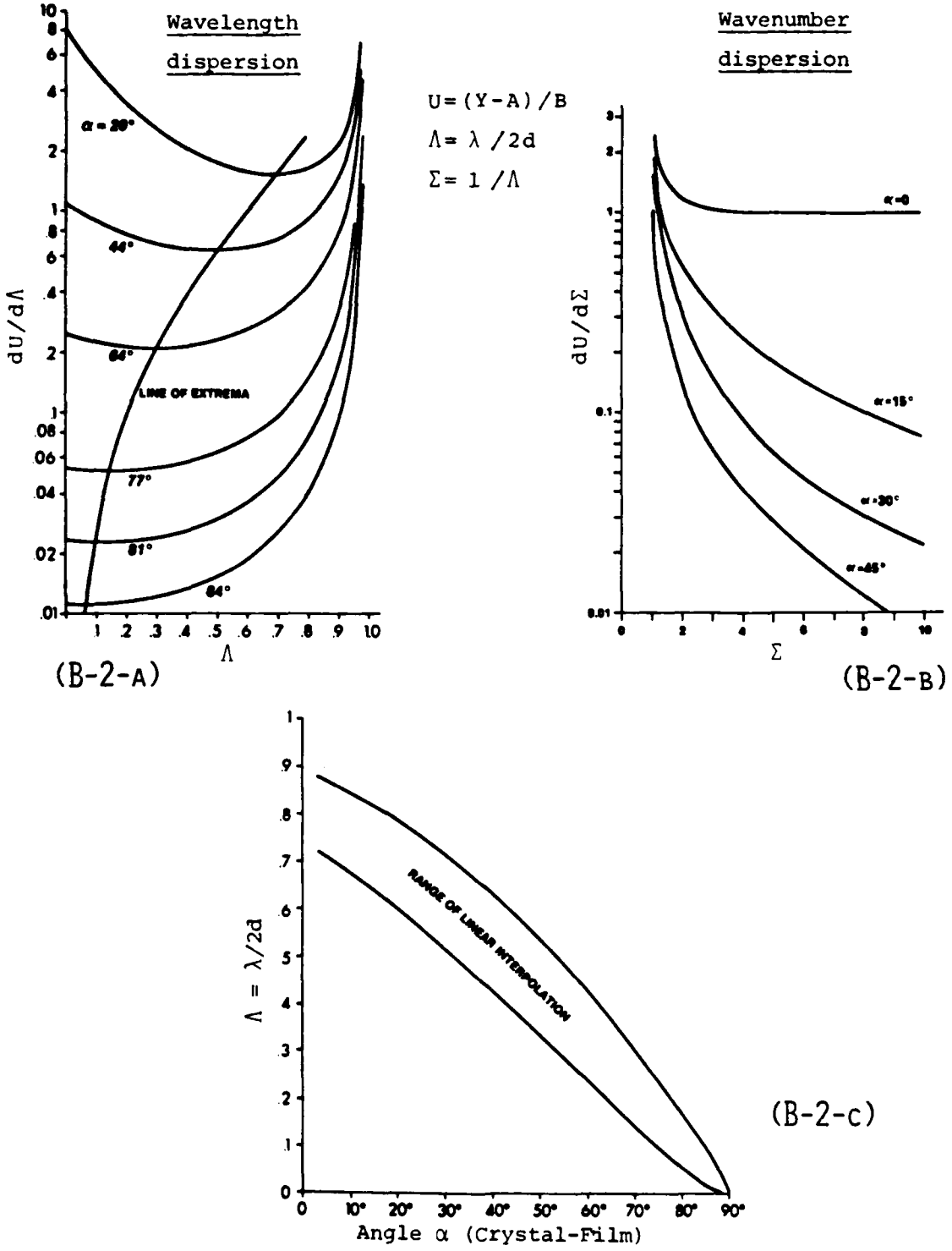

FIGURE B-2 : DISPERSION CHARACTERISTICS OF A FLAT-CRYSTAL SPECTROGRAPH.

Here Λ_1, Λ_2 are two known wavelengths, Λ is the actual value of an unknown line and Λ^* the wavelength of the same line obtained by linear interpolation between Λ_1 and Λ_2. Eq.(B-18) is valid in a limited range around Λ_o, i.e. in the region where the curve $\partial U/\partial\Lambda$ is reasonably symmetric. Outside that region the Taylor expansion must be pushed further. The upper bound of $|\Lambda-\Lambda^*|/\Lambda$ for any wavelength $\Lambda \in [\Lambda_1, \Lambda_2]$ within the range of validity of Eq.(B-18) is

$$|\Lambda-\Lambda^*|/\Lambda < \{ (1-\Lambda_o^2/2)/[4\Lambda(1-\Lambda_o^2)^2] \} . \text{Max} \{ |\Lambda_1-\Lambda_o|^3, |\Lambda_2-\Lambda_o|^3 \} \qquad \text{(B-19)}$$

We plot in Figure B-2-c for each angle α a range of wavelengths within which linear interpolation will yield a relative error smaller than 10^{-3}.

When the angle α is known accurately, it is convenient to rewrite Eq.(B-6) as follows:

$$Y = \tilde{A} + \tilde{B} \cot an(\alpha+\theta) \qquad \text{(B-20)}$$

where $\tilde{A}=A + B.\sin\alpha .\cos\alpha$, $\tilde{B}=B.\cos^2\alpha$ (see Fig.B-1-b). The graph Y versus $\cot an(\alpha+\theta)$ is a straight line and a linear interpolation is possible for any value of α. Also the dispersion in wavelength $\partial Y/\partial\lambda = -\tilde{B}/\sin^2(\alpha+\theta)$ derived from Eq.(B-20) remains valid for $\alpha = 90^\circ$ because $\tilde{B}$ is finite (while B becomes infinite).

B-2. Curved-crystal spectrograph.

Mechanical constraints or the risk of damage from target blow-off may require that the spectrograph be set at a large distance from the source, reducing the range of angles, hence wavelengths, incident on a flat crystal. The spectral range may be increased by using a curved crystal. The relevant geometry is presented on Figure B-3. We limit our analysis to the case where the diffracting planes are parallel to the surface of the crystal. Five independent parameters are needed to define the problem:

CN = r : radius of curvature of the crystal (center C),

CS = s : distance from C to the source S,

CH = h : distance from C to the film $\mathcal{F}$,

(CH,CS) = α : (defines the orientation of the film),

$\overline{OA}$ = $\bar{y}$: (defines the origin O on the y-axis along the film).

Once again the X-rays are diffracted according to Bragg's law, $\lambda = 2D.\sin\theta$, where D is the interplanar spacing of the crystal. One gets from Fig.B-4

$$\sin\beta = (r/s)\cos\theta \qquad \text{(B-21)}$$

$$y = \bar{y} + [h\sin(\beta+2\theta)/\cos\alpha - r\cos\theta]/\cos(\alpha+\beta+2\theta) \qquad \text{(B-22)}$$

$$L = [2s\tan\theta\cos^2(\beta+\theta) + (\bar{y}-y)\cos\alpha]/\sin(\beta+2\theta) \qquad \text{(B-23)}$$

y defines the position of the line of wavelength λ on the film. L is the distance (STS') the ray of wavelength λ travels from the source to the film. If a densitometer trace of magnification m is used, one can make the substitutions: Y=my, R=mr, S=ms, H=mh, Y=my. The sensitivity

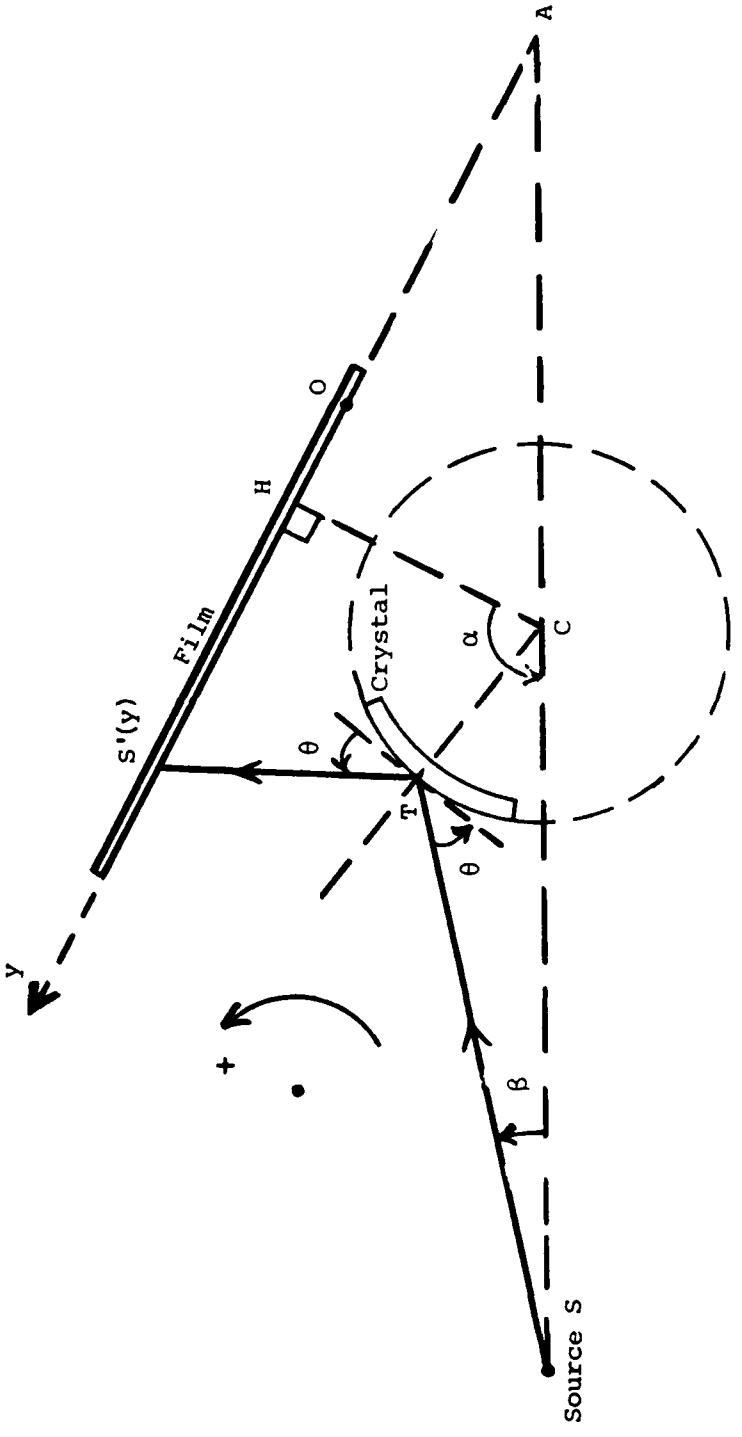

FIGURE B-3 : GEOMETRY OF A CURVED-CRYSTAL SPECTROGRAPH.

of Y and L to the five parameters is measured by the partial derivatives:

$$\partial Y/\partial R = -(S/R)\,\partial Y/\partial S + (m\,\partial L/\partial H)\cos\theta$$

$$\partial Y/\partial S = -(\tan\beta/S)\,(\partial Y/\partial\alpha + H/\cos^2\alpha)$$

$$\partial Y/\partial H = -(m\,\partial L/\partial H)\sin(\beta+2\theta)/\cos\alpha \qquad \text{(B-24)}$$

$$\partial Y/\partial\alpha = (Y-\bar{Y})\tan(\alpha+\beta+2\theta) + H\tan\alpha\,\partial Y/\partial H$$

$$\partial Y/\partial\bar{Y} = 1$$

and

$$m\,\partial L/\partial R = \{\cos\alpha\,[S\cos(\alpha+2\theta) - H]/\cos^2(\alpha+\beta+2\theta) - m\,L\cos(\beta+2\theta) - 2S\tan\theta\sin 2(\beta+\theta)\}\tan\beta/R\sin(\beta+2\theta)$$

$$m\,\partial L/\partial S = (L - R\,\partial L/\partial R - H\,\partial L/\partial H)/S \qquad \text{(B-25)}$$

$$m\,\partial L/\partial H = -1/\cos(\alpha+\beta+2\theta)$$

$$m\,\partial L/\partial\alpha = [R\cos\theta - H\sin(\alpha+\beta+2\theta)]/\cos^2(\alpha+\beta+2\theta)$$

$$\partial L/\partial\bar{Y} = 0$$

The dispersion in wavelength is

$$\partial Y/\partial\lambda = [S\,(\tan\theta - 2/\tan\beta)\,\partial Y/\partial S + R\sin\theta/\cos(\alpha+\beta+2\theta)]/2D\cos\theta \qquad \text{(B-26)}$$

B-3. Grating spectrograph.

B-3-a. Description of the problem.

Figure 3-5 shows the geometrical set-up of an EUV grating spectrograph. The grating acts as both the dispersive element and a 1-dimensional imaging element. For each wavelength the image of the entrance slit is formed on the film. There is focussing only in the direction parallel to the Rowland circle's plane. One gets from Fig.3-5

$$k\lambda/p = \cos\alpha - \cos[(y+a)/r] = \cos\alpha - \cos\beta^{(k)} \qquad \text{(B-27)}$$

$$L = r(\sin\alpha + \sin\beta) \qquad \text{(B-28)}$$

p and r are the spatial period and radius of curvature of the grating. Positions y on the film are measured with respect to an arbitrary point O whose distance to the center of the grating along the Rowland circle is a. α is the angle of incidence and $\beta^{(k)}$ the angle of diffraction for the wavelength λ in the kth order. L is the distance (SCS') the ray of wavelength λ travels from the entrance slit to the film. If a densitometer trace of magnification m is used, one can make the substitutions: Y=my, A=ma, R=mr. There are three independent parameters (A, R, α). The sensitivity of Y and L to these parameters is measured by the partial derivatives:

$$\begin{aligned} \partial Y/\partial A &= -1 \\ \partial Y/\partial R &= \beta \\ \partial Y/\partial \alpha &= R\sin\alpha/\sin\beta \end{aligned} \qquad \text{(B-29)}$$

$$\begin{aligned} \partial L/\partial A &= 0 \\ m\,\partial L/\partial R &= \sin\alpha + \sin\beta \\ m\,\partial L/\partial \alpha &= R\cos\alpha \end{aligned} \qquad \text{(B-30)}$$

The dispersion in wavelength is $\partial Y/\partial\lambda = kR/p\sin\beta$

B-3-b. Discussion.

In order to solve for the three parameters A, R, α, one needs to know three lines in the spectrum. Let us call the coordinates of these lines (Y_1,λ_1), (Y_2,λ_2) and (Y_3,λ_3). The presence of trigonometric functions in Eq.B-27 does not make possible an explicit solution for each parameter, similar to Eq.B-7. Using a cosine expansion, one gets the following results in first order:

$$A \simeq -\tfrac{1}{2} \sum_{i=1,3} (\lambda_{i+2}-\lambda_{i+1})Y_i^2 \Big/ \sum_{i=1,3} (\lambda_{i+2}-\lambda_{i+1})Y_i$$

$$R \simeq \left\{-p/2 \prod_{i=1,3} (Y_{i+2}-Y_{i+1}) \Big/ \sum_{i=1,3} (Y_{i+2}-Y_{i+1})\lambda_i\right\}^{\frac{1}{2}} \qquad \text{(B-31)}$$

$$\sum_{i=1,3} (Y_{i+2}-Y_{i+1})\sqrt{2\lambda_i + p\alpha^2} \simeq 0$$

However, it is best to solve for an exact solution on the computer. When one or more parameters are known from previous recordings with the same instrumental set-up, the knowledge of less than three lines can be enough. The algebra to compute the remaining parameters becomes straightforward. It is not presented here.

We have not included among the parameters the spatial period p of the grating ($p_{(\mathring{A})}=10^7/n$; n=number of grooves/mm). The expression $d\lambda/dn$ was derived for each possible combination of free parameters. The results are summarized in Table B-2 where β_1, β_2, β_3 are the diffraction angle(s) of the reference line(s) used in the analytic solution: $\beta_i=(Y_i+A)/R$. The table gives in each case the lower order term (but by far the dominant one) of the exact solution. Note that $d\lambda/dn$ goes as $\beta^2/2!$ (or $\alpha^2/2!$) except in cases "2-3" and "1-2-3" where it goes as

Option	Free parameters	$d\lambda(\mathring{A})$ / $dn(mm^{-1})$ in units of $10^7/n^2$
1	X_1	$-(1+\alpha^2/\beta\beta_1)(1-\beta_1/\beta)\ \beta^2/2$
2	X_2	$[1-(\beta/\beta_1)^2]\ \alpha^2/2$
3	X_3	$-[1-(\beta_1/\beta)^2]\ \beta^2/2$
2-3	X_2, X_3	$-[1-(\beta_1/\beta)^2][1-(\beta_2/\beta)^2]\ \beta^4/4!$
3-1	X_3, X_1	$-(1-\beta_1/\beta)(1-\beta_2/\beta)\ \beta^2/2$
1-2	X_1, X_2	$(1-\beta/\beta_1)(1-\beta/\beta_2)\ \alpha^2/2$
1-2-3	X_1, X_2, X_3	$-(1+\sum_{i=1,3}\beta_i/\beta)[\prod_{i=1,3}(1-\beta_i/\beta)]\ \beta^4/4!$

$$\begin{cases} X_1 = m\,a = A \\ X_2 = m\,r = R \\ X_3 = \alpha \end{cases}$$

β, β_i in radian

TABLE B-2 : EFFECT ON THE LINE IDENTIFICATION OF AN ERROR IN THE GRATING' SPATIAL PERIOD, IN A EUV SPECTROGRAPH.

$\delta^4/4!$. In first approximation a change Δn in the number of grooves per mm of the grating does not affect the relationship $\lambda \leftrightarrow Y$ if it can be compensated by changes

$$\Delta A = 0 \quad ; \quad \Delta R = -(R/2)\,\Delta n/n \quad ; \quad \Delta\alpha = [\tan(\alpha/2)]\,\Delta n/n$$

This of course is possible only if R and α are both free parameters. The three quantities m, r and n are often reasonably well known in advance but the addition of just one free parameter, namely R=mr, takes care of the uncertainty on all three at the same time.

B-4. Least-squares optimization.

B-4-a. Analysis.

When the number (N) of known lines in the spectrum is larger than the number (M) of unknown parameters, one can improve on the accuracy of the analytical solution given above by doing a least-square fit with the free parameters X_j (j=1,M). The errors in the parameters and in the wavelength determination are now determined by a statistical method. Let us label the N reference lines as follows: $Y_i \pm \Delta Y_i$, $\lambda_i \pm \Delta\lambda_i$ (i=1,N), where ΔY_i corresponds to the uncertainty in the position of the line center for the ith line and $\Delta\lambda_i$ refers to the accuracy of the tabulated wavelengths. We define the real position $Y_i+\delta Y_i$ corresponding to the wavelength λ_i by a normalized probability distribution

$$P_{(\lambda_i,\delta Y_i)} = \frac{\pi^{-\frac{1}{2}}}{\Delta Y_i + (\partial Y/\partial\lambda)_i \Delta\lambda_i} \exp - \left[\frac{\delta Y_i}{\Delta Y_i + (\partial Y/\partial\lambda)_i \Delta\lambda_i}\right]^2 \qquad \text{(B-32)}$$

We further assume that the errors ΔY_i's made in the measured position of

the N lines are independent of each other, i.e. $< \delta Y_i . \delta Y_{i'} >_{i \neq i'} = 0$.

Using Eq.B-32, we have

$$< \delta X_j . \delta X_{j'} > = \tfrac{1}{2} \sum_{i=1,N} (\partial X_j / \partial Y_i)(\partial X_{j'} / \partial Y_i) [\Delta Y_i + (\partial Y / \partial \lambda)_i \Delta \lambda_i]^2 = \tfrac{1}{2} S_{jj'} \qquad \text{(B-33)}$$

The knowledge of ($X_j, S_{jj'}$; j=1,M, and j'=1,M) allows us to find

- the position of a given wavelength $Y = f[(X_j), \lambda]$,
- the wavelength of an unknown line $\lambda = f^{-1}[(X_j), Y]$, (B-34)
- in each case, the distance $L = g[(X_j), \lambda]$,

  source-film (crystal spectrograph) or

  entrance slit-film (grating spectrograph)

and to compute the rms errors associated with the solution of Eq.B-34:

$$\text{rms}(\delta X_j) = (\tfrac{1}{2} S_{jj'})^{\frac{1}{2}} \qquad \underline{a}$$

$$\text{rms}(\delta Y) = \{ \tfrac{1}{2} \sum_{j=1,M} \sum_{j'=1,M} (\partial Y / \partial X_j)(\partial Y / \partial X_{j'}) S_{jj'} \}^{\frac{1}{2}} \qquad \underline{b}$$

$$\text{rms}(\delta \lambda) = (\partial \lambda / \partial Y)\ \text{rms}(\delta Y) \qquad \underline{c} \qquad \text{(B-35)}$$

$$\text{rms}(\delta L) = \{ \tfrac{1}{2} \sum_{j=1,M} \sum_{j'=1,M} (\partial L / \partial X_j)(\partial L / \partial X_{j'}) S_{jj'} \}^{\frac{1}{2}} \qquad \underline{d}$$

The partial derivatives $\partial Y / \partial X_j$, $\partial L / \partial X_j$ (j=1,M) needed to compute quantities B-35-b and B-35-d were given in the previous sections: see Eq.B-3 and B-4, Eq.B-24 and B-25, Eq.B-29 and B-30.

FORTRAN programs were written to carry out these calculations. Their filenames are CRYSPEC (for the flat-crystal spectrograph), CURVEX (curved-crystal) and GRASPEC (grating). The parameters derived from the analytical solution with M known lines are used as initial values for the least-squares fitting. Let us define $F_i = Y_i - f[(X_j), \lambda_i]$.

The program searches for the values of X_j (j=1,M) that minimize the quantity ΣF_i^2 (i=1,N). It computes the matrix $\| \partial X_j / \partial Y_i \|$ whose components are needed in Eq.B-33:

$$\| \partial X_j / \partial Y_i \| = (J^t J)^{-1}_{jk} J^t_{ki} \qquad \text{(B-36)}$$

where J is the jacobian matrix $\| \partial F_i / \partial X_j \|$ and J^t is the transposed matrix. The program output includes the solution to Eq.B-34 and B-35 and the value of the local dispersion $(\partial Y / \partial \lambda)$ for each line.

B-4-b. Examples.

The program CRYSPEC has been tested with a large number of known spectra in the region 1-20 Å. The uncertainties ΔY_i and $\Delta \lambda_i$ in the reference lines were set equal to the half-width at half-maximum and to one unit of the last digit listed in Kelly & Palumbo (1973), respectively. The difference between the wavelength determination from the spectrum with our method and the tabulated value was always within the error bar ($\Delta\lambda / \lambda \lesssim 10^{-3}$) predicted by the program. An example is shown in Figure B-4. A Chlorine spectrum was recorded with a P.E.T. crystal (tetragonal: $a_1 = a_2 = 6.16$ Å; $a_3 = 8.74$ Å). The spectra produced by two sets of diffracting planes were recorded simultaneously. One set was (0,0,2), parallel to the surface, 2D=8.74 Å. It allowed the determination of the parameters A, B and α (see Sec.B-1). The remaining lines were then found to have been diffracted by the set (0,1,3), $\psi = 25^\circ\ 20'$, 2D=5.27 Å. The parameter H was also computed.

The program GRASPEC has been used to identify many spectra in the range 45 Å-200 Å, from Beryllium (Z=4) to Iron (Z=26), with gratings of

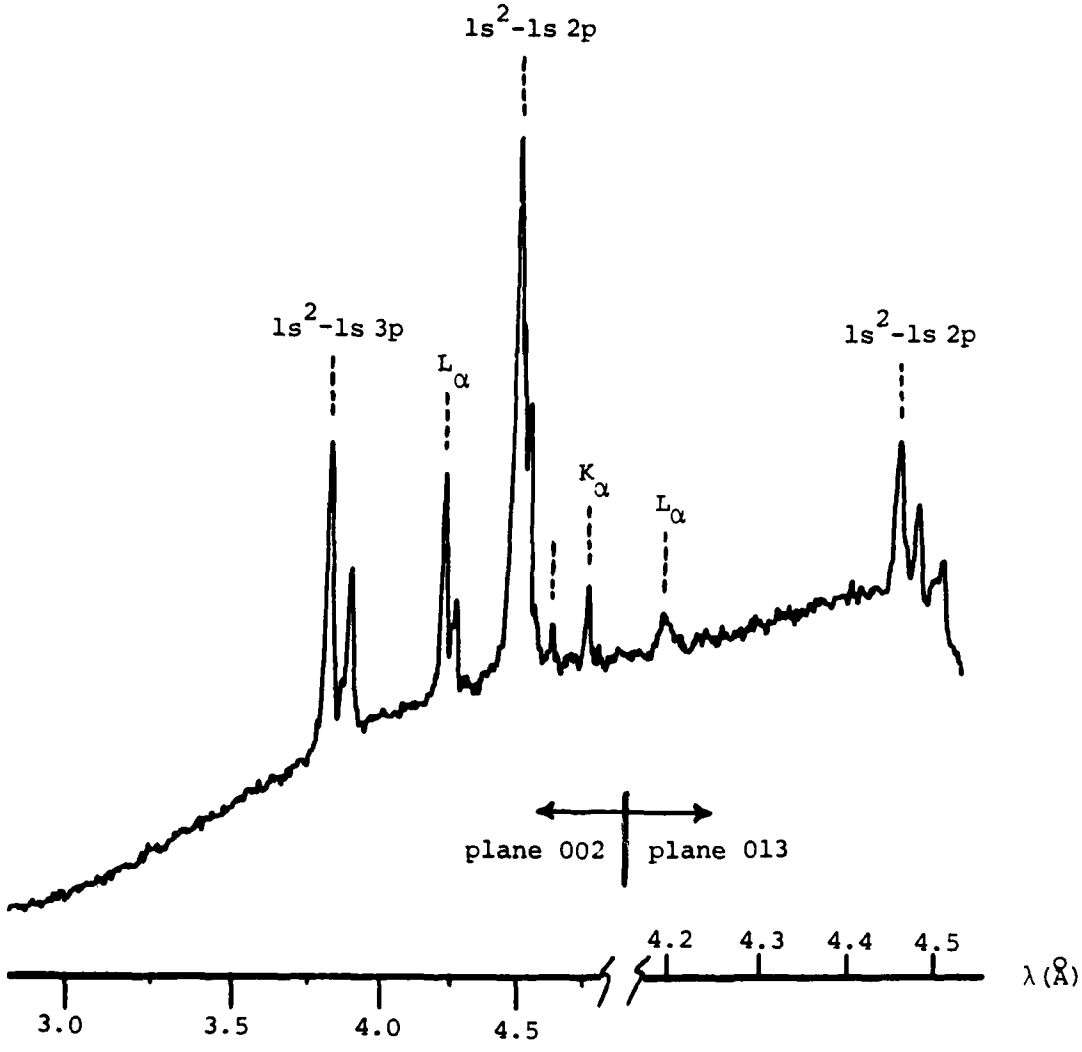

FIGURE B-4 : CHLORINE SPECTRUM DIFFRACTED BY 2 SETS OF CRYSTALLOGRAPHIC PLANES (PET 002 AND 013).

600, 1200 and 2400 grooves/mm. Wavelengths and error bars were consistent with published data. Some examples can be found in Chapter 4.

Appendix C

Design and fabrication of the cylindrical optics

The beam produced by the Glass Development Laser and the lens used to focus it on target are well characterized in both the IR and the UV configurations (Seka et al 1980 & 1981). In some of our experiments we needed to add a blast-shield to protect the lens from target blow-off and/or a cylindrical optics to form a line-focus. This appendix describes a ray-tracing code written to evaluate how the blast-shield affects the intensity distribution on target, in a point-focus or a line-focus geometry. It also describes several options for the cylindrical optics, the design that was chosen (a pair of weakly diverging corrector plates) and the manufacturing process.

C-1. Ray-tracing code.

In high intensity experiments on flat targets, the plasma blow-off occurs mainly in the direction of the incident laser. When a cooling plate is added in front of the target, the expanding plasma can produce hot debris which are then thrown toward the focusing optics, damaging its coating. An inexpensive glass plate, inserted at an angle to avoid back reflection and ghost formation along the axis of the laser, is used as a shield (see Figure C-1-a). The code (filename LINFOC) can propagate a uniform parallel beam through a 2-focus lens followed by a glass plate (i) of any index and thickness, (ii) with any tilt in any direction. Since the introduction of the glass plate and/or the astigmatism of the cylindrical optics are the main factors influencing

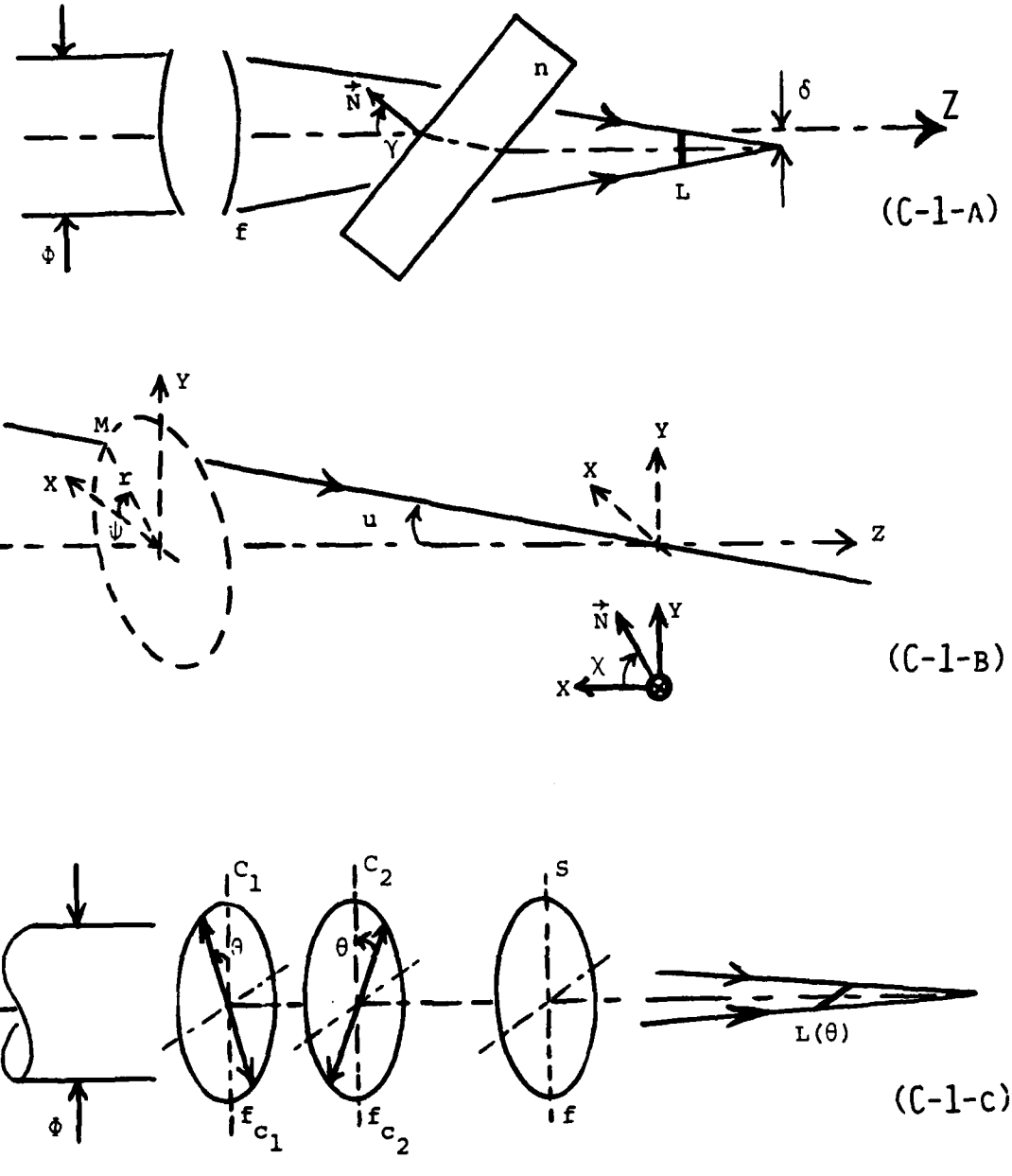

FIGURE C-1 : OPTICS TO PRODUCE A LINE-FOCUS.

A- TILTED BLAST-SHIELD,

B- (GEOMETRY FOR THE CODE LINFOC),

C- CYLINDRICAL CORRECTOR PLATES.

the intensity distribution in the focal region, the code neglects other aberrations in the lens or in the incident beam. In particular, the slope of the ray emerging from the cylindrical optics (see Figure C-1-b) is given by

$$\tan u(r,\psi) = r\{(\cos\psi / f_x)^2 + (\sin\psi / f_y)^2\} \qquad \text{(C-1)}$$

where r and ψ are the polar coordinates of the incident ray, f_x and f_y are the focal lengths in azimuths $\psi=0^\circ$ and $\psi=90^\circ$ respectively. The cosinus directors of that ray are represented by the unit vector $\vec{s}$:

$$\vec{s} \begin{cases} s_x = -(r/f_x)\ \cos\psi\ \cos u \\ s_y = -(r/f_y)\ \sin\psi\ \cos u \\ s_z = \cos u \end{cases}$$

The tilt of the glass plate, assumed plane and parallel, is defined by the angle γ between its normal $\vec{N}$ and the optical axis Z, while its rotation is defined by the angle χ between the planes (N,Z) and (X,Z). $\vec{N}$ is represented by a unit vector:

$$\vec{N} \begin{cases} N_x = \sin\gamma\ \cos\chi \\ N_y = \sin\gamma\ \sin\chi \\ N_z = -\cos\gamma \end{cases}$$

The propagation through the plate is done using Snell's law, $\sin i = n \sin i'$, where n is the index of refraction of the glass and $\cos i = |\vec{s}.\vec{N}|$.
The code gives the lateral displacement of the optical axis and provides

in graphic form the intensity distribution in any image plane along the Z-axis.

C-2. Optics to produce a line-focus.

For an ASE device in the soft X-ray region, one needs to produce a line-shaped plasma of aspect ratio $\rho \gtrsim 10:1$. A smaller ratio would make it difficult to observe any angular dependence because plasma expansion tends to blur the geometry of the original focus. It is not easy, at least in our experimental set-up, to create a plasma of transverse dimension smaller than 80 μm. The minimum length of the line focus should therefore be $\sim$ 1 mm. The maximum length depends on the available laser energy and the atomic number of the target material. A population inversion in the Helium-like stage of Aluminum requires about 2×10^{14} W/cm^2 of UV light or 4×10^{14} W/cm^2 of IR light on target. A 1 mm x 100 μm focal spot would require 100 J of UV light or 200 J of IR light in 500 psec. It is close to the limit capability of the GDL laser when upgraded with active mirrors (see Chapter 3). Targets of lower atomic number such as Fluorine require intensities in the 10^{13} W/cm^2 range, making it possible to extend the length of the line to several mm.

There are a number of designs to form such a line-focus. Limiting ourselves to a maximum of three optical elements, to reduce reflection losses and ghost problems, we can consider:

a) one single lens with two different foci,

b) two strong cylinders, in translation or rotation,

c) the main aspheric lens (the lens used in point focus experiments) followed by a thick blast-shield with a large tilt angle,

d) two weak rotating cylinders, before the aspheric lens.

The first two options are difficult to manufacture in large size. Also in option a the length of the line cannot be tuned. We did, however, use an existing lens of that type in preliminary experiments with IR light (see Chapter 4).

Option c takes advantage of the strong astigmatism introduced by the blast shield. Figure C-2, produced by the code LINFOC, illustrates how one can form a line-focus of aspect ratio $\simeq$ 10:1 using that method. The length of the line can be tuned, though in a limited range, either by changing the tilt angle γ (which does not require another plate) or the thickness t. There is a large lateral shift (δ = several centimeters) of the laser axis. One may expect the non-uniformity of the geometrical image to be smoothed by diffraction in the beam or the optics, though it is not a requirement: the focus is dissymmetric enough for our purpose and its central gap may actually help the cooling of the plasma (Silfvast, et al, 1979-a).

Option d is the most attractive. It is easier to manufacture than options a and b and more tunable, less aberrated, and less massive than option c, with no beam walk-off. It is described in the next section.

C-3 Design and manufacture of a cylindrical lens.

Figure C-1-c shows the combination of lenses chosen to produce a variable line focus. S is the aspheric lens used in point-focus experiments (focal length f), C_1 and C_2 are two identical cylindrical lenses with very weak power ($1/|f_{C_1}| = 1/|f_{C_2}| = 1/f_C \ll 1/f$). Neglecting the spacings between the lenses, the length of the line focus is

LASER INTENSITY DISTRIBUTION ON A FLAT TARGET

(GDL → ASPHERIC LENS → TILTED BLAST SHIELD → TARGET)

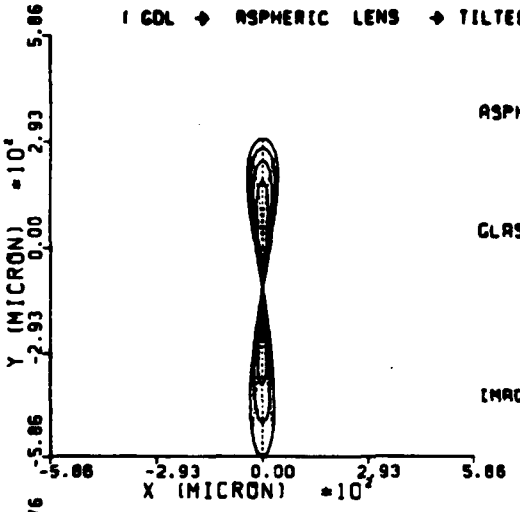

ASPHERIC LENS :
BEAM DIAMETER = 200.00 MM
FOCAL LENGTH = 600.00 MM

GLASS PLATE (BLAST SHIELD) :
THICKNESS = 10.00 MM
REFRACTIVE INDEX = 1.500
TILT / Z-AXIS = 45.00 DEG.MIN

IMAGE PLANE Z = -1.25 MM

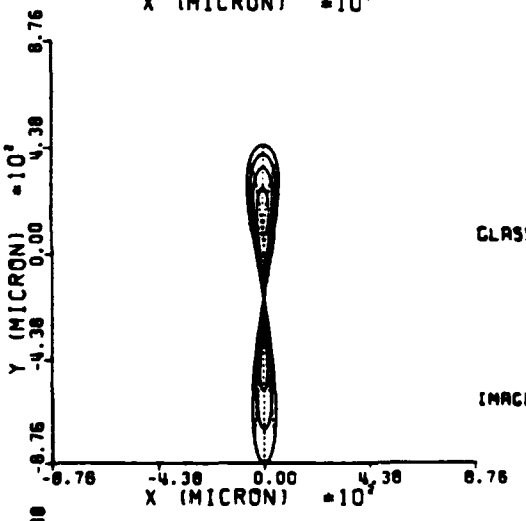

GLASS PLATE (BLAST SHIELD) :
THICKNESS = 15.00 MM
REFRACTIVE INDEX = 1.500
TILT / Z-AXIS = 45.00 DEG.MIN

IMAGE PLANE Z = -1.86 MM

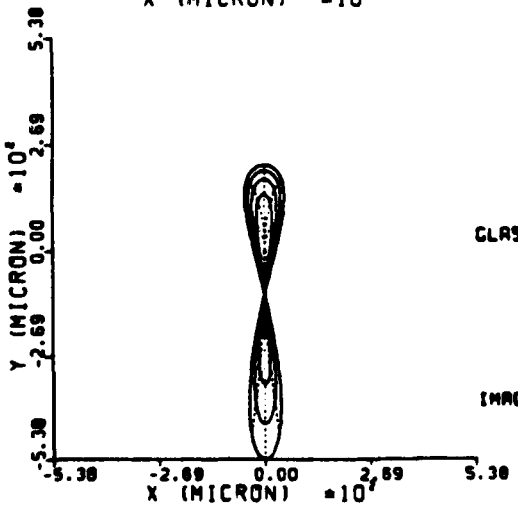

GLASS PLATE (BLAST SHIELD) :
THICKNESS = 15.00 MM
REFRACTIVE INDEX = 1.500
TILT / Z-AXIS = 35.00 DEG.MIN

IMAGE PLANE Z = -0.95 MM

FIGURE C-2.

$$L(\theta) = 2\Phi\ (f/f_c)\ \cos 2\theta \qquad \text{(C-2)}$$

where D is the diameter of the incident beam and θ the half-angle between the axis of the two cylinders. The relationship between f_c and the cylindrical sag at the center of one of the lenses is as follows:

$$-1/f_{c_1} = 1/f_c = (n-1)/R \qquad \text{(C-3)}$$

$$\text{sag}_c = R(1-\cos\alpha) \simeq R\,\alpha^2/2 = \Phi^2/8(n-1)f_c \qquad \text{(C-4)}$$

where R is the radius of curvature of the cylinder. Therefore

$$\text{sag}_c = L_{max}/16(n-1)\ f\# \qquad \text{(C-5)}$$

Since the absolute value of the overall focal length ($F \simeq f$) of the three-lens optics is unimportant, the cylindrical lenses need not be perfect. If C_1 and C_2 have some spherical power ($1/f_{s_1}$, $1/f_{s_2} << 1/f$), the focal length is changed by $\Delta F \simeq (1/f_{s_1} + 1/f_{s_2})f^2$. The power $1/f_{s_i}$ results in a spherical sag in the ith lens:

$$(\Delta\,\text{sag})_{s_i} = \Phi^2/8(n-1)\ f_{s_i} = (\Delta F)_i\,\Phi^2/8(n-1)f^2 = (\Delta F)_i/8(n-1)\ f\#^2 \qquad \text{(C-6)}$$

If one tolerates an overall uncertainty $\pm(\Delta F)_{max}$ on F, the tolerance on the spherical sag for each "cylindrical lens" is

$$(\Delta\,\text{sag})_s = (\Delta F)_{max}/[(n-1)(4\ f\#)^2] \qquad \text{(C-7)}$$

To have the flexibility of working with low-Z targets, we set the tunability requirement to be L = 0 to 4 mm (L = 2 mm when only one cylinder is used). With n=1.5 and $(\Delta F)_{max} \simeq 1$ cm, the specifications on

each lens are as follows:

f#	sag_c	$(\Delta sag)_s$
3	166 μm	139 μm
6	83 μm	35 μm
12	42 μm	9 μm

The UV beam and focusing optics available to us were such that D ≃ 13 cm and f-number ≃ 12, hence the idea arose of achieving the small cylindrical sag required by bending and polishing a flat plate of fused silica. The process is described on Figure C-3. The dimensions of the plate, not including the edges, were 5.7"x5.7"x0.3". The bending knife, which ran the length of the plate, was raised by the motion of two sliding wedges. Each step was controlled with a Fizeau interferometer. The main difficulties of that process are

(i) to polish flat a large square-shaped surface (step 1: lower surface, step 3: upper surface). It is difficult to maintain the same rate of wear at the corners of the plate and at the center. Fortunately the knife runs along a transverse, not a diagonal direction and in the end the lens is used in a circularly symmetric beam. The quality of the corners affects neither the symmetry of the bending nor the quality of the line-focus. Along the direction of the knife the flatness of the plate must be within about a wave, the mechanical quality of the knife becoming the limiting factor. The overall polish must be smooth enough for the deposition of anti-reflection coatings capable of handling a high-power beam. In our experiments the power load at 0.351 μm can be as high as 1 GW/cm^2, or 0.5 J/cm^2 in 500 psec.

MANUFACTURE OF A CYLINDRICAL CORRECTOR FOR LINE-FOCUS EXPERIMENTS

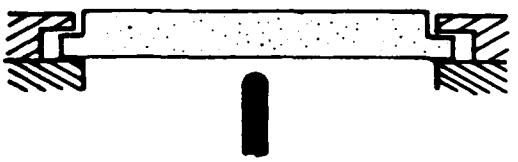

1. The lower surface has been polished flat. The plate is inserted in the mount.

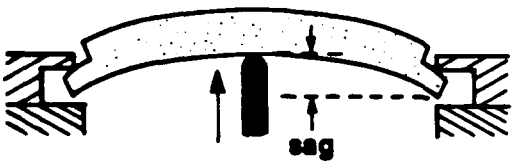

2. The edges are clamped. The central knife is raised to produce the appropriate sag.

3. After proper blocking, the upper surface is polished flat.

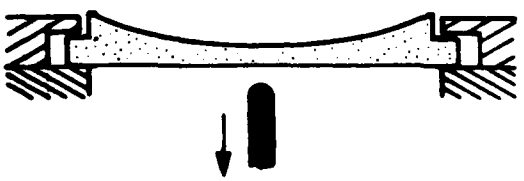

4. The plate is unblocked. The knife is lowered, producing a concave (negative) cylindrical lens.

FIGURE C-3.

(ii) to measure the sag introduced in step 2, which determines the length of the line-focus. The bending produces a saddle-shaped interferometric fringe pattern because initially the plate is slightly concave at the center (if that residue was convex, the bending would be less even and the pattern more distorted). The fringes are very dense at the edges (see Eq.C-4). Only at the center of the plate can their spacing be resolved accurately and used to measure the sag from an extrapolation based on the assumption of a circular bend. Good agreement was found between the cylindrical sag set interferometrically in the optical shop and the length of the line-focus measured with the alignment beam of the GDL laser.

ACKNOWLEDGEMENTS

Before mentioning some of the people who helped me during the course of this work, I would like to express my appreciation and gratitude to the University of Rochester, and specifically the Institute of Optics and the Laboratory for Laser Energetics, for inviting me here and for giving me a chance to get good scientific experience.

I am very grateful to Dr. James M. Forsyth for welcoming me in his group, and for providing valuable advice and continued support during this research.

I am indebted to Dr. Barukh Yaakobi for sharing his expertise in plasma physics and spectroscopy, and to Dr. Jacques Delettrez, who ran many numerical simulations with the code LILAC and discussed the results with me.

Most of the experiments reported in the thesis were done with the Glass Development Laser. I would like to thank Drs. John Soures, Wolf Seka and their colleagues for the opportunity to use that impressive system.

For the manufacture of an important cylindrical lens, I relied heavily on Herb Graf, who succeded in a difficult task.

I have received help from many other members of the Laboratory. A limited list of those that I would like to thank includes J. Abate, F. DeWitt, R. Frankel, J. Grosso, J. Kelly, and A. Rosenbluth. I would also like to mention Dr. Conger W. Gabel: while not specifically associated with this work, he was extremely helpful at an earlier stage, guiding my studies and introducing me to the local optics community.

Special thanks to my wife, Cynthia, for her patience and moral support.

This research was partially supported by the following sponsors: Air Force Office of Scientific Research (grant AFOSR-81-0059), Exxon Research & Engineering Company, General Electric Company, Northeast Utilities, New York State Energy Research & Development Authority, Standard Oil Company of Ohio, University of Rochester, and Empire State Electric Energy Research Corporation. Such support does not imply endorsement of the content by any of the above parties.

FILM
2-8
DTI